Long-term Global Morphology of Gravity Wave Activity Using UARS Data

Contract NAS5-98045

FINAL REPORT

Sep 18, 2000 – Dec 18, 2000

Principal Investigator
Stephen D. Eckermann

ABSTRACT

This report provides a broad outline of the total body of research conducted during the past three years. We report on detailed model studies of the precise way in which infrared limb scanning satellites explicitly detect gravity waves, and use these insights to resolve earlier discrepant zonal mean estimates of gravity wave variances from satellite limb scanners. Detailed analysis of CRISTA temperature fluctuations are outlined, which provide new global information on long-wavelength stratospheric gravity waves generated by mountains, tropical convection and the mid-latitude jet stream-vortex system, as well as interactions higher in the mesosphere with the diurnal tide. The detailed insights gained from analyzing CRISTA data are applied to provide a multi-year analysis of stratospheric mountain waves over the Andes evident in MLS limb-track data. We also demonstrate for the first time that stratospheric temperature data from the CLAES instrument on UARS resolved gravity waves, and we highlight mountain wave information in a subset of these data. Final conclusions and recommendations are set forth, and the present findings are directly related to the original goals of the research contract. A full list of publications that resulted from this research is provided.

A three-year research project funded by:

Office of Mission to Planet Earth
National Aeronautics and Space Administration
Washington, DC 20546.

NRA-97-MTPE-04 (Science Investigations in Support of the UARS Mission)

TABLE OF CONTENTS

1. Introduction

Following the guidelines outlined in the proposal contract, we present a final report on the project without explicitly reporting on results performed during the last three months of the project just completed. We have performed a wide variety of tasks under this contract, and it is impossible to outline all the results in this report: much of it has been documented in the previous collection of eleven quarterly reports submitted during the three-year project lifetime.

Newer work that has yet to be written up will receive the major writeups in this report. Work that has been successfully transitioned to be publication stage will be reviewed more briefly.

This research has benefited greatly from collaborations forged during the three years of this project. I particularly wish to acknowledge the pivotal role played by Dr. Peter Preusse, of the Department of Physics and Mathematical Physics, University of Wuppertal, Germany, whose dedicated efforts made much of the work outlined here possible.

2. Major Work and Results (Including New Results This Quarter)

2.1 Are Gravity Waves Resolved by Infrared Limb-Scanning Satellites?

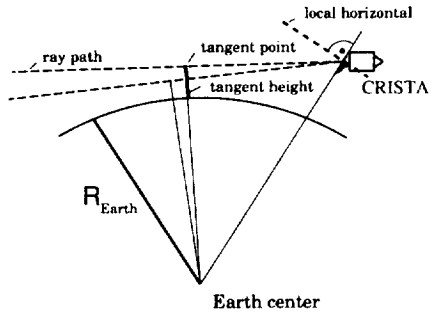

Figure 1: Measuring geometry of the limb sounder. Two rays with different tangent heights are shown. CRISTA orbits clockwise in this Figure, whereas for CLAES or MLS the orbit is either perpendicularly into or out of the page (depending on the yaw cycle).

Our work in modeling the way in which CRISTA and other limb scanning instruments detect gravity waves has been set out at length in previous reports [*Preusse et al.*, 1999; section 1.4 of report dated March 18-June 18, 1998; section 1.4 of June 18-September 18, 1998; section 1.2 of report dated 18 June-September 18, 2000]. Since the bulk of the work has been reported previously, only a brief overview of the major results and some previously unreported results will be provided here. The major findings are that CRISTA explicitly resolves long wavelength gravity waves from retrieved temperatures derived from inversion of 12.6 μm CO_2 limb-scanned radiances. These results also apply to similar temperature data acquired by the CLAES instrument on UARS. The gravity waves extracted from both instruments' data are discussed in sections 2.3 and 2.5.

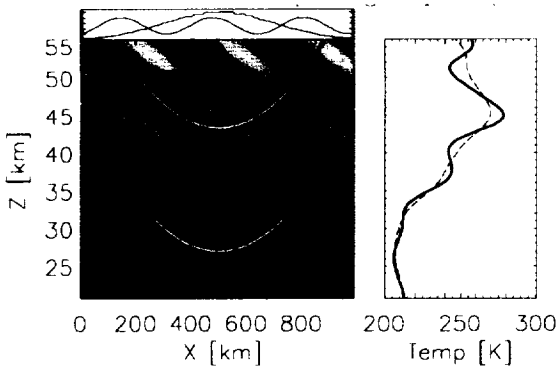

Figure 2: Viewing geometry of a limb sounding projected through a simulated two-dimensional gravity wave temperature perturbation superimposed upon a background temperature profile. Two limb ray paths with different tangent heights are shown in left panel. Top panel gives the weighting function along a ray path as well as wave oscillation phase

The observational situation is shown schematically in Figure 1. In our model, we insert a linear two-dimensional sinusoidal temperature fluctuation due to a gravity wave, projecting those oscillations into a 2D plane both in altitude, z, and in horizontal distance along the limb-scan direction, x. This oscillation exists on top of a mean background temperature profile. Then we simulate a limb scan of the atmosphere by CRISTA under the influence of this perturbed temperature profile, yielding 12.6 μm CO_2 radiance profiles, of the form

$$I(z) = \int_{-\infty}^{\infty} \xi(s) B[T(s)] ds$$

The geometry of this situation is set out in Figure 2, showing limb ray paths through a two-dimensional gravity wave. Here s is the distance increment along one of the limb ray paths shown in Figure 2, $\xi(s)$ is the emissivity at distance s along the limb ray path, and $B(T)$ is the blackbody radiance function.

From here, we passed these model limb scanned radiance data *I(z)* through the same retrieval algorithms used for actual CRISTA retrievals, to back out a temperature profile *T(z)*. Then we analyzed the fluctuations that remain on the extracted profile and compared the measured amplitude of the fluctuation, $\hat{T}$, to the actual amplitude of the wave we inserted, $\tilde{T}$. This yields a "visibility," $\varepsilon=\hat{T}/\tilde{T}$, of CRISTA to the gravity wave of this particular amplitude with the given vertical and horizontal wavelength pairing (λ_h,λ_z). We then conducted a series of these simulations using different gravity wave wavelengths λ_h and λ_z to infer a net two-dimensional CRISTA visibility function, $\varepsilon(\lambda_h,\lambda_z)$ to gravity waves with varying wavelength properties aligned along the limb-scan direction.

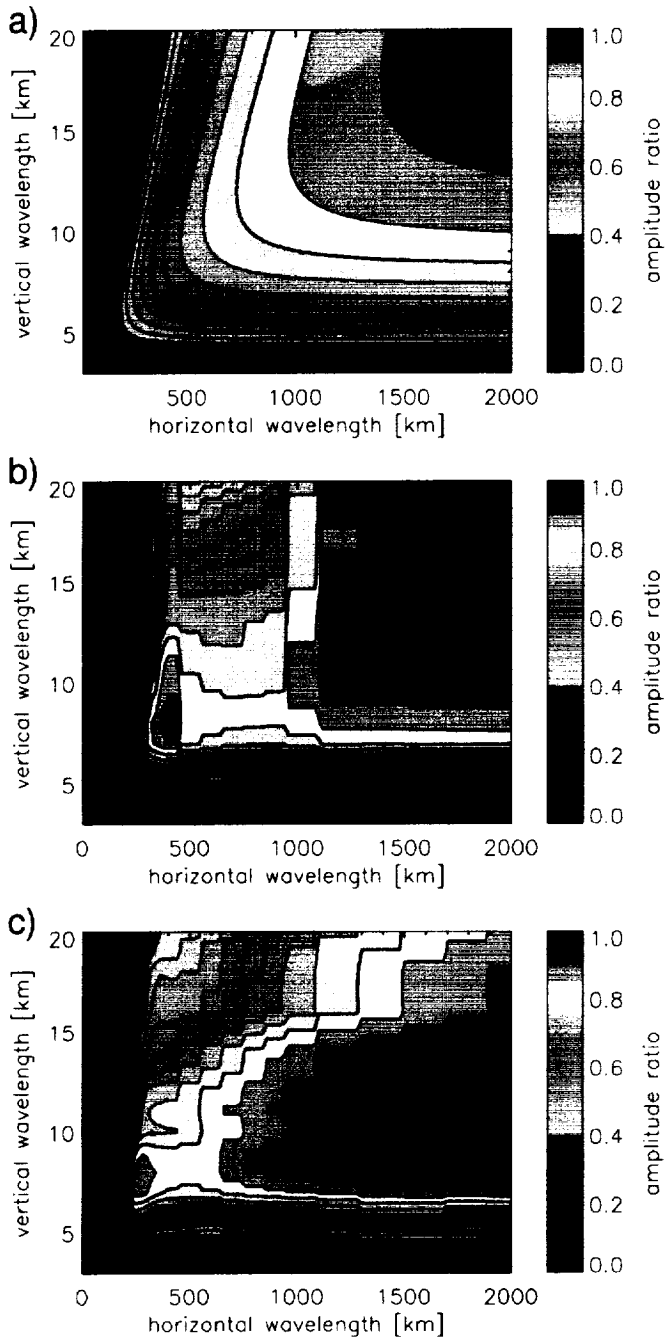

Figure 3: Estimated visibilities $\varepsilon(\lambda_h,\lambda_z)$ of CRISTA temperatures to gravity waves with different horizontal and vertical wavelengths. Radiative transport and well as retrieval effects are included in the calculations. Panel (b) shows full calculations using a constant amplitude of 1K, (c) using amplitudes that grow exponentially with height. Panel (a) shows an analytical model for the visibility function that is developed under certain simplifications by *Preusse et al.* [2000*c*].

These calculations are extremely expensive to do numerically, and a considerable amount of computing time and effort was required to generate results that are summarized in Figures 3b and 3c. The major advance in these new calculations over previous more limited efforts is the use of full BANDPAK libraries [*Marshall et al.*, 1994] to generate realistic radiance fields measured along the limb, and use of updated CRISTA retrieval algorithms in the inversion back to a limb-scanned temperature profile. Figure 3b shows results in which the amplitudes of the temperature perturbations in Figure 2 were kept constant at 1 K. Figure 3c shows similar collated results in which the temperature amplitudes were allowed to grow quasi-exponentially with altitude. Figure 3a shows an analytical simplification in which we simplified the problem by assuming that:

- The blackbody radiance function *B(T)* can be approximated by the first term in its Taylor series expansion
- The considered range of wavelengths is optically thin.
- The atmosphere is isothermal
- The wave amplitude remains constant with altitude

Further details of the calculations and the analytical simplification are provided by *Preusse et al.* [2000c].

In summary, we see that the three sets of plots in Figure 3 are broadly similar. All show >50% visibility of CRISTA to gravity waves with vertical wavelengths $\lambda_z > 5$ km and λ_h > 200 km. Below these limits, CRISTA's visibility characteristics diminish rapidly, indicating strong smearing of the wave response due to integration of radiance fluctuations

along the limb. We view these two-dimensional simulations as "worst case" scenarios, since here CRISTA scans the limb at a 90° angle to the wave phase fronts, as shown in Figure 4 (top). If CRISTA scanned at some other angle, as shown schematically in Figure 4 (bottom), then the smearing of the temperature wave along the limb in much reduced, since the wave presents a longer horizontal wavelength component along the limb direction. Thus, we believe that the zones of >50% visibility to gravity waves in Figure 3 mark those long wavelength gravity waves that CRISTA should be able to observe nearly all the time, regardless of the horizontal orientation of the phase fronts with respect to the CRISTA viewing direction. Waves with lower visibility will tend not to be observed in these "worst case" scenarios, but may be episodically visible if/when CRISTA scans the wave in some configuration closer to the "best case" scenario in Figure 4. Indeed, this can be gauged directly from Figure 3. As depicted schematically in Figure 5, for an angle α between the CRISTA scan direction and the gravity wave horizontal wavevector direction, the component of the horizontal wavenumber intercepted by the CRISTA ray path scanned through the line of sight (LOS) along the limb (pink curve in Figure 4) is $k_{limb} = k_h \cos\alpha$, where $k_h = 2\pi/\lambda_h$ is the gravity wave's horizontal wavenumber and α is 0° or 180° for the "worst case" and 90° or 270° for the "best case." Thus the wavelength along the limb LOS resolved by CRISTA is $\lambda_{limb} = \lambda_h \sec\alpha$, so that for the "best case" scenario in Figure 4, λ_{limb} is essentially infinite and the visibility of CRISTA to the gravity wave in this case is given by values for a given λ_z at the long horizontal wavelength limit of Figure 3.

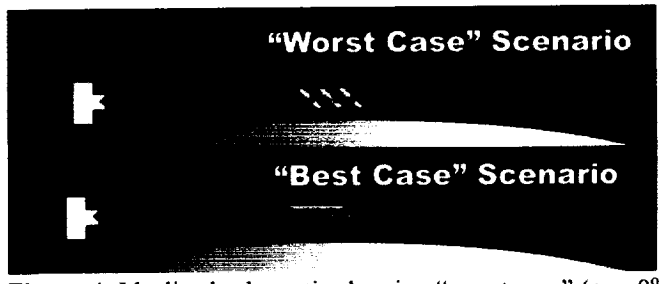

Figure 4: Idealized schematic showing "worst case" (α = 0° or 180°) and "best case" scenarios (α = 90° or 270°) for CRISTA limb scan though a gravity wave segment, shown as red-yellow temperature banding in a quasi—horizontal plane near the tangent height. Figure 2 represents the physics of the "worst case" scenario above.

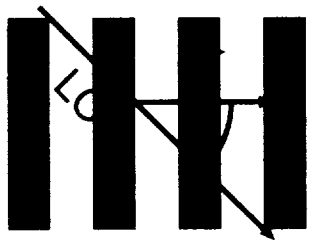

Figure 5: Relation between CRISTA line of sight (LOS), shown in pink in Figure 4, wave phase fronts, and the gravity wave horizontal wavenumber vector $\vec{k}$ and the

In addition to the fidelity of the amplitude retrieval, we have also studied how the wave's vertical wavelength and phase are affected by the retrieval. Figure 6 shows a scatterplot of the actual versus the retrieved vertical wavelengths. The effects here combined both the weaknesses in the retrieval as well as the MEM/HA analysis to isolate gravity waves in temperature profiles (this method that has been discussed at length in previous reports and will be discussed briefly in section 2.3.1). We see from Figure 6 generally good retrieval of the vertical wavelength of the gravity wave in each case. We also investigate the absolute phase of the retrieved disturbance at a given altitude. The combined results are shown in Figure 7. We see that phase shifts are generally small, except at the boundary regions of the amplitude sensitivity evident in Figure 3b. Thus, as expected, the wave phase retrieval is less reliable in those regions of Figures 3b and 7 where the wave is at the limit of the instrument's intrinsic ability to "see" the gravity wave. We have also studied the altitude dependence of these gravity wave retrievals. Figure 8 shows a plot of the one-

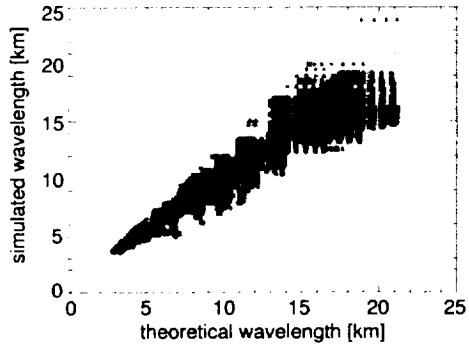

Figure 6: Scatterplot of retrieved versus input vertical wavelength. Solid line indicates 100% accurate retrieved value.

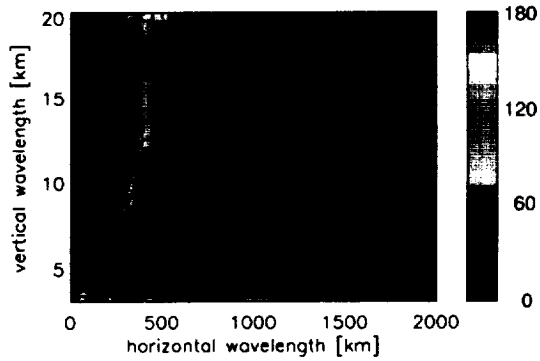

Figure 7: As for Figure 3b, but showing phase shifts in retrieved compared to actual wave.

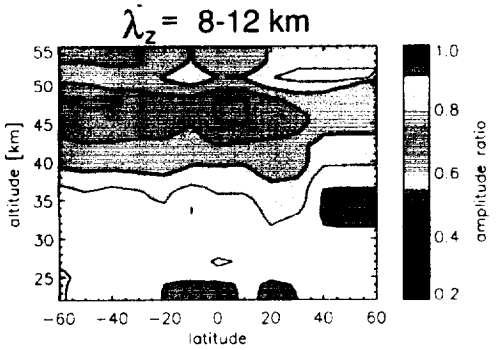

Figure 8: Latitude-height distribution of one-dimensional mean visibility function $\hat{\varepsilon}(\lambda_z)$ in the 8-12 km vertical wavelength range.

dimensional visibility approximation (see section 2.2) inferred over the 8-12 km range of vertical wavelengths. We see there is little latitudinal dependence to the visibility, but some slight height dependence, with marginally better sensitivity at lower altitudes compared to higher stratospheric altitudes.

These results were formulated specifically for observations with the CRISTA instrument, since we have full details of the data, the radiance measurements, the retrieval algorithms and the data analysis algorithms. Nonetheless, we believe that these results also translate to temperature measurements acquired by the CLAES instrument on UARS, which acquires its stratospheric temperature data via inversion of limb scanned radiances from the 12.6 μm CO_2 Q-branch emissions [see, e.g., *Gille et al.*, 1996]. Thus, the results in Figures 3-8 immediately suggested to us that we should be able to resolve gravity waves in CLAES temperatures, in much the same way that we have verified both theoretically and experimentally for CRISTA. This work motivates the study in section 2.5.

Although we have provided some depth to the analysis here, we cannot provide full details. Initial results can be found in the publications of *Preusse et al.* [1999] and *Preusse et al.* [2000a] (the latter reproduced in section 7.2), and a full writeup of the modeling work outlined herein is provided in the work of *Preusse et al.* [2000*c*]. Another separate spectral study of a special high-resolution subset of CRISTA data has also largely supported the theoretical sensitivity results presented here. That work of ours has just been submitted for publication [*Eidmann et al.*, 2000] but is not described here due to space constraints.

2.2 Reconciling Zonal Mean Global Estimates of Gravity Wave Temperature Variances in the Middle Atmosphere Measured by Various Satellite Instruments

At the beginning of this project, some preliminary maps of small-scale temperature variance had been compiled from satellites. Examples include analysis of small-scale temperature fluctuations in data from the Limb Infrared Monitor of the Stratosphere (LIMS) on the NIMBUS 7 satellite [*Fetzer and Gille*, 1994], and radiance fluctuations from microwave limb radiance data from the Microwave Limb Sounder (MLS) instrument on the UARS satellite [*Wu and Waters*, 1997]. Zonal mean maps of variances from these two instruments are shown in Figure 9. It was noted that the activity differed greatly between these and other instruments. These discrepancies, along with the fact that gravity wave fluctuations existed at the spatial and precision limits of all these instruments, meant that there was little agreement as to the

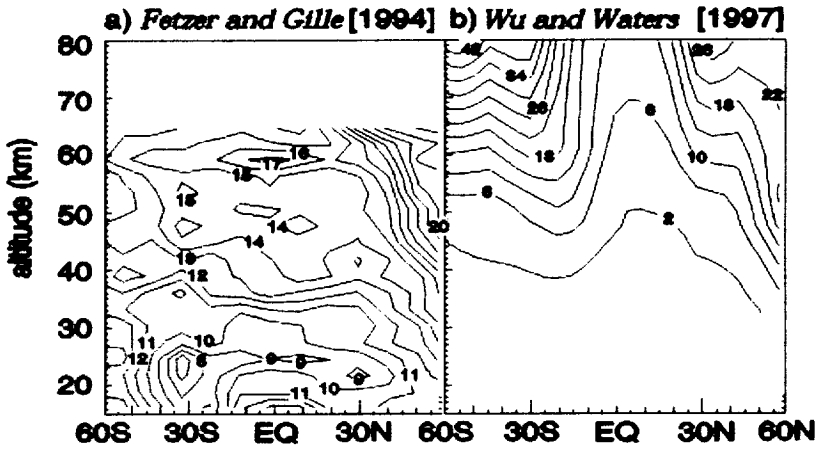

Figure 9: Zonal mean distributions of small-scale temperature-related variance due to gravity waves, plotted as a function of latitude and height, from satellite data acquired by (a) LIMS [after *Fetzer and Gille*, 1994] and (b) MLS [after *Wu and Waters*, 1997]. LIMS contours are temperature variances in dB over 1 K^2 (i.e., 10 dB = 10 K^2, 20 dB = 100 K^2). MLS contours are relative radiance variances. Both datasets were acquired during northern winter (6-12 November, 1978 for LIMS data, December 20, 1992-January 29, 1993 for the MLS data).

geophysical significance of these preliminary satellite-derived gravity wave data. Indeed, at the beginning of this project, it was unclear whether any of these instruments were reliably measuring gravity waves. A major focus of this project was to investigate these issues both theoretically and observationally.

The modeling study outlined in section 2.1 revealed that limb-scanning satellites should, theoretically, be able to resolve long wavelength gravity waves in the stratosphere and mesosphere. Why, then, are zonal mean results like those in Figure 9 so variable among the various instruments?

Alexander [1998] used model ray tracing data to propose that much of the difference in Figure 9 could be explained by the spatial sensitivity functions of the various instruments. Put simply, the two-dimensional visibility functions (see Figure 3) can vary considerably between instruments, meaning that each instrument is observing different wavelength regions of the total gravity wave field in the middle atmosphere. She used these ideas to filter model data to resemble the wavelength scales resolved by MLS and various ground-based instruments such as rockets and radiosondes.

We conducted a study to test these ideas experimentally using CRISTA data as a reference, given the well-defined gravity wave visibility and radiance characteristics we have inferred for this instrument [*Riese et al.*, 1999; see also section 2.1]. First, we approximated the two-dimensional CRISTA visibilities $\varepsilon(\lambda_h,\lambda_z)$ in Figure 3 by a one-dimensional visibility term, $\hat{\varepsilon}(\lambda_z)$, derived by averaging $\varepsilon(\lambda_h,\lambda_z)$ over the horizontal wavelength range from 300-800 km. This is largely valid since, from Figure 3, the visibility does not vary significantly over this range, but falls off rapidly below it. We can now use this one-dimensional visibility factor, $\hat{\varepsilon}(\lambda_z)$, to correct for imperfect observations by CRISTA of the measured gravity wave amplitudes $\hat{T}$ without having to know what the wave's horizontal wavelength was (horizontal wavelengths are difficult to measure from satellite instruments given the comparatively coarser horizontal resolution of satellite data).

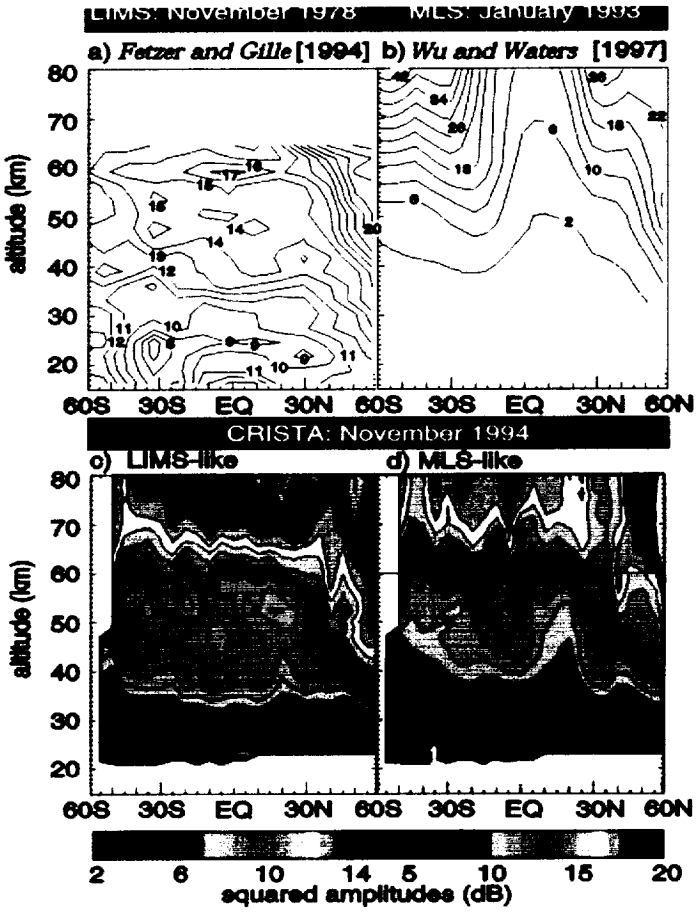

Figure 10: Top row as in Figure 9. Bottom row shows "LIMS-like" and "MLS-like" zonal-mean $\hat{T}$ data from CRISTA. See text for further details. Line in (d) separates high-altitude and low-altitude estimates, which use different one-dimensional visibility functions.

Next we applied new one-dimensional visibility functions to these corrected CRISTA data that crudely represented those of the MLS, LIMS and GPS/MET instruments, represented here by the functions $\hat{\varepsilon}_{MLS}(\lambda_z)$, $\hat{\varepsilon}_{LIMS}(\lambda_z)$, and $\hat{\varepsilon}_{GPS}(\lambda_z)$, respectively. In each case, following *Alexander* [1998], we adopted simple boxcar visibility functions with passbands in the range λ_z > 10-25 km for MLS below 60 km, λ_z > 15-35 km for MLS above 60 km (where the weighting function is much broader), λ_z > 3-15 km for LIMS, and λ_z > 3-10 km for GPS/MET. These functions were applied to the corrected MEM/HA $\hat{T}$ data from CRISTA, to derive new CRISTA datasets that were "MLS-like," "LIMS-like," and "GPS/MET-like." For more background and details on these choices, see *Preusse et al.* [2000a].

Latitude-height global zonal-mean results for the resulting "MLS-like" and "LIMS-like" CRISTA data are shown in Figures 10c and 10d, beneath the original data reproduced from Figure 9 to facilitate easier visual comparisons. We see that the two filtered CRISTA datasets are quite different from each other, due to the effects of the boxcar $\hat{\varepsilon}_{MLS}(\lambda_z)$ and $\hat{\varepsilon}_{LIMS}(\lambda_z)$ visibility functions applied to the corrected data. Furthermore, we see features that resemble the actual LIMS and MLS data redisplayed above in Figures 10a and 10b.

For example, for the LIMS comparisons, we see at low levels that Figure 10c reproduces the equatorial maximum and the minima at 30°S and 30°N evident in the actual data in Figure 10a. Note that these features are not nearly as evident in the MLS-like CRISTA data shown in Figure 10d. We also see a "ledge" of reduced variance growth, or even reductions, with height over the 40-60 km altitude range. Indeed, similar things are also seen in gravity wave temperature data derived from rocketsondes, which have similar vertical wavelength sensitivity [*Eckermann et al.*, 1995].

For the MLS comparisons (right column Figure 10), we see in the "MLS-like" CRISTA data in Figure 10d the general reproduction of a band of attenuated variance centered at ~20°N, which is seen clearly in the actual MLS data reproduced in Figure 10b. The "MLS-like" CRISTA variance grows monotonically with altitude, showing little if any sign of the ledge at 40-60 km in the LIMS data and the "LIMS-like" CRISTA data. Again, the same monotonic increase with altitude is evident in the MLS data in Figure 10b.

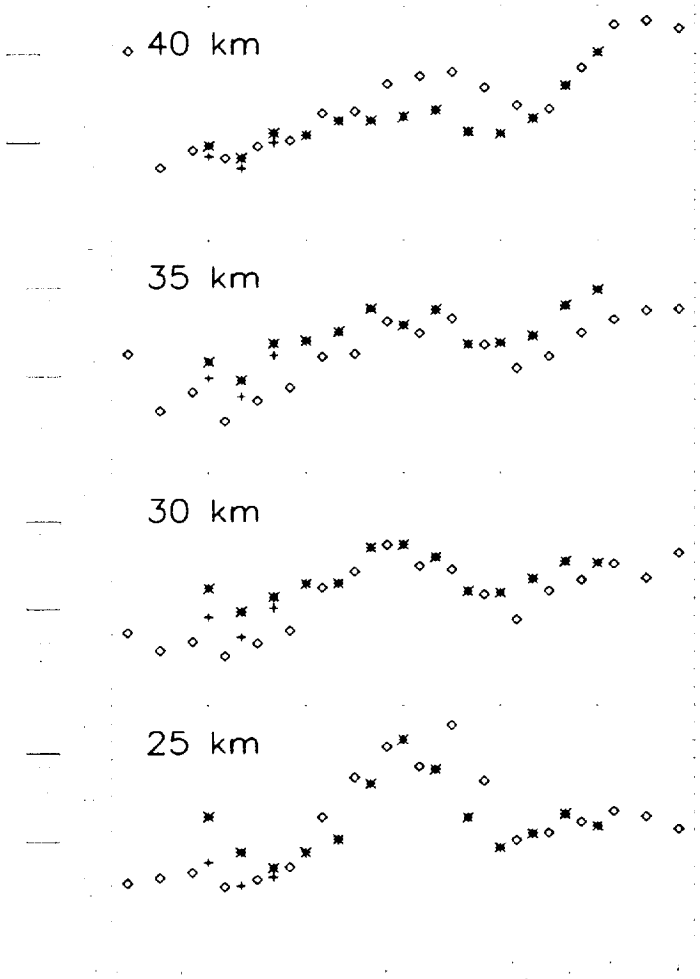

Figure 11: Zonal mean gravity-wave potential energies per unit mass, as a function of latitude and height, derived from GPS/MET data (asterisks) and "GPS/MET-like" CRISTA MEM/HA data (asterisks). Crosses near 40-60S show recalculated "GPS/MET-like" CRISTA MEM/HA data after removal of large values over the Andes.

We also used these ideas to compare with recent gravity wave data inferred from temperature profiles provided by GPS occultation measurements made from the GPS/MET satellite system [*Tsuda et al.*, 2000]. Latitude height variations inferred from the wintertime GPS/MET data are plotted with open diamonds in Figure 11, where here the temperature variances have been converted to potential energies per unit mass using standard gravity wave formulas [see *Tsuda et al.*, 2000]. Corresponding results from the "GPS/MET-like" CRISTA $\hat{T}$ data are plotted with asterisks in Figure 11. We see excellent correspondence between the two, both in shape of latitudinal variations at each altitude, and in absolute magnitudes. At 25 km, the CRISTA data show a larger peak near 40°-60°S due to large mountain waves over the southern Andes in the CRISTA data (see sections 2.3.2 and Figures 14, 15, 17, 20, 21, and 28). When we remove data from the Andean sector of longitudes, we get the new results shown with crosses in Figure 11. Once again, the data here correspond quite well with the mean GPS/MET values of *Tsuda et al.* [2000].

The results in Figures 10-11 and elsewhere provide direct experimental verification of the weighting function argument originally postulated by *Alexander*

[1998] using model data. They show that temperature perturbation amplitudes $\hat{T}$ from different instruments resemble each other once the wavelength filtering characteristics of the measurements are taken into account. It also shows that CRISTA, MLS, LIMS and GPS/MET all made reliable measurements of gravity waves within the particular portions of the gravity wave spectrum they were sensitive to. These results, as well as those in section 2.1, achieve one of the major goals of the project – to assess whether high-resolution satellite instruments on UARS and other satellites make reliable measurements of gravity wave oscillations. Figures 10 and 11 prove beyond doubt that they do.

This work has been described in greater detail in previous reports [e.g., section 1.1 of the report dated December 18, 1998-March 18, 1999; section 1.3 of report dated June 18-September 18, 2000]. A short version of this work was recently published in *Geophysical Research Letters* [*Preusse et al.*, 2000a – see section 7.2] and more complete analyses and details are provided in a paper being drafted for the special issue of *The Journal of Geophysical Research* devoted to first results from the CRISTA 2 mission [*Preusse et al.*, 2000c].

Given the fidelity of the gravity wave signals that sections 2.1 and 2.2 have set forth, the following sections describe detailed analysis of the gravity wave signals in data from different satellite instruments.

2.3 Gravity Wave Activity in CRISTA Temperatures Acquired During the CRISTA-SPAS Satellite Missions

The CRISTA instrument flew on CRISTA-SPAS (Shuttle Pallet Satellite) for two missions of ~1 week duration during shuttle missions STS-66 (4-12 November, 1994) and STS-85 (7-16 August, 1997). CRISTA data taken during each mission will hereafter be referred to as CRISTA 1 and CRISTA 2 data, respectively. Here we analyze CRISTA temperatures acquired in the stratosphere from 12.6 μm CO_2 emissions, and mesospheric data from the 15 μm emission. Analysis in previous sections shows that these data contain gravity wave-scale spatial structures. We infer amplitudes $\hat{T}$ of small-scale temperature fluctuations due to gravity waves in these CRISTA data using the MEM/HA analysis method applied to Kalman-detrended global temperature fields for each day of the mission, as developed and outlined in previous reports. We outline the final procedure in a formal way in section 2.3.1. We use the $\hat{T}$ data from this analysis of the 12.6 μm CRISTA temperature channel to study stratospheric gravity waves emanating from mountains (section 2.3.2), from the jet-vortex region (section 2.3.3) and from tropical convection (section 2.3.4). We conclude by analyzing high altitude temperature data from the 15 μm CRISTA temperature channel to study mesospheric gravity waves in section 2.3.5.

2.3.1 Extraction of Gravity Waves from Global CRISTA Temperature Data

Over the course of this contract, we developed and refined our own, largely new method for extracting gravity wave temperature fluctuations from global satellite data, which we describe only briefly here, since it has been described at length in various other places [*Preusse et al.*, 1999; *Eckermann and Preusse*, 1999; *Preusse et al.*, 2000c]. Nonetheless, since it is a key analysis method used throughout the project, we describe it briefly in this section.

First, given global asynoptically sampled temperature data each day, we remove the planetary-scale structure using a Kalman filter [*Rodgers*, 1977] that fitted temperatures at each level to zonal wavenumbers 0-6, which should account for most of the mean state and planetary waves that exist globally [e.g., *Fetzer and Gille*, 1994]. In addition, we fit data from ascending and descending nodes separately, since these data are separated in local time by ~12 hours and thus these separate fits help to remove the diurnal tide (this is important in the mesosphere – see section 2.3.5). The background temperature estimated by the Kalman fits at various altitudes are interpolated to the precise locations of each temperature measurement in performing the detrending of individual temperature profiles. See *Preusse et al.* [2000c] for further details.

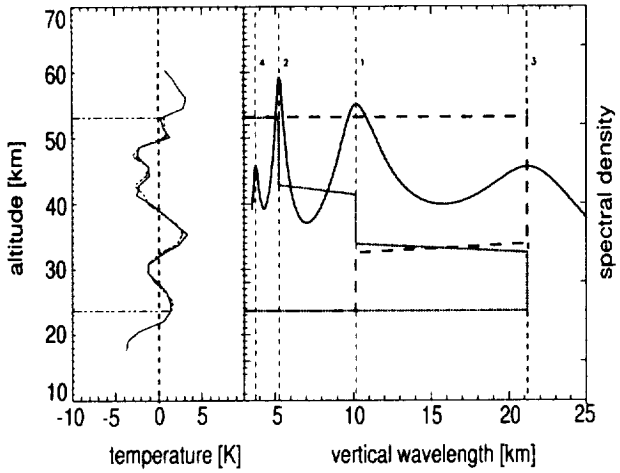

Figure 12: Example of the way in which the MEM/HA analysis method works, in application to CRISTA1 residual temperature data. This profile (solid curve, left panel) was acquired on November 9, 1994 at ~24°S and 82°W over Chile. Right panel shows the MEM spectrum, with the two major peaks highlighted by dotted lines at wavelengths ~5 and 10 km. The spectral density scale is logarithmic. Dotted curve on left shows reconstructed profile based on sliding harmonic analysis of the original profile constrained by these two major peaks in the MEM spectrum. We see this fit captures most of the detail in the original residual temperature profile

After we have removed the background, we are left with a global distribution of profiles of residual temperatures $\tilde{T}(x,y,z)$. We search for gravity wave fluctuations in these profiles using a combination of spectral analysis using the Maximum Entropy Method (MEM), and a (vertically) sliding harmonic analysis fit (HA) constrained by the two peak wavenumbers identified in the MEM spectrum. We refer to this hereafter as the MEM/HA analysis method.

The method is best illustrated using an actual example, which is given in Figure 12. The original residual temperature from CRISTA1 data is plotted with the solid curve in the left panel, and its MEM spectrum is shown in the right panel. Four local maxima in the MEM spectrum are evident, with the major two being at wavelengths of ~5 km and ~10 km. These two harmonics were then used to perform harmonic fits that were slid vertically in 1.5 km vertical increments through the full height range of the profile. A reconstructed profile based on these fits is shown as a dotted curve in the left panel of Figure 12.

The MEM/HA analysis is useful in that it gives a peak vertical temperature amplitude for each harmonic, $\hat{T}$, at each height level in the profile. It is also easy to automate this analysis, allowing us to analyze and store results for the large number of profiles provided by satellite data. Most of the results in following sections plot estimates of these $\hat{T}$ amplitudes at given levels in the satellite data.

We have compared the MEM/HA analysis method carefully against more standard Fourier Transform analysis methods that have been used in vertical profile data from radiosondes and lidars. Here we use a sliding Fourier Transform (FT) method to fit the profile in a manner more similar and comparable to output provided by the MEM/HA analysis. Results are summarized in Figure 13, which shows output from MEM/HA analysis (panel a), FT analysis (panel b), and the ratio of the two (panel c). We see from Figure 13 that the MEM/HA method gives better results, particularly at low levels where it captures the tropical peak and subtropical minima in the lower stratosphere better than does the sliding FT analysis (see also Figures 10a and 10c). Note that the LIMS data in Figure 10a were simple standard deviations of Kalman-filtered residuals $\tilde{T}(x,y,z)$.

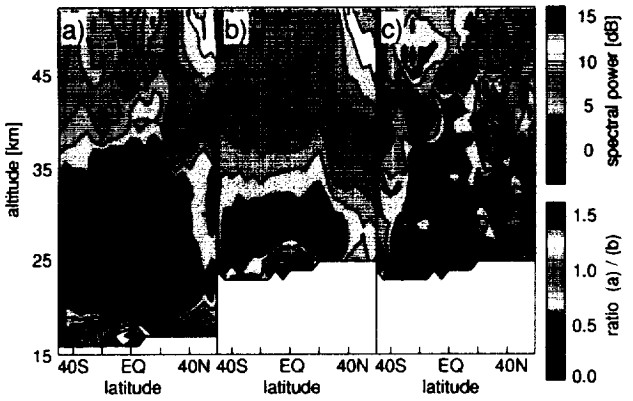

Figure 13: Zonal-mean global $\hat{T}$ amplitudes estimated from CRISTA1 data using (a) MEM/HA and (b) sliding FT analysis. Panel (c) shows the ratio of the two. Since FT requires a finite window in which to form spectral estimates, the height range is less than that for MEM/HA. For more details, see *Preusse et al.* [2000c].

2.3.2 Stratospheric Mountain Waves

2.3.2.1 CRISTA Data Analysis

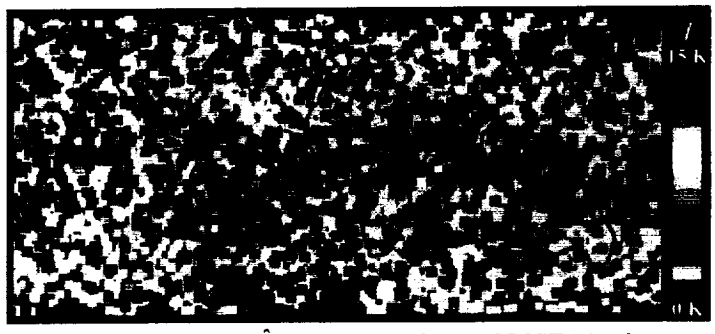

Figure 14: Global $\hat{T}$ amplitudes from CRISTA1 data on November 6, 1994 at 25 km, after correction for visibility effects.

Our analysis of mountain waves in CRISTA data has been a major focus of this project, and has been reported extensively elsewhere, in both reports for this project [section 1.1 of report dated December 18, 1999-March 18, 2000; section 1.1 and 1.2 of report dated June 18-September 18, 1999; section 1.1 of report dated March 18-June 18, 1999] and in publications [*Eckermann and Preusse*, 1999 (see section 7.1); *Britt*, 1999 (see section 7.3); *Eckermann et al.*, 2000a; *Eckermann et al.*, 2000b; *Preusse et al.*, 2000c]. Thus, we will give an overview of the major results: fuller details can be found in the aforementioned references.

Analysis of residual temperature amplitudes $\hat{T}$ from CRISTA data yields global maps like the one shown in Figure 14 for CRISTA1 temperature data at a height of 25 km, acquired on November 6, 1994. What is immediately evident is a clustering of large amplitude values at the southern end of South America. Given that the Andes Mountains are located here, an immediate question is whether these values here are due to mountain waves generated by the Andes that have propagated into the stratosphere.

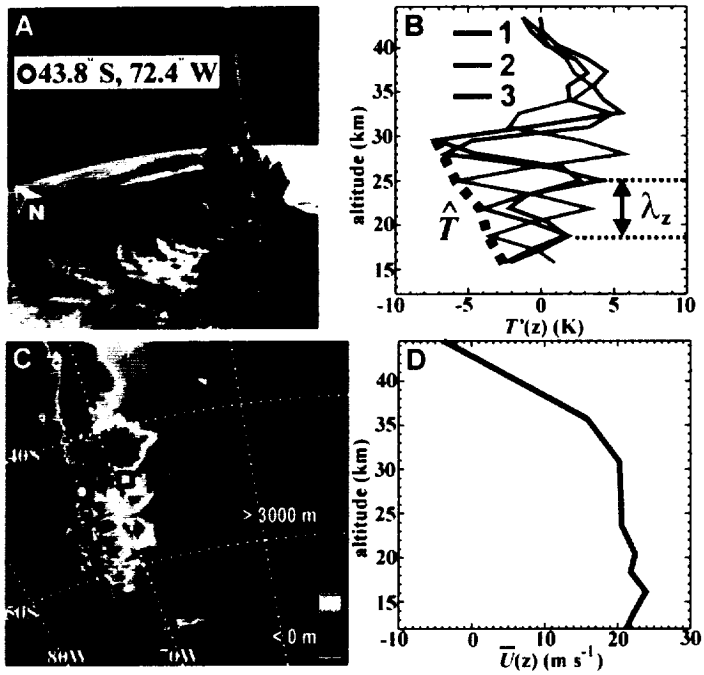

Figure 15: **(A)** Astronaut photograph over southern South America showing deployment of CRISTA-SPAS from Atlantis, 4th November, 1994, 12:19 UT. The cylindrical assembly on the satellite houses CRISTA. The east coast of Argentina and Atlantic Ocean are visible to the right, banded mountain wave clouds downstream of the Andes are visible to the lower-left. **(B)** Temperature perturbations $T'(z)$ from three successive CRISTA scans (labeled 1,2 and 3) on 6th November, 1994 at ~06:00 UT. **(C)** Topographic elevations for southern South America (linear color scale). Squares labeled 1,2 and 3 show locations of the profiles in B. The nadir point and orbital motion of the shuttle in A are shown with a black and white circle and black arrow, respectively. **(D)** Horizontal winds orthogonal to the Andean ridge, from DAO assimilated data [*Coy and Swinbank*, 1997] at 42°S, 69°W on 6th November, 1994, 06:00 UT.

Figure 15 summarizes a detailed analysis of a sequence of three successive profiles acquired by one the three CRISTA observing telescopes as it sampled tangent altitudes at regions labeled 1,2 and 3 in Figure 15c. Large oscillatory temperature amplitudes were evident in these profiles, as shown in the residual data in Figure 15b. That these might be mountain waves is evidenced by the astronaut photograph, shown in Figure 15a, which was taken 2 days earlier as the SPAS was deployed into orbit from the shuttle payload by the shuttle's robot arm. The photograph shows characteristic banded mountain wave clouds downstream of the Andes, which suggests that mountain waves were being produced in the troposphere by flow across the Andes in the days leading up to the stratospheric measurements in Figure 15b.

Inspection of Figure 15b shows that the vertical wavelength of these waves is similar in all three profiles (though phase shifted) at ~6-7 km. A long stationary plane hydrostatic mountain wave emanating from the Andes should have a vertical wavelength given by the hydrostatic relation

Estimate of the Effect of Andean Mountain Wave Breaking on the Background Circulation of the Stratosphere

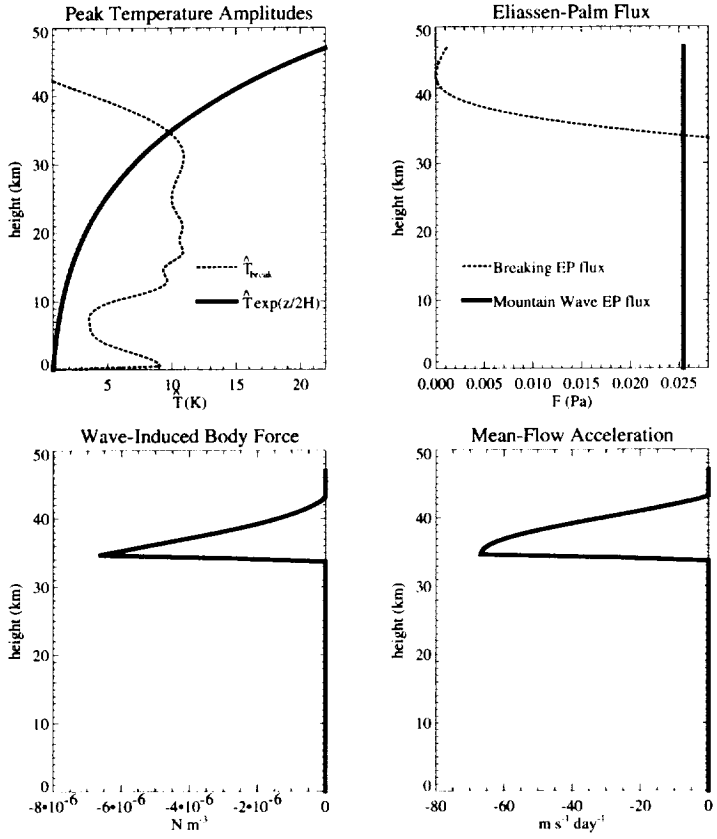

Figure 16: Top row: left panel: thick black curves show the exponential growth of mountain wave temperature amplitude $\hat{T}$ with height, tuned to the 7K amplitude observed at 30 km (Figure 15b). Blue dotted curve shows the calculated breaking amplitude $\hat{T}_{break}$ evaluated from Eq. 2 of *Eckermann and Preusse* [1999] using the wind profile in Figure 15d. Right panel show corresponding Eliassen-Palm (EP) fluxes, evaluated using the formula derived in citation (17) of *Eckermann and Preusse* [1999] (see section 7.1). Note that the nonbreaking EP flux is constant with height. Both figures show that wave breaking sets in just above 30 km, where $\hat{T}$ exceeds $\hat{T}_{break}$. Lower panels show the ensuing EP-flux divergence (left panel) and the mean-flow acceleration that it implies (right panel). Peak decelerations of ~70 m s^{-1} day^{-1} are noted. These calculations assumed no smearing in the CRISTA measurement, λ_h = 400 km and λ_z = 6.5 km.

$$(\lambda_z)_{theory} \approx \frac{2\pi\overline{U}}{N}$$

where $\overline{U}$ is the local horizontal wind speed across the Andean Ridge and N is the background buoyancy frequency. At 15-30 km, $\overline{U} \approx$ 20-23 m s^{-1}, as can be seen from the assimilated data for this region taken from the Data Assimilation Office ESTRATF analyses for 6 November, 1994 at 06:00Z, plotted in Figure 15d. Since $N \approx 0.020$ rad s^{-1}, this yields $(\lambda_z)_{theory} \approx$ 6-7 km according to the mountain wave formula above. The observed vertical wavelength λ_z of the measured wave oscillations in Figure 15b is ~6.5 km at 15-30 km. The close agreement between observed and theoretical vertical wavelengths is powerful evidence that these are stratospheric mountain waves produced by flow across the Andes.

Successive profiles in Figure 15b are separated horizontally by 200 km, from Figure 15c, and adjacent profiles are phase shifted by 180° (Figure 15b). This implies a horizontal wavelength for this stratospheric mountain wave of λ_h = 400/n km, where n is an odd integer. Given the sensitivity of CRISTA to $\lambda_h >$ 100-200 km (depending on the orientation - see Figures 3,4 and 5), then λ_h must be either 130 or 400 km.

These and other comparisons with linear hydrostatic mountain wave theory confirm the reality of these oscillations as mountain waves – see the *Science* paper of *Eckermann and Preusse* [1999], reproduced in section 7.1 of this report. In particular, the analysis outlined there shows that the diminution of activity above 30 km in Figure 15b is likely due to strong dissipation of wave activity. Indeed, this diminution can be used to assess the driving this wave breaking has on the background flow. Results of such calculations are plotted in Figure 16 (see report dated June 18-September 18, 1999 for details of these calculations). We see that there is a sharp onset in wave breaking just above 30 km, with values around 50 m s^{-1} day^{-1} in the westward direction (i.e., against the eastward stratospheric flow in Figure 15d). In this linear saturation model calculation, the mountain wave dissipates entirely below 43 km, where a critical level ($\overline{U}$ = 0: Figure 15d) causes total absorption of wave activity below these altitudes.

2.3.2.2 Modeling of CRISTA Mountain Wave Signals

To assess whether these and other signals in the CRISTA1 and CRISTA2 temperature data can be explained as mountain waves, we need to go beyond simple analytical formulae and compare the results with more detailed models. During this project, we have conducted an extensive series of modeling experiments to both validate and study the stratospheric mountain waves evident in CRISTA data. Detailed descriptions of this work have been provided in previous reports [sections 1.1 and 1.2 of report dated 18 March-18 June, 2000; section 1.4 of report dated September 18-December 18, 1999; section 1.3 of report dated June 18-September 18, 1999; section 1.2 of report dated March 18-June 18, 1999; section 1.2 of report dated December 18, 1998-March 18, 1999]. Results of some of this work have also been published elsewhere [*Eckermann and Preusse*, 1999 (see section 7.1); *Tan and Eckermann*, 2000; *Preusse et al.*, 2000c]. Thus, we will summarize here only the major results and provide a general overview of the three year's worth of work on this topic. Fuller details are to be found in the references above. We present the results in terms of the separate models we have used to study mountain waves in the CRISTA data.

NRL Mountain Wave Forecast Model (NRL/MWFM)

The NRL/MWFM model has been developed in Code 7640 at the Naval Research Laboratory over a number of years. First versions of the model were described by *Bacmeister* [1993] and *Bacmeister et al.* [1994]. This version of the model used two-dimensional hydrostatic irrotational wave equations and simple linear saturation criteria, a model we refer to as MWFM 1.0. Since then we have undertaken a major project to upgrade the model to use three-dimensional ray-tracing equations to model the three-dimensional radiation of mountain waves governed by a nonhydrostatic rotational dispersion relation. Wave amplitudes are governed by a wave action conservation equation with convective and dynamical saturation criteria under the same approximations. General information on these upgrades is provided by *Eckermann and Preusse* [1999] and *Eckermann et al.* [2000a, 2000c], while the theoretical underpinnings of these model extensions were outlined by *Broutman et al.* [2000]. This new version of the model is known as MWFM 2.0, and was used for the first time in detailed mountain wave forecasting during winter of 1999-2000 in support of NASA's SAGE III Ozone Loss and

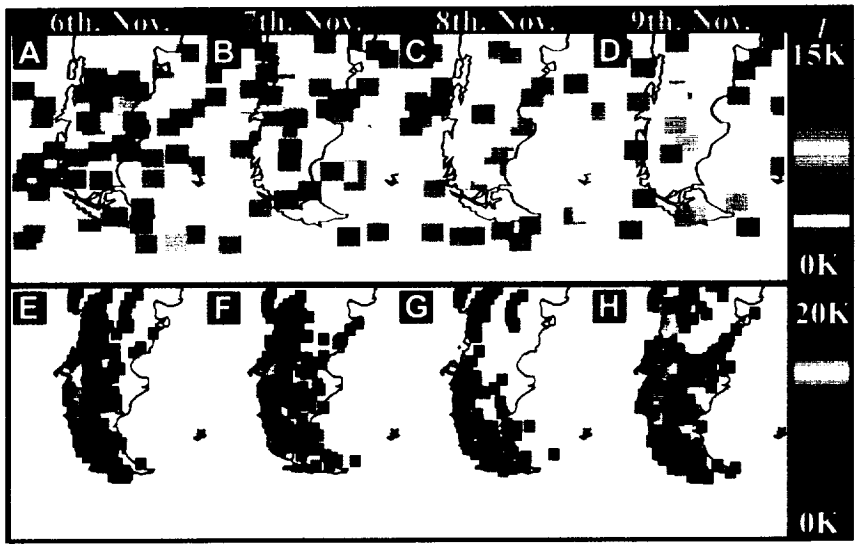

Figure 17: $\hat{T}$ amplitudes over southern South America at an altitude of 25 km from 6th-9th November, 1994 (panels **A-D**, respectively), plotted as color pixels at the profile's limb tangent location. Raw values were scaled by their vertical wavelength-dependent one-dimensional visibility function (see section 2.2) to correct for observational degradation of amplitudes. Beneath each panel is a corresponding MWFM 2.0 "hindcast" using DAO assimilated winds and temperatures at 12:00 UT for these dates (panels **E-H**). Modeled mountain waves with λ_z<5 km were not plotted since CRISTA is not sensitive to them. The color scales are linear. Pixels are plotted in order of ascending amplitude, and are sized to maximize coverage and visibility while minimizing pixel overlap. Plot after *Eckermann and Preusse* [1999] – see section 7.1.

Validation Experiment (SOLVE)[1] For further background information on the MWFM model, see http://uap-www.nrl.navy.mil/dynamics/html/mwfm.html. All the results shown hereafter were generated using the latest MWFM 2.0 model.

We have used the MWFM in "hindcast mode" to model mountain waves in the CRISTA data. In this mode, we take large-scale analysis winds and temperatures for dates appropriate to the CRISTA mission to "hindcast" mountain wave amplitudes in the stratosphere. These results are compared with global or regional maps of the $\hat{T}$ amplitudes actually measured by CRISTA during these times. In these comparisons, short wavelength mountain waves are removed from the analysis. This is based on the importance of considering such effects to make effective and meaningful comparisons between satellite observations and theory, as proposed by *Alexander* [1998] and verified experimentally in section 2.2.

An example from CRISTA1 is shown in Figure 17. Top row shows $\hat{T}$ amplitudes from CRISTA over November 6-9, 1994, while bottom row shows corresponding MWFM hindcasts using DAO assimilated winds and temperatures at 12Z on these dates. Note that simulated waves with vertical wavelengths < 5 km were removed from the MWFM results, since CRISTA is not sensitive to them (see Figure 3). We see excellent correlations between actual CRISTA data and the MWFM hindcasts. The activity in both is large on the 6th, wanes on the 7th and 8th, then reintensified on the 9th. This is good further evidence that this activity over southern South America is due to mountain waves forced by flow across the Andes. Further evidence

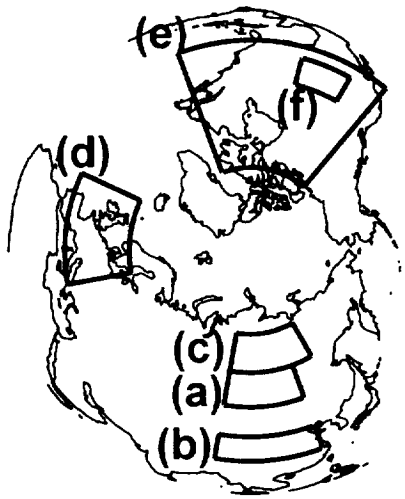

Figure 18: Geographical locations where CRISTA1 data and MWFM hindcasts are analyzed in Figure 19.

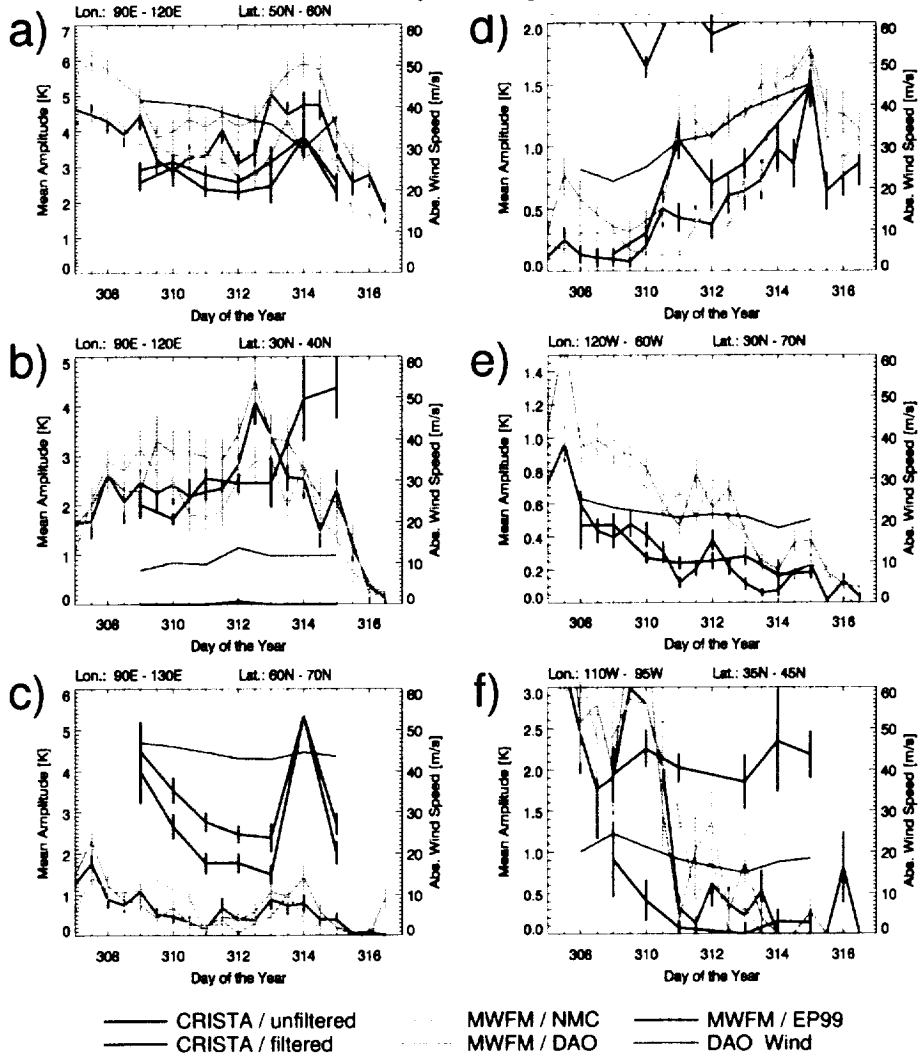

Figure 19: Time series from regions in Figure 18 of filtered (navy curve) and unfiltered (black curve) CRISTA $\hat{T}$ data, and MWFM hindcasts using NCEP analyses (aqua), DAO E0106 analysis (orange), DAO ESTRATF analysis (red). Also plotted are local DAO wind speeds (pink, axis scale to right). Error bars are standard deviations. All plots are for an altitude of 10 hPa

[1] See http://uap-www.nrl.navy.mil/dynamics/html/mwfm_solve1.html

based on accumulated wavelength estimates over the entire CRISTA 1 mission period is provided in section 7.1 by *Eckermann and Preusse* [1999].

We also studied possible mountain wave signals in the northern hemisphere. We studied time series of CRISTA 1 and MWFM hindcasts at six northern hemisphere locations shown in Figure 18, labeled (a) through (f). Time series of $\hat{T}$ data from CRISTA, as well as time series of various MWFM hindcasts, for these regions are shown at an altitude of 10 hPa in Figure 19. The local DAO wind speeds are also plotted with pink in each panel. The comparisons among data and hindcasts in some regions are particularly good, such as geographical regions "a" (central Siberia) and "d" (northwestern Europe), while the comparisons are less compelling elsewhere (e.g., region "c," northern Siberia). These comparisons lead us to believe that fluctuations in certain broad regions of the northern hemisphere stratosphere during the CRISTA1 mission period are consistent with stratospheric mountain waves.

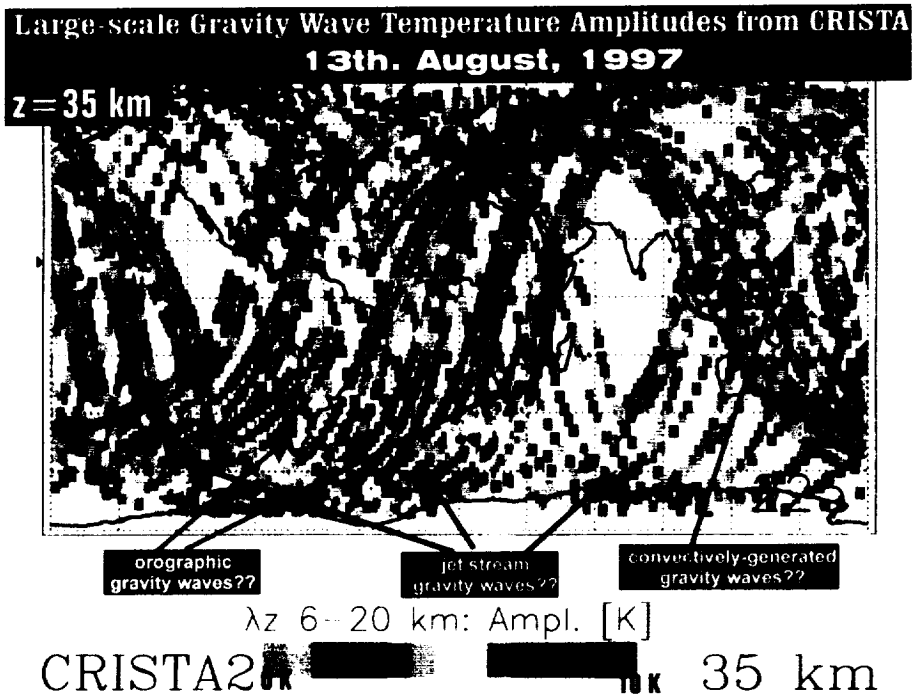

Figure 20: CRISTA peak temperature amplitudes on August 13, 1997 at an altitude of ~35 km. Regions highlighted by aqua box indicate possible zones of stratospheric mountain wave activity. Vertical wavelengths here are in the range 6-20 km.

We have initiated similar studies of fluctuations in data from the CRISTA2 mission during 7-16 August, 1997. Wave activity from this mission showed more activity concentrated in broad regions around the southern polar vortex, as shown in Figure 20. Other regions of activity are analyzed in more depth in later sections. However, here on August 13, 1997 at 35 km, we note regions over southern South America (as for CRISTA1) and South Africa which may be associated with mountain waves. Results in Figure 20 are plotted within the range of resolved vertical wavelengths between 6 and 20 km.

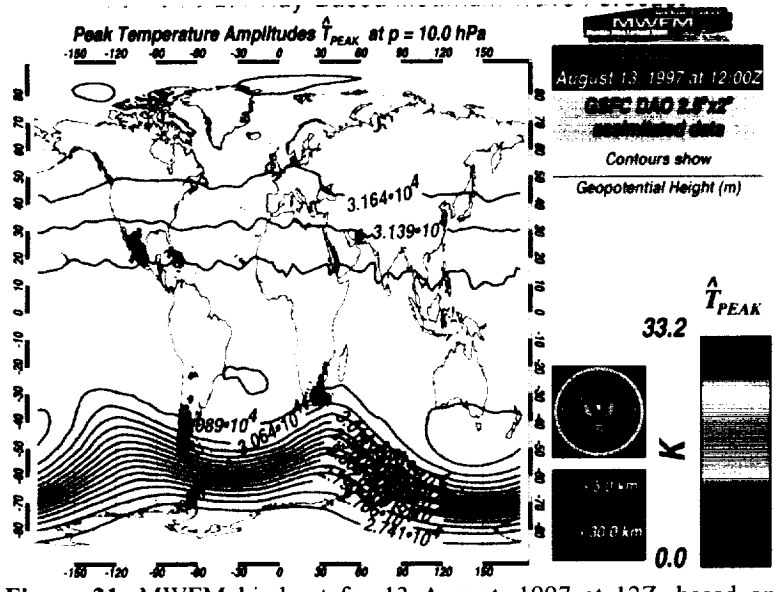

Figure 21: MWFM hindcast for 13 August, 1997 at 12Z, based on DAO assimilated global winds and temperatures for the period. Vertical wavelengths > 5 km and horizontal wavelengths > 30 km only are plotted.

Figure 21 shows a corresponding NRL/MWFM hindcast simulation at 10hPa for August 13, 1997 at 12Z, based on DAO assimilated global winds and temperatures for this period. Pink contours show geopotential heights, revealing the intense wavenumber-2 vortex structure that existed in the southern hemisphere stratosphere at this time. The hindcasts reveals regions of mountain wave activity over the southern Andes and also over South

Africa, much as observed in Figure 20. Note again here that only longer wavelength waves are retained in these hindcasts, to make more appropriate comparisons with the waves resolved by CRISTA. The presence of mountain waves over southern Africa is associated with the bulging of strong vortex edge winds into this region at the time (evidenced by the closely spaced pink geopotential height contours) via a wavenumber 2 pattern which provides a strong wind channel for mountain waves to reach the stratosphere with long vertical wavelengths (necessary for them to be resolved in the CRISTA2 limb-scanned temperatures). We even see additional evidence for mountain wave activity in the northern hemisphere over eastern Mexico in both the MWFM hindcast map and the CRISTA 2 data. Thus, we have good evidence that mountain waves were evident in the stratosphere and were measured by CRISTA during the CRISTA2 mission period.

Two-Dimensional Mesoscale Model Simulations (NRL/UNSW Model)

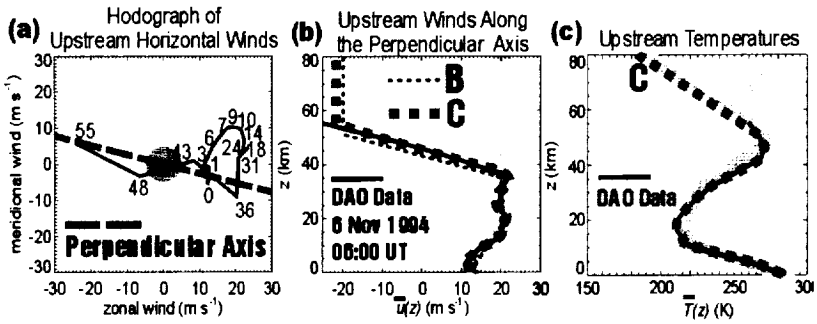

Figure 22: (a) Hodograph of horizontal winds upstream of the Andes from DAO assimilated data on 6th. November, 1994 at 06:00 UT. The altitudes (in kilometers) of each wind value are labeled along the hodograph trace. Orientation of the model experiment axis is shown with broken curve; (b) black solid curve shows upstream DAO wind profile along the perpendicular axis. Other labeled curves show model wind profiles used in Experiments A, B and C using the mesoscale model; (c) vertical profile of upstream DAO temperatures (solid black curve), and the model curves used in Experiments A, B and C.

While a great deal of work was expended during this project on this particular modeling project, we will only summarize the major final findings of this work, since the full study has been outlined at length in previous quarterly reports (e.g., reports dated 18th September-18th. December, 1999, 18th. December 1999-18th. March, 2000), and has also been published elsewhere in the peer-reviewed literature [*Tan and Eckermann*, 2000]. In short, we developed a new two-dimensional nonhydrostatic compressible mesoscale model and applied it to simulate mountain waves observed over the southern Andes in CRISTA1 data (see Figures 14, 15 and 17). The model equations and numerics are set forth in *Tan and Eckermann* [2000]. Using the model, we formulated and performed three experiments, labeled A, B and C, which used wind and temperature profiles as shown in Figure 22. Experiment A used an idealized wind profile that omitted the westward shear layer in the DAO assimilated wind profile above 35 km (Figure 22b). This wind profile is taken from a region upstream of the Andes, shown as the blue "upstream point" in Figure 23. This control experiment allowed us to study mountain wave generation and propagation to stratosphere-mesosphere levels above the Andes without the complication of critical-level effects, and also allowed us to tune the sponge layer in the model. In Experiment B, a linear westward shear layer was introduced above 35 km, yielding a critical level (zero mean wind line) at z ~43 km. Experiment B allowed us to introduce the critical layer, while maintaining an identical atmospheric situation to Experiment A below 35 km. To this end, both experiments used background temperatures from the 1976 U.S. Standard Atmosphere at mid-latitudes, which fit the upstream DAO temperatures from ~0-55 km quite well (Figure 22c). Experiment C used cubic spline fits to the upstream DAO wind and temperature profiles from 0-55 km. This yielded a zero wind line at z ~46 km, slightly higher than in Experiment B. Lacking any DAO data to fit above 55 km, from 55-80~km we used constant winds (Figure 22b) and a linear temperature gradient equal to that in Experiments A and B (Figure 22c).

In all three experiments, mountain waves entered the upper stratosphere after a few hours and produced overturning isentropes after ~6 hours. Figure 24 plots contours of the total (wave + mean) potential temperature $\Theta(x,z,t)$ after t = 18 hours in each experiment over the orographic region of the

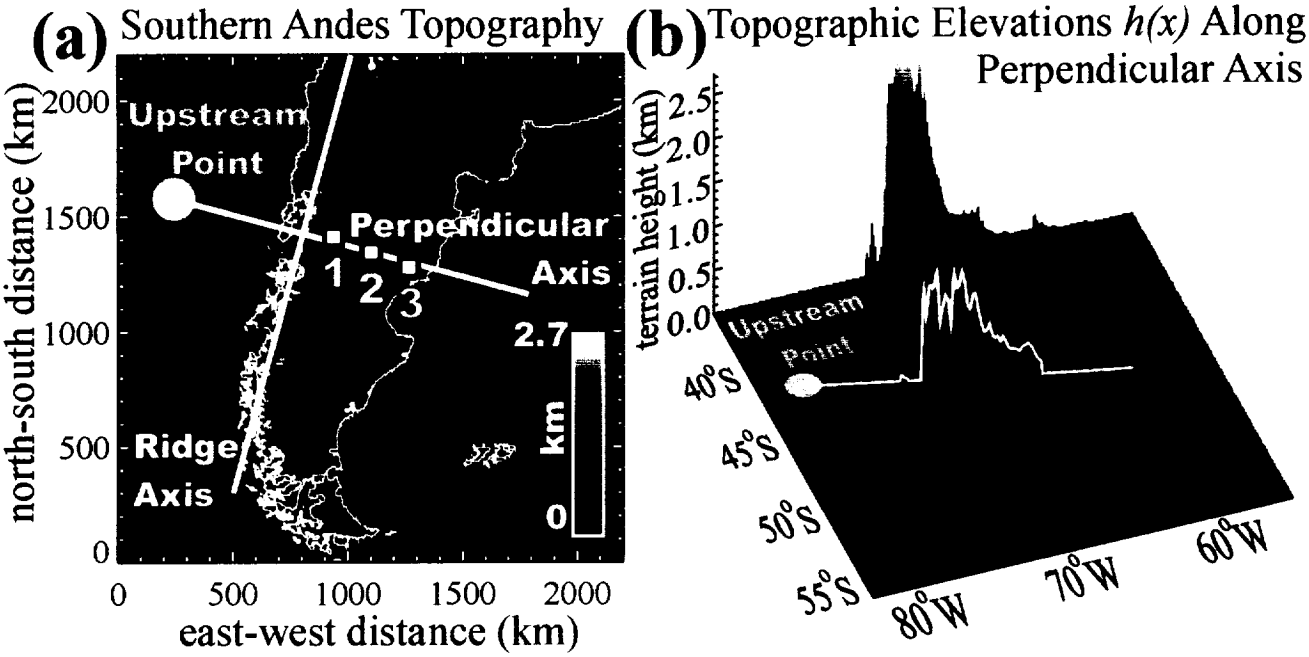

Figure 23: Topographic elevations over southern South America, plotted as (a) filled contours in Cartesian coordinates, (b) three-dimensional elevations in Mercator coordinates. Squares labeled 1,2 and 3 in (a) show locations of temperature profiles acquired by CRISTA. Raw elevations *h(x)* along the perpendicular axis in (a) are plotted in (b), and represent the topography used in the model simulations. The blue dot in both figures is the upstream point where mean winds and temperatures are computed from DAO data in Figure 22.

Andes. Colors show contours of temperature perturbations $T'(x,z,t)$. We see that the critical levels in Experiments B and C efficiently absorb mountain waves, and yield rapid wave shortening and intense breaking at closely underlying altitudes. Despite the different wind profiles and the significant amounts of overturning (nonlinearity) and mixing by this time, the large-scale wave structures below 35 km look very similar in all three experiments.

The wave fields evolve significantly with time, as illustrated in Figure 25 using results from Experiment C. The middle atmosphere is dominated initially by short horizontal wavelengths, which trigger vigorous overturning and mixing by ~8 hours. The turbulent zones persist and seem to move downstream after 10 hours. Thereafter, progressively longer horizontal wavelengths come to dominate

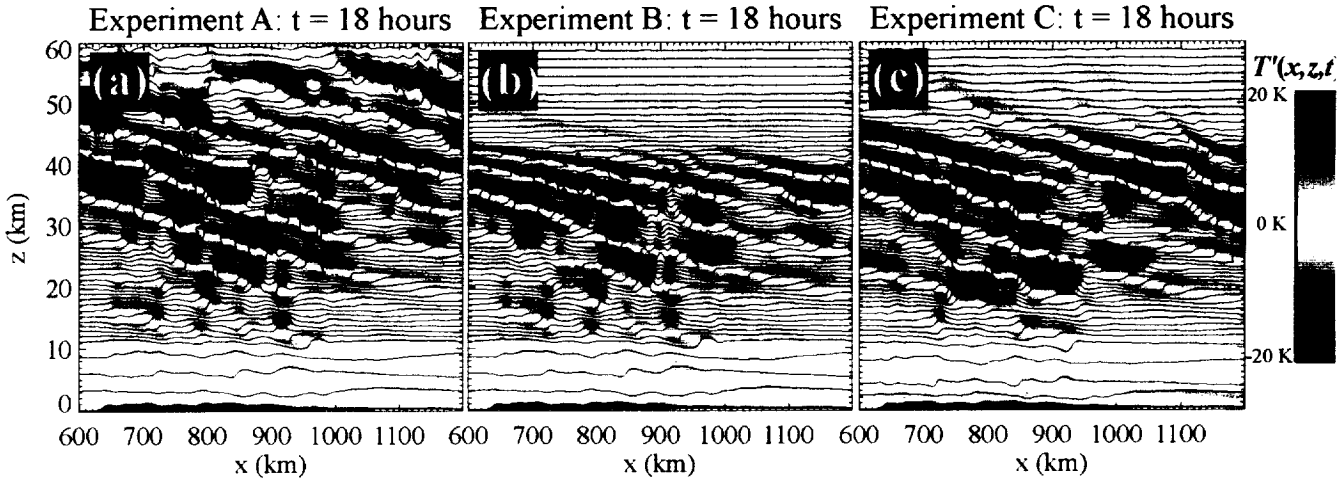

Figure 24: Temperature fields 18 hours into Experiments A, B and C. Contours show isentropes $\Theta(x,z,t)$, with constant logarithmic separation between adjacent contours. Temperature perturbations $T'(x,z,t)$ are overlayed using the blue-red color scheme shown to the right. Underlying topography is shown in black.

the wave field, and less vigorous overturning is evident. After 24 hours, waves at lower stratospheric levels are suppressed compared to their earlier intensities.

The wavelength selection and the resultant group velocities explain the wavelength selection observed here in Figure 24, as well as the time evolution of dominant horizontal wavelengths evident in Figure 25. These theoretical arguments were set forth in previous reports, as well as by *Tan and*

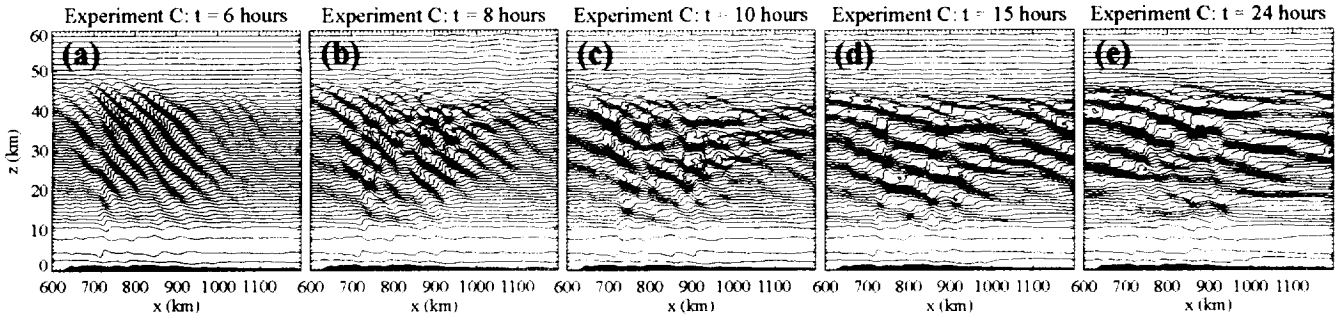

Figure 25: Contours of isentropes $\Theta(x,z,t)$ from Experiment C after t = 6, 8, 10, 15 and 24 hours. Same constant logarithmic separation between contours is used in each panel. Underlying topography is shaded.

Eckermann [2000], and will not be repeated here. The simulations out to 24 hours in Figure 25e show much longer horizontal wavelength waves in the stratosphere than earlier, consistent with the long wavelength waves that appear to dominate the response and need to be present in order for the CRISTA and MLS limb scans to resolve them.

The general form of the profiles over the Andes compares favorably with the CRISTA data. Figure 26 plots a sample temperature perturbation profile from Experiment C at x = 845 km, a location between points 1 and 3 over the Andes where CRISTA acquired these profiles, as shown in Figure 23a. The CRISTA profiles at these points are overlaid in Figure 26, taken from Figure 15b. The wavelength, amplitude and general height variation of the model profile are all quite similar to the data. Oscillations in Experiment C seem to penetrate slightly higher prior to shortening and dissipating below the critical layer. Note too that the amplitudes of the CRISTA profiles are probably underestimated due to instrumental effects, and that CRISTA cannot resolve any waves of vertical wavelength less than ~3-5 km [*Eckermann and Preusse*, 1999; see Figure 3].

These results, which are not tuned in any way but allowed to run from "first principles" using a 2D nonlinear mesoscale model constrained to background conditions at this time, generate mountain waves with many similarities to those measured by CRISTA on 6 November, 1994. This provides powerful evidence that CRISTA indeed measured long wavelength mountain waves over the Andes at this time.

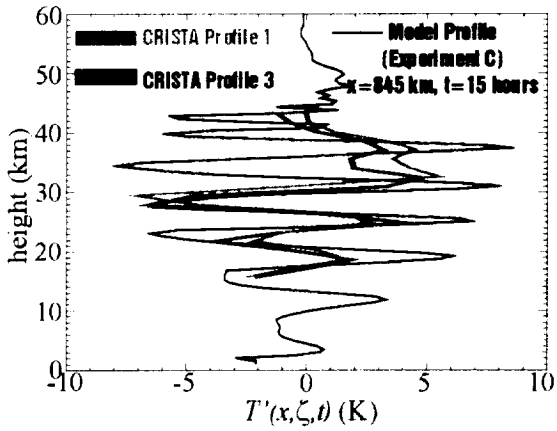

Figure 26: Black curve shows a vertical profile of temperature perturbations at x = 845 km, 15 hours into Experiment C. Two shaded solid curves reproduce the temperature perturbation profiles acquired by CRISTA at locations 1 and 3 in Figures 15a, 15b and 23a.

Three-Dimensional Mesoscale Model Simulations (MM5)

In collaboration with Dr. Andreas Dörnbrack of the Deutsche Institut für Luft und Raumfahrt (DLR) in Oberpfaffenhofen, Germany, we have also used a version of the Penn State Mesoscale Model 5 (MM5) to provide hindcasts of large-scale mountain waves for the CRISTA1 mission, in a similar way to what has been done previously in the stratosphere over northern Scandinavia [e.g., *Dörnbrack et al.*, 1998] and Greenland [e.g., *Leutbecher and Volkert*, 2000]. Given the MM5 model's ability to simulate

the largest scale mountain waves, which CRISTA and MLS measure, then we began discussions about performing MM5 simulations over southern Scandinavia during the CRISTA 1 mission period to see if this model could cast light on the three-dimensional nature of mountain waves radiated into the stratosphere from this region.

In these simulations, the MM5 model was initialized using archived analysis ECMWF winds and temperatures for 5th. November, 1994 at 0:00 Z, and then was integrated for 36 hours thereafter in dry mode with an upper level of ~28 km and a horizontal grid resolution of ~27 km. The temperature results are shown in Figure 27c at an altitude of 30 hPa. Another nested grid simulation was conducted which was identical to the one in Figure 27c, but increased the effective horizontal resolution. Corresponding results from that simulation are shown in Figure 27d. As for the 2D mesoscale simulations, we see a long stratospheric mountain wave emerge in the MM5 results, of a horizontal scale long enough to be resolved by CRISTA (see Figure 3). Interestingly, however, these waves in the MM5 output are titled somewhat in phase with respect to the Andean topography, as evident from inspecting Figures 23 and 27c,d. The reason for this may be due to surface wind patterns that bulge southward from the Andes and then northward past the Andes in response to the larger Andean obstacle heights to the north [see, e.g., *Seluchi et al.*, 1998]. Another reason could be the sharp latitudinal shear in the vortex winds here that may refract waves latitudinally. It might also be caused by flow across the "hook"-like topography near the southernmost tip of South America (see Figure 23b). However, since these orientations persist even to the north, the exact reason for this in the MM5 simulations is unclear and is a somewhat unexpected finding.

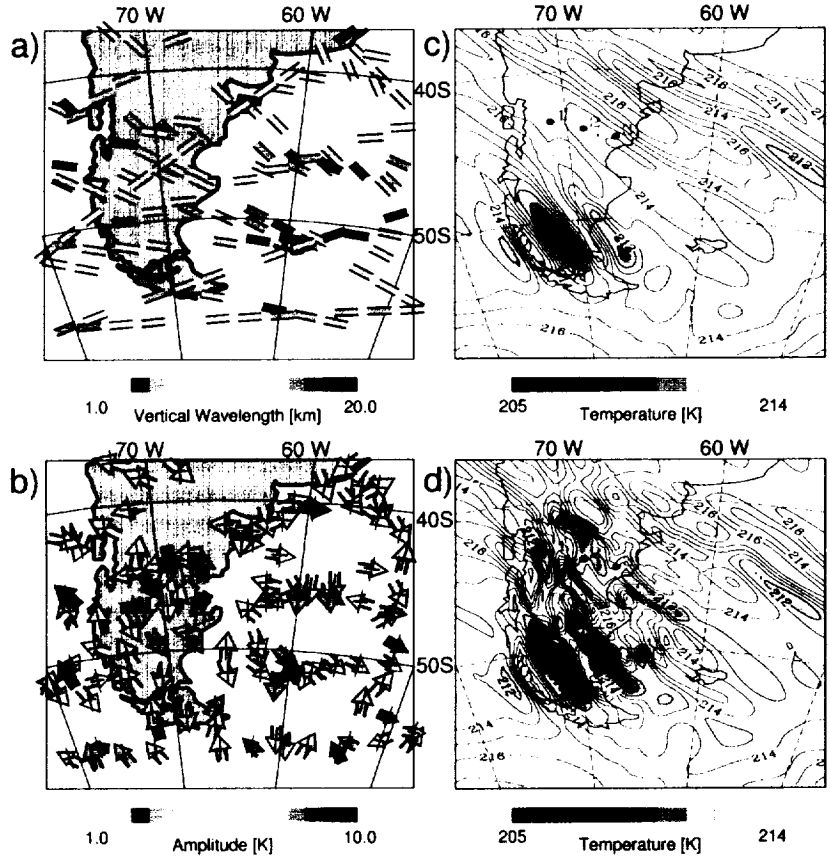

Figure 27: Gravity wave activity over southern South America at 30 hPa. The vertical wavelength in the CRISTA1 profile and the viewing direction of the instrument are displayed in (a). Panel (b) shows CRISTA wave amplitudes (color scale), along with wave phase depicted by the orientation of the arrow. Panel (c) shows contours of temperature at 30 hPa 36 hours into the MM5 simulation for this period, while Panel (d) shows results using a nested grid simulation to increase the horizontal resolution to ~14 km. Red dots show locations of the 3 CRISTA1 profiles in Figures 15b, 15c and 23a.

Activity at 30 hPa from CRISTA1 data at this time are profiled in a more in-depth way in Figures 27a and 27b, showing wavelength, phase, amplitude and telescope limb scan directions, all of which aid in assessing how fluctuations like those seen in the MM5 simulations might be resolved by the CRISTA1 limb scan data. We see that the interesting 45° tilt of the MM5 wave fronts with respect to the Andean Ridge axis in Figures 27c and 27d assists in CRISTA resolving the large waves noted in the three profiles noted in Figures 15, 23a and 26, since, as noted from Figure 27a and 27b, the telescopes observed these waves roughly along a 45° orientation that runs roughly parallel to a wave phase front in Figure 27c and 27d, a situation akin to the "best case" observing scenario in Figure 4. The absolute magnitudes of the temperature amplitudes are similar, with MM5 values generally a little lower. We also see evidence of significant downstream penetration

of mountain wave activity in both the CRISTA1 data and the MM5 hindcast simulation. However, the major difference is that the activity in the MM5 simulations is concentrated near the southernmost tip of South America, whereas in the CRISTA data for November 6, the largest burst is further north. Nonetheless, the comparisons are generally quite good, and add further weight to our accumulating body of evidence that these fluctuations in the CRISTA1 temperature channel over the southern Andes are due to long wavelength stratospheric mountain waves. Initial results of this work are being written up as part of a major paper detailing the mountain wave analysis and modeling from the CRISTA1 mission [*Preusse et al.*, 2000c].

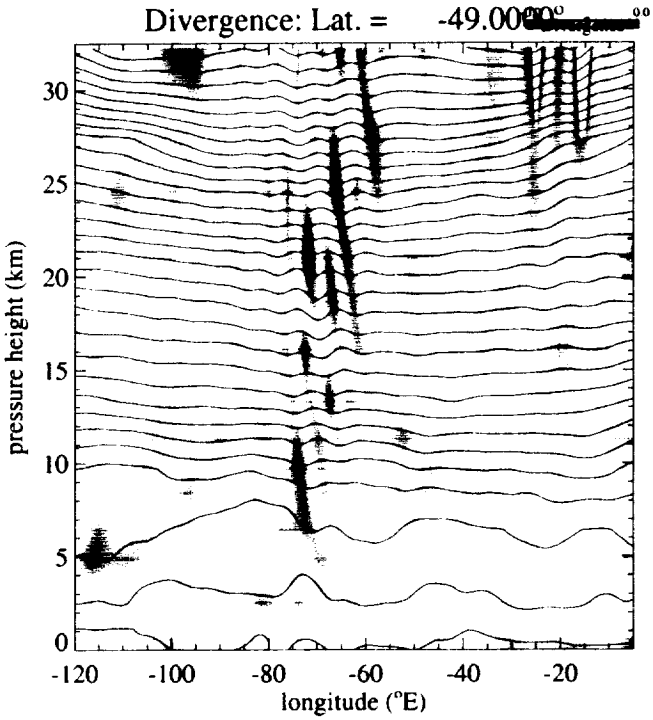

Figure 28: Longitude-height section of divergence D calculated from 1°x1° NCEP global analyses for August 12, 1997 along a latitude of 49° S. In the longitude range 70° – 80°W, corresponding to the southern Andes, we see wave fluctuations with phase lines that slope upwards and westward, consistent with a mountain wave propagating westward with respect to the eastward background winds.. Note the increase in vertical wavelength as the wave propagates into the strong eastward vortex winds in the stratosphere. Black contours show isentropes, which also reveal perturbations due to these waves.

NCEP Global Analyses

Around 1995, the National Centers for Environmental Prediction (NCEP) global upgraded the output from their global spectral forecast model to a 1°x1° resolution. Accordingly, NCEP started issuing 1°x1° analysis fields in support of these new forecasts, in addition to the standard 5°x2° fields that have been issued for many years, as well as the 2.5°x2.5° fields that are being issued as part of the NCEP 40-year reanalysis project [*Kalnay et al.*, 1996]. At mid-latitudes, 1° longitudinal resolution corresponding to a spatial resolution Δx ~75 km, and thus, given that CRISTA1 cannot resolve waves much shorter than 200 km, this raises the interesting possibility that waves evident in the CRISTA temperature channel might also be evident in these new high-resolution NCEP global analyses. Since the CRISTA1 mission took place in November, 1994, just before these analyses were issued, we cannot test this for the CRISTA1 mission, but we can test these ideas during the CRISTA2 mission period of August, 1997.

The exact analysis methods we used are discussed at length in the following section detailing potential jet stream-related activity in the CRISTA2 data. Suffice to say here that we analyze divergences D in the NCEP analyses, which often show gravity wave fluctuations directly [e.g., *O'Sullivan and Dunkerton*, 1995]. Figure 28 shows a longitude-height section along the Andes at a latitude of 49°S on August 12, 1997. We see coherent wave fluctuations in the divergences D with phase lines that slope upward and westward,

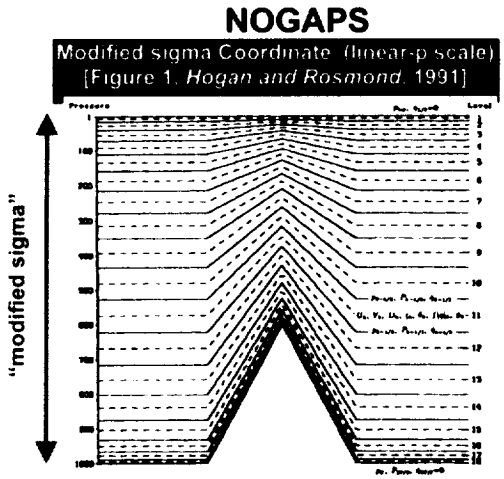

Figure 29: Illustration of how the sigma coordinate transformation over topography extends to the top model altitude (based on NOGAPS model of *Hogan and Rosmond* [1991]). The pressure scale here in linear, which accentuates the obstacle effect

consistent with upward propagating quasi-stationary mountain waves propagating westward with respect to the eastward background flow.

The identification of this activity as a mountain wave by this method is important, since we might also expect some residual fluctuations within the analysis due to the fact that the NCEP spectral model uses sigma coordinates. While the sigma coordinate deals well with arbitrary topography near the ground, it leads to perturbations in fields like geopotential heights all the way to the model top when model fields are regridded onto pressure coordinates, due to the topographic elevations, as shown schematically in Figure 29. Other models, which concentrate more on the stratosphere, use a so-called "hybrid coordinate," which transitions from sigma to pressure coordinates at some safe level above the topography, often somewhere near the tropopause. However, the NCEP model does not do this since the stratosphere is not a prime focus of its forecasts, and thus "wiggles" over mountainous regions like the Andes are expected due to the sigma coordinate effect. However, as we see from Figure 29, such sigma coordinate "wiggles" follow the topographic shapes, and do not exhibit any sloping phase line structures like those seen in Figure 28. Thus, we conclude that the "wiggles" in Figure 28 are mountain waves generated by the NCEP global model, and are not artifacts due to sigma coordinate residuals. This also agrees with the NRL/MWFM hindcast simulation for 13 August, 1997 presented in Figure 21, and the enhanced fluctuations in the CRISTA2 temperature data in this region noted in Figure 20.

The activity at ~20°W in Figure 28 is different to the mountain wave activity, and is associated with a band of wave activity in the NCEP analyses that appears to be radiated by the jet and follows the stratospheric vortex edge flow. This is discussed fully in the next section (see, e.g., Figure 32b,d).

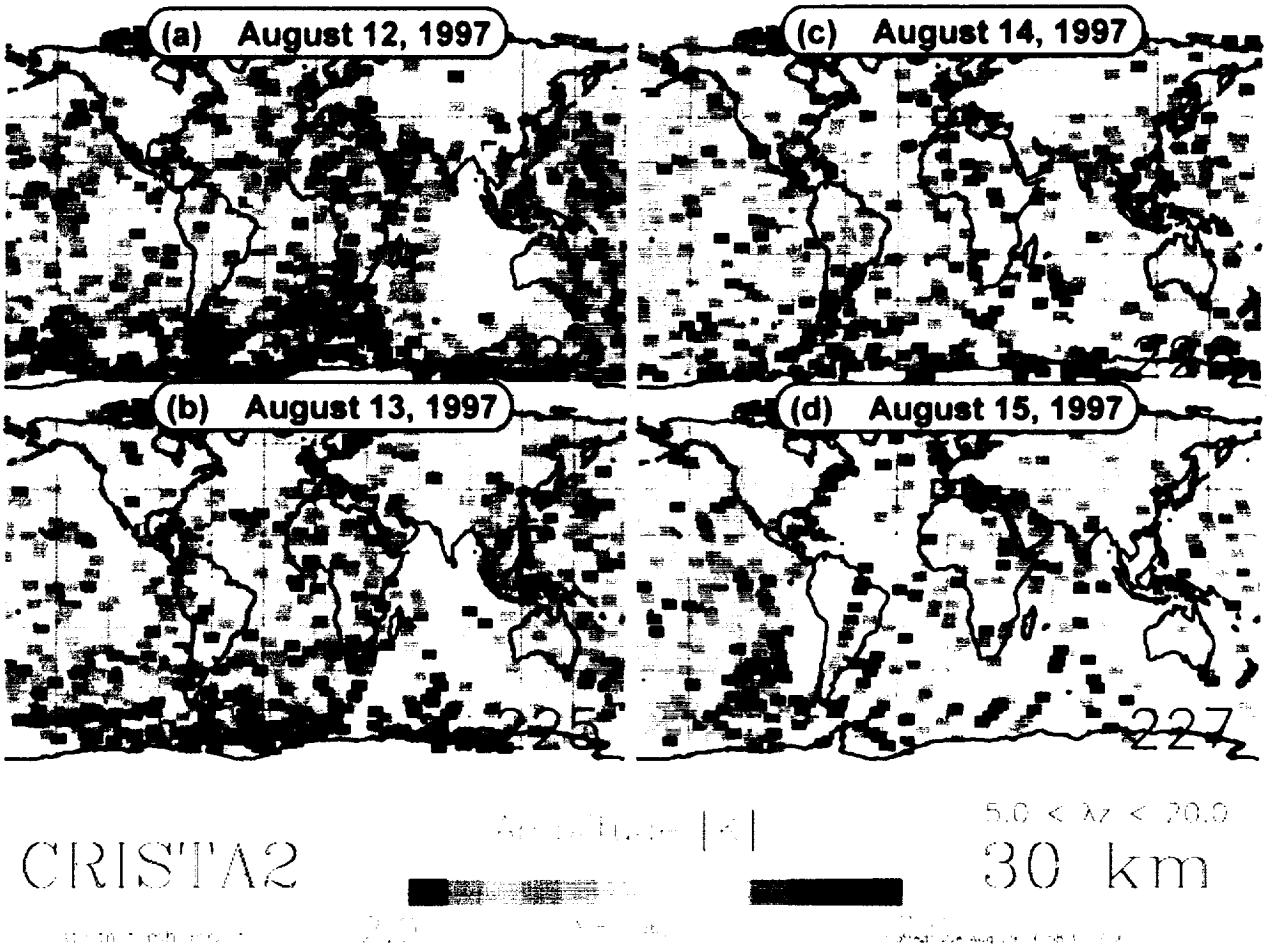

Figure 30: Gravity wave temperature amplitudes during Days 224-227 (August 12-15, 1997) of the second CRISTA-SPAS mission. Results show wave amplitudes in the range 2-7K at a height of 30 km, showing vertical wavelengths in the 5-20 km range.

2.3.3 Stratospheric "Vortex Gravity Waves"

Figure 30 shows a time series of four successive days of peak amplitudes $\hat{T}$ of small-scale temperature fluctuations due to gravity waves in CRISTA2 data, isolated as before using the MEM/HA analysis method applied to Kalman-detrended global temperature fields for each day of the mission. As noted in Figures 20, 21 and 28, activity over the southernmost regions of South America and Africa appears to be due to long stratospheric mountain waves. However, unlike the CRISTA1 mission which did not show a great deal of other activity at these southern latitudes (see, e.g., Figure 14), the stratospheric activity during CRISTA2 in Figure 30 shows broad regions of activity at southern mid-latitudes that exist well away from significant topography or even land mass. These mysterious "vortex gravity waves" are the most notable feature of the Southern Hemisphere CRISTA2 gravity wave data in Figure 30, and require dedicated study.

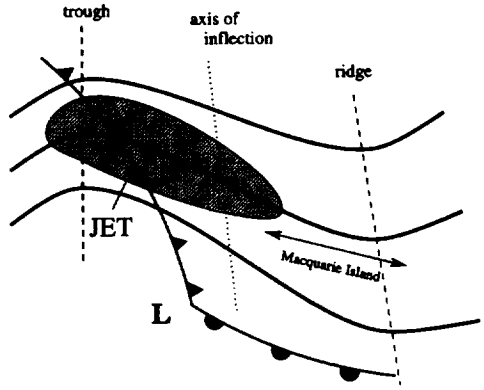

Figure 31: Synoptic setting at 300 hPa for gravity wave radiation by the jet, transposed for southern hemisphere [after *Guest et al.*, 2000]. Downstream of a trough, as height contours spread apart and air parcels decelerate, winds become strongly ageostrophic in the shaded region, and radiate long low-frequency gravity waves as the jet region relaxes to a state of balance.

Similar enhancements of stratospheric gravity wave activity in and around the polar vortices have been inferred from MLS data [*Wu and Waters*, 1997; *Jiang and Wu*, 2000], as well as LIMS data [*Fetzer and Gille*, 1994] and data from ground-based lidar instruments [e.g., *Whiteway*, 1999; *Duck and Whiteway*, 2000]. The major source(s) of these waves remain(s) undetermined. In the northern hemisphere (Arctic), it has been argued that wave variance enhancements that correlate with intensifying vortex flow overhead are due to increased transmission of mountain waves into the stratosphere [e.g., *Whiteway et al.*, 1997; *Whiteway*, 1999], although correlations with tropospheric jets have also been noted [*Duck and Whiteway*, 2000] Since most of the southern hemisphere vortex activity in Figure 30 is over open ocean, these southern hemisphere features cannot be explained by mountain waves alone (compare Figures 21 and 30). Thus, we must consider other sources in trying to explain these waves in the CRISTA2 data.

We have considered unstable jet stream dynamics as a potentially viable source of the activity in around the southern vortex that we see in the CRISTA 2 data in Figures 20 and 30. This is because the region at ~40-50°S where stratospheric vortex winds peak is also characterized at lower levels by strong jet stream winds and evolving baroclinic wave systems, storms and fronts (the so-called "roaring 40's" region). *Guest et al.* [2000] showed that large-scale gravity waves observed in radiosonde data over Macquarie Island (54°S, 159°E) were probably due to inertia gravity waves radiated from jet exit regions, rather than by flow across the island's orography.

Modeling or identifying global jet-related wave sources is much more difficult than it is for mountain waves: indeed, it is probably fair to say that the theory of waves generated from jet streams is still not fully developed [see, e.g., *Vadas and Fritts*, 2001]. However, *Uccellini and Koch* [1987] noted a reproducible synoptic setting for long wavelength gravity waves radiated from the jet: the situation appropriate to the southern hemisphere is shown in Figure 31. Winds in the hatched regions become highly ageostrophic and decelerate, radiating inertia gravity waves in response. Such waves have been observed in idealized global spectral model simulations [e.g., *O'Sullivan and Dunkerton*, 1995] as well as in data and numerical weather forecasts [e.g., *Koch and O'Handley*, 1997]. Within spectral numerical weather prediction model models, it is usual to deal with prognostic equations for the horizontal velocity divergence $D = \vec{\nabla}_h . \vec{V}$, where $\vec{V} = (u, v)$ is the horizontal velocity. The prognostic time tendency equation, in pressure coordinates, then becomes

$$\frac{dD}{dt} = -D^2 - \frac{\partial \vec{V}}{\partial p}.\vec{\nabla}_h \omega + \dot{D}_{nonlinear}$$

where

$$\dot{D}_{nonlinear} = 2J(u,v) - \beta u + f\zeta - \nabla_h^2 \Phi$$

[e.g., *Moore and Abeling*, 1988]. Here $d/dt = \partial/\partial t + \vec{V}.\vec{\nabla}_h + \omega\partial/\partial p$ is the total advective time derivative, ω is the vertical velocity (transformed to the pressure coordinate), J is the Jacobian operator, such that $J(u,v) = (a\cos\phi)^{-1}[\partial u/\partial\lambda.\partial v/\partial\phi - \partial v/\partial\lambda.\partial u/\partial\phi]$, ζ is the relative vorticity, f is the Coriolis parameter, $\beta = \partial f/\partial y$ and Φ is the geopotential. For stable or "balanced" jet stream dynamics, the 4 nonlinear tendency terms in $\dot{D}_{nonlinear}$ above sum to zero to a very good approximation [*Moore and Abeling*, 1988] and this is sometimes referred to as the nonlinear balance equation, or NBE for short. In jet exit regions like Figure 31, however, $\dot{D}_{nonlinear}$ can be significantly nonzero, and thus can serve as an identifier of unstable regions were long mesoscale gravity waves may be radiated by unbalanced jet stream dynamics. Indeed, *Koch and O'Handley* [1997] suggested such a calculation as a way to forecast trapped mesoscale gravity waves that can produce locally severe weather. In other words, $\dot{D}_{nonlinear}$ may serve as a large-scale proxy for identifying synoptic regions where smaller-scale gravity waves radiate from the jet.

To investigate this, we use high-resolution global analyses issued by the National Centers for Environmental Prediction (NCEP). *Kalnay et al.* [1996] provide background on the NCEP reanalyses in the context of their specific 40-year reanalysis project. However, those reanalysis products are issued on a 2.5°x2.5° global grid, whereas we need better resolution than this to resolve long wavelength gravity waves, as shown for our analysis of mountain waves in Figure 28 and the accompanying discussion. Thus, we again focus on the 1°x1° analysis product that has been issued since ~1995 in support of the current 1°x1° global numerical weather predictions from the NCEP global spectral model. These products are issued once daily (at 0Z) on 22 pressure levels from sea level (1000 hPa) up to 10 hPa.

We have studied these NCEP products throughout the second CRISTA-SPAS mission (7-16 August, 1997). First, we computed divergences D directly from these pressure-gridded global NCEP datasets. These estimates should be quite reliable since the NCEP global spectral

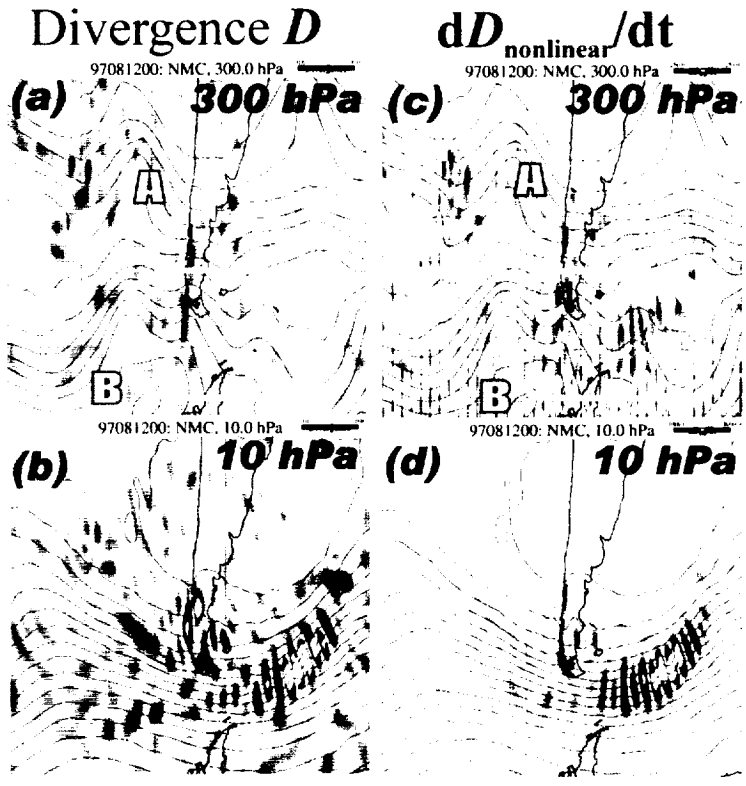

Figure 32: Divergences D (left column) and the nonlinear divergence tendency term, $\dot{D}_{nonlinear}$ evaluated at 300 hPa (top row) and 10 hPa (bottom row) using data from 1°x1° NCEP reanalyses for August 12, 1997 at 0Z. The red-blue color scale is shown top-right, with white showing zero, red most positive and blue the most negative values. Largest divergences are 10^{-6} s^{-1} and $\dot{D}_{nonlinear}$ values are capped at $2.5x10^{-8}$ s^{-2} in panel c and $10x10^{-8}$ s^{-2} in panel (d). Black lines show geopotential height contours. Yellow regions show synoptic settings resembling Figure ZP, which yield apparent propagating gravity wave disturbances.

$$\frac{dD}{dt} = -D^2 - \frac{\partial \vec{V}}{\partial p}.\vec{\nabla}_h \omega + \dot{D}_{nonlinear}$$

where

$$\dot{D}_{nonlinear} = 2J(u,v) - \beta u + f\zeta - \nabla_h^2 \Phi$$

[e.g., *Moore and Abeling*, 1988]. Here $d/dt = \partial/\partial t + \vec{V}.\vec{\nabla}_h + \omega\partial/\partial p$ is the total advective time derivative, ω is the vertical velocity (transformed to the pressure coordinate), J is the Jacobian operator, such that $J(u,v) = (a\cos\phi)^{-1}[\partial u/\partial\lambda.\partial v/\partial\phi - \partial v/\partial\lambda.\partial u/\partial\phi]$, ζ is the relative vorticity, f is the Coriolis parameter, $\beta = \partial f/\partial y$ and Φ is the geopotential. For stable or "balanced" jet stream dynamics, the 4 nonlinear tendency terms in $\dot{D}_{nonlinear}$ above sum to zero to a very good approximation [*Moore and Abeling*, 1988] and this is sometimes referred to as the nonlinear balance equation, or NBE for short. In jet exit regions like Figure 31, however, $\dot{D}_{nonlinear}$ can be significantly nonzero, and thus can serve as an identifier of unstable regions were long mesoscale gravity waves may be radiated by unbalanced jet stream dynamics. Indeed, *Koch and O'Handley* [1997] suggested such a calculation as a way to forecast trapped mesoscale gravity waves that can produce locally severe weather. In other words, $\dot{D}_{nonlinear}$ may serve as a large-scale proxy for identifying synoptic regions where smaller-scale gravity waves radiate from the jet.

To investigate this, we use high-resolution global analyses issued by the National Centers for Environmental Prediction (NCEP). *Kalnay et al.* [1996] provide background on the NCEP reanalyses in the context of their specific 40-year reanalysis project. However, those reanalysis products are issued on a 2.5°x2.5° global grid, whereas we need better resolution than this to resolve long wavelength gravity waves, as shown for our analysis of mountain waves in Figure 28 and the accompanying discussion. Thus, we again focus on the 1°x1° analysis product that has been issued since ~1995 in support of the current 1°x1° global numerical weather predictions from the NCEP global spectral model. These products are issued once daily (at 0Z) on 22 pressure levels from sea level (1000 hPa) up to 10 hPa.

We have studied these NCEP products throughout the second CRISTA-SPAS mission (7-16 August, 1997). First, we computed divergences D directly from these pressure-gridded global NCEP datasets. These estimates should be quite reliable since the NCEP global spectral

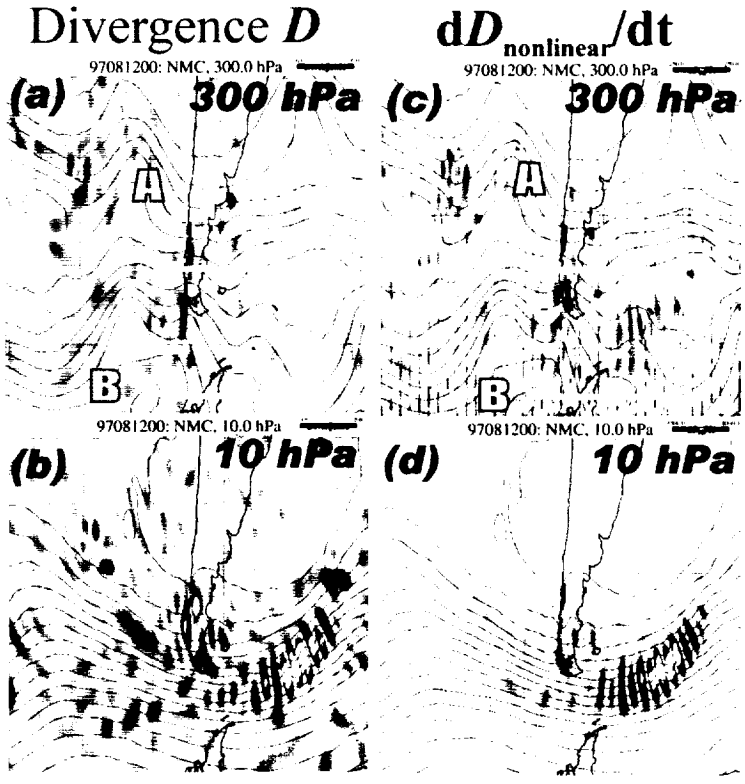

Figure 32: Divergences D (left column) and the nonlinear divergence tendency term, $\dot{D}_{nonlinear}$ evaluated at 300 hPa (top row) and 10 hPa (bottom row) using data from 1°x1° NCEP reanalyses for August 12, 1997 at 0Z. The red-blue color scale is shown top-right, with white showing zero, red most positive and blue the most negative values. Largest divergences are 10^{-6} s^{-1} and $\dot{D}_{nonlinear}$ values are capped at $2.5x10^{-8}$ s^{-2} in panel c and $10x10^{-8}$ s^{-2} in panel (d). Black lines show geopotential height contours. Yellow regions show synoptic settings resembling Figure ZP, which yield apparent propagating gravity wave disturbances.

model is formulated in terms of equations that solve directly for divergence and vorticity. Furthermore, divergences effectively suppress the mean state, and so can often show directly any coherent mesoscale wave disturbances radiated from jets or other regions [e.g., *O'Sullivan and Dunkerton*, 1995]. We also computed the nonlinear divergence tendency term $\dot{D}_{nonlinear}$ using the four terms based on its defining NBE equation above, to search for unstable jet exit regions that may also radiate propagating wave disturbances [e.g., *Koch and O'Handley*, 1997].

Some results for 12 August, 1997 in the western sector of the globe centered near South America are plotted in Figure 32. The top row of plots shows results at 300 hPa, the nominal jet stream altitude at which previous studies have diagnosed the flow [e.g., *Uccellini and Koch*, 1987]. Divergences D are shown in Figure 32a, while the nonlinear divergence tendency $\dot{D}_{nonlinear}$ is shown in Figure 32c: both are contoured using the blue-red color scheme, with blue showing negative anomalies and red positive ones in each case. Black contours show geopotential height contours.

The yellow squares in Figure 32a,c highlight two regions where the synoptic situation shown in Figure 31 appears to have been established, labeled Cases A and B. We see both D and $\dot{D}_{nonlinear}$ anomalies in these regions that take the form of radiating wavelike disturbances. In the "Case A" region, fluctuations in D and $\dot{D}_{nonlinear}$ appear to radiate away from the jet exit region in Figure 31a,c as a somewhat spherical wave disturbance, consistent with gravity wave radiation from a compact three-dimensional region of instability. In the lower "Case B" region, just below the tip of South America, even more coherent wavelike motions are seen, though here the wave fronts appear more planar.

The bottom row of Figure 32 shows corresponding results at the highest stratospheric altitude of 10 hPa (~32 km). In "Case A," we see little evidence for these waves in the stratosphere, due presumably to less favorable wind conditions for this activity to penetrate to higher altitudes. For "Case B," however, we see large amounts of activity of similar horizontal wavelength at 10 hPa related to the activity noted at 300 hPa. Note in particular the strong clustering of geopotential height contours associated with the strong stratospheric winds at the edge of the polar vortex. This is particularly clear in Figure 32d. Interestingly, these strong stratospheric wave trains appear to follow the peak winds of the vortex. This may be due to ducting of these waves into the peak winds of the vortex by strong latitudinal wind shear. For a horizontal wavenumber vector (k,l), the refraction equation for the meridional wavenumber is

$$\frac{dl}{dt} = -k\frac{\partial \overline{U}}{\partial y}$$

which can yield strong focusing into peak winds with strong latitudinal gradients. For example, strong refractive focusing of waves into the peak

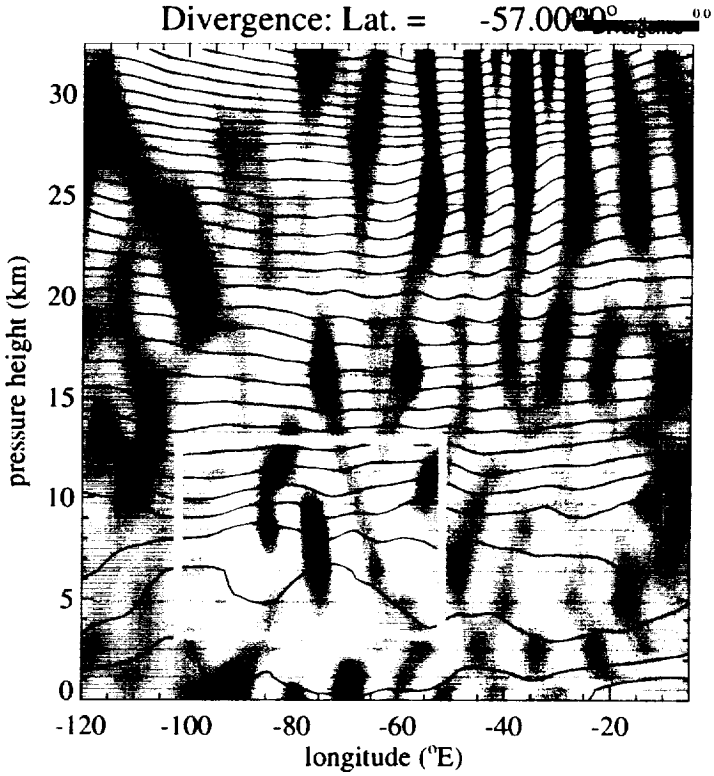

Figure 33: Longitude-height section of divergence D at 57°S for NCEP analyses on 12 August, 1997. Contours show (dry) isentropic levels (logarithmically equispaced). Orange box shows jet exit region with elevated isentropes that descend and spread out downstream. Sloping longitude-height phase contours in D are evident in this region, suggestive of waves produced by this unstable jet region. Note too the intense wave activity of similar horizontal wavelength in the uppermost stratospheric levels, visible in both the divergences and potential temperature contours.

winds of the polar night jet was noted by *Dunkerton* [1984] and *Marks and Eckermann* [1995]. Similar refractive effects nearer the source at jet stream level were noted by *O'Sullivan and Dunkerton* [1995].

To study wave generation in "Case B" in a little more depth, Figure 33 shows a longitude-height section of divergence (blue-red colors) and isentropic surfaces (black contours) at a latitude of 57°S based on the NCEP analyses in Figure 31. Unlike a similar plot at 49°S in Figure 28, this latitude region is well removed from topography of the Andes or the Antarctic Peninsula, and thus waves here cannot be due to mountains. The orange box in Figure 33 shows the region where waves are apparently being generated in Case "B." We see a coherent packet of waves at ~7-12 km and ~90°-60°W, with sloping time-height contours consistent with a wave propagating westward with respect to the background flow. We also see large amplitude waves in the stratosphere above and downstream of this region, though here the phase lines are much deeper due to the intensifying stratospheric flow, which dilates the vertical wavelength of waves aligned along the vortex flow. These waves are evident not just in the colored divergence contours, but also as perturbations on the isentropes in Figure 33.

Nonetheless, the exact correspondence between the low-level activity produced by the jet and the intensifying activity in the stratosphere in Figure 33 is not entirely clear. In particular, unlike with the mountain waves in Figure 28, it is difficult at present to glean clear propagation paths all the way into the stratosphere for this jet-related activity in the NCEP analyses. Analysis of similar maps in NCEP data from other days during the CRISTA 2 missions shows similar ambiguities. We believe this has much to do with the background wind patterns, which may tend to refract waves in and out of the resolved field of view in various cases. In particular, just as for CRISTA data, the vertical wavelength must be sufficiently large that it can be resolved in the final issued data. It may also be that some of the activity at upper levels may be going unstable, due either to wave breaking or due to numerical instabilities, since the mean and wave-induced shears here are large. Indeed, initial computation of Richardson numbers here reveal somewhat low values. We have also analyzed the source regions using other measures of instability or imblance, such as Richardson number and the Lagrangian Rossby number, the latter based on the approximate relation recommended by *Koch and O'Handley* [1997]. These results also show interesting trends but are not shown here in order to keep this report to a manageable length. This work, much of it conducted in the last 3 monthly quarter, will be a focus of ongoing and future research.

2.3.4 Convectively-Generated Stratospheric Gravity Waves

This work has been reported at various stages in previous quarterly reports (e.g., section 1.1. of report dated June 18-September 18, 1998; section 1.2 of report dated 18th. September-18th. December, 1999). Here we briefly report on consolidated research on this topic. Our research here has focused mainly on data acquired during CRISTA2. During this mission period, a large typhoon developed over the South China Sea, reaching Category 5 ("super typhoon") status on 12 August, 1997. Named "Winnie," it was visible both from the GOES geostationary weather satellite and was also photographed by the shuttle astronauts – images of the typhoon from both orbital platforms are shown in Figure 34.

Stratospheric fluctuations were also evident in CRISTA data in this region north of Indonesia, as can be seen in Figures 20 and 30. Typhoons have been implicated previously as sources of large-scale gravity waves [*Matsumoto and Okamura*, 1985; *Sato*, 1993], so it is interesting to investigate whether this enhanced gravity wave activity is due to convection generated within this typhoon region, since, if so, it would comprise an unusually clear connection between a convective source in the tropical troposphere and enhanced gravity wave activity in the tropical stratosphere. Unfortunately, during the mission a special "hawkeye mode" was used to maximize sampling over the Indonesia area in an effort to search for convectively generated wave activity over the maritime continent. This increased sampling came at the expense of coverage of regions to the north where Super Typhoon Winnie formed and passed.

Figure 34: (a) full disk GOES 8 visible image on 12th August, 1997, showing Super Typhoon Winnie. Australia is visible to the south (image courtesy of NOAA's National Climatic Data Center); (b) close-up photo of Winnie taken from *Discovery* on 13th August, 1997 (shuttle robot arm visible in foreground).

Water vapor concentrations were one among many trace constituents measured by CRISTA during the mission, and these measurements extended to quite low levels. Thus, we can study tropical water vapor distributions down to ~13 km, which is well within the tropical troposphere, and correlate it with stratospheric gravity wave activity. Such an analysis is presented in Figure 35, where each panel is divided into 8 subpanels and shows CRISTA limb-scanned data on successive days over the South China Sea area, starting at Day 220 (August 8, 1997) and finishing at Day 227 (August 15, 1997). Note that the most data intensive days are Days 222-226. The passage of Super Typhoon Winnie over these days is shown in the first panel of Figure 35c. Figure 35a shows the evolution of measured gravity wave activity at an altitude of ~35 km for waves with vertical wavelengths in the 14-30 km range, while Figure 35b shows the same thing for waves in the 9-14 km vertical wavelength range. Figure 35c shows measured water vapor mixing ratios at z=13 km as inferred from the CRISTA data, while Figure 35d plots the inferred altitude of cloud tops from these data.

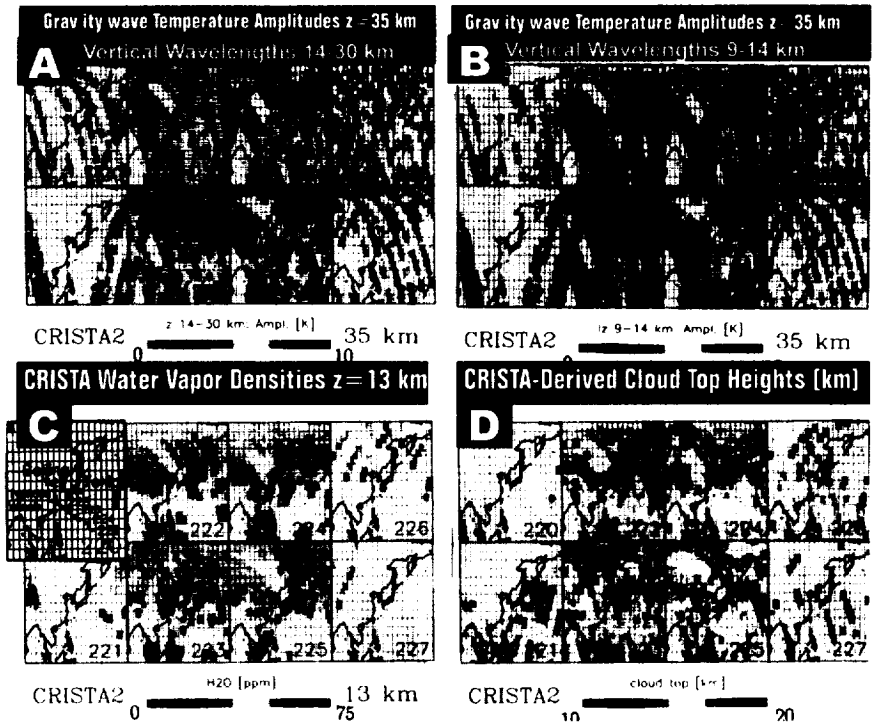

Figure 35: Time sequence of daily CRISTA 2 measurements over China Sea region from Days 220-227 (7-14 August, 1997). **A**: temperature fluctuation amplitudes at z=35 km for λ_z = 14-30 km. **B**: temperature fluctuation amplitudes at z=35 km for λ_z = 9-14 km. **C**: water vapor mixing ratios (ppmv) at z=13 km. Storm track of Super Typhoon Winnie as a function of day number is plotted in the top-left panel. **D**: cloud top heights (in kilometers).

We see what looks to be fairly uniform cloudiness and convection in the area that are

well correlated with increases in the gravity wave variance locally. There does not appear to be any obvious correlation between the daily evolution of the stratospheric gravity wave activity measured by CRISTA (Figure 35a,b) and the passage of the typhoon into the South China Sea region and onto the coast of China. Exact interpretation of the convective activity may be difficult too, since the values are taken at z=13 km and the abrupt change on moving to more poleward latitudes may be due to passage from the subtropical upper troposphere into the dryer mid-latitude lower stratosphere.

A useful way to diagnose the nature of the wave activity, pioneered and explained in previous reports, is to form scatterplots of observed vertical wavelengths versus theoretical hydrostatic vertical wavelengths given by the local background wind speeds, i.e. $\lambda_z=2\pi|c-U|/N$, where c is the ground-based phase speed, U is the background wind along the wave vector direction, and N is the Brunt-Väisälä frequency. Figure 36a plots such a scatterplot of values from the equatorial region in and around the south China sea region, with Figure 36b showing the mean amplitudes of each point binned as a function of its inferred phase speed c from Figure 36a using the formula above (isolines of these inferred c values are also plotted in Figure 36a). We see inferred wave phase speeds peaking at ~20-30 m s^{-1}, although the peak is not sharp and larger values are also evident. Figure 37 shows a detailed profiling of some of this activity in the CRISTA2 data over regions near Japan and Indonesia, using a plot formulation similar to that in Figure 27b. We see lines of activity along orbital tracks that show amplitude and phase coherence over several measurements, such as the sequence labeled 1-4 in Figure 37a. The wavelengths and phase shifts are also reproducible and consistent from profile to profile, as shown in an example in Figure 37c.

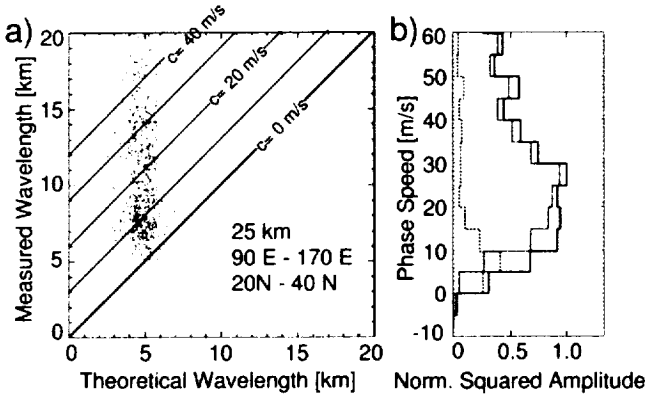

Figure 36: (a) scatterplot of theoretical versus measured vertical wavelengths and (b) amplitude of various points in (a) as a function of their inferred phase speed c. For more information, see *Preusse et al.* [2000d].

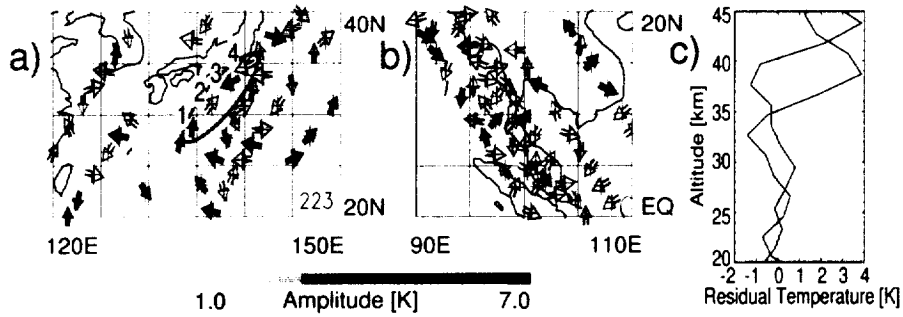

Figure 37: Gravity wave amplitudes and phases (a) east of Japan and (b) north of Indonesia during CRISTA2. Two adjacent profiles from panel (b) are plotted in panel (c), showing the long wavelength gravity wave and a phase shift ~180° between profiles, consistent with a horizontal wavelength ~300-400 km.

More complete versions of this work have now been published [*Eckermann et al.*, 2000*b*; *Preusse et al.*, 2000*d*] and the interested reader should refer to both of those papers for more information. In summary, however, this work has revealed stratospheric gravity waves in the equatorial and subtropical regions of the stratosphere that appear to correlate with increased water vapor abundances in the high tropical troposphere, which we interpret here as a proxy for increased convective activity. Thus, we associate these waves with tropical convective sources. Whether the dominant source is isolated clusters of convection in the region (Figure 35c), or whether the large coherent typhoon system in Figure 34 is the dominant source, is not yet clear and remains an area of ongoing research.

2.3.5 Gravity Waves in the Mesosphere

Here we briefly summarize this subproject work, which has provided information on gravity waves in CRISTA temperatures from high altitude scan (HAS) data. Here temperatures are derived from the 15μm CO_2 channel [e.g., *Riese et al.*, 1999]. Some of this work has already been presented, both here (e.g., the upper level data in Figures 10c and 10d come from the HAS data) and in previous reports (see, e.g., section 1.1. of the report dated September 18-December 18, 1998). Here we summarize one important new finding that has emerged from the analysis so far, namely what we believe to be the first space-based detection of gravity wave interactions with tides, which is one of the more important dynamical processes that occur at these altitudes.

Earlier work with the CRISTA mesospheric temperature data by *Ward et al.* [1999] and *Oberheide et al.* [2000] revealed a large well-defined diurnal tidal signature in these mesospheric temperatures during CRISTA1. It is well-known from ground-based measurements and models that tides can significantly modulate gravity waves, though this has never been observed from space. To investigate this here, we separated the CRISTA1 data into ascending and descending nodes, and performed separate Kalman fits to each. Since the local times of these data are ~12 hours apart, this fit goes some way to also fitting the diurnal tidal structure globally. The top row of Figure 38 shows latitude-height results of our MEM/HA analysis of perturbations in these separated ascending (daytime: ~9am LT) and descending (nighttime: ~9pm) residual temperature fields, in the vertical wavelength range of ~6-9 km, which we can be fairly sure is not contaminated by any remaining tidal perturbations missed by the Kalman detrending.

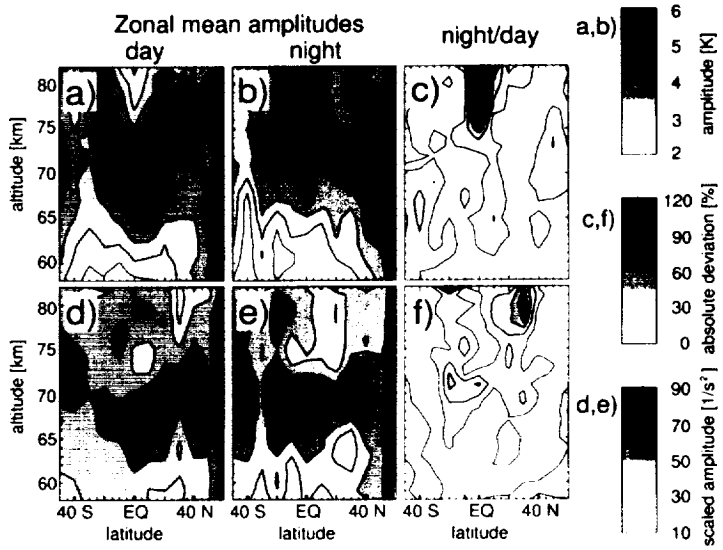

Figure 38: Top row: comparisons of daytime and nighttime zonal mean gravity wave $\hat{T}$ values from the 15μm upper stratospheric and mesospheric temperature profiles obtained by CRISTA during November, 1994. Bottom row shows plots after rescaling of results by $\overline{T}N^2$, with values expressed now as percentages throughout. The day-night differences in (c) largely disappear after this normalization.

There are large differences between the daytime and nighttime data, particularly in the equatorial regions where the diurnal tidal temperature oscillations are large [*Ward et al.*, 1999]. From the Hough mode structures here, we expect the horizontal velocity oscillations to be moderate. Thus, it seemed possible that the temperature perturbations of the tide might be the dominating influence at the equator, modulating the background temperatures and Brunt-Väisälä frequencies seen by the gravity waves and potentially producing these differences in observed gravity wave activity in the CRISTA1 HAS data.

To investigate this, we note from spectral gravity wave models and theories that waves in the wavelength range 6-9 km should lie in the nominal "saturation" regime, since they have scales less than the characteristic wavelength λ_z^*, which is ~15-30 km in the mesosphere [e.g., *Smith et al.*, 1987]. Saturated temperature variance in this range should then satisfy the approximate relation $T'/(\overline{T}N^2) =$ constant, where the constant is determined by the intensity of the saturated m^{-3} portion of the spectrum here [*Smith et al.*, 1987]. Thus, tidal modulations of both N^2 and $\overline{T}$ profiles presented to gravity waves may cause T' amplitudes to vary so as to keep the saturation ratio $T'/(\overline{T}N^2)$ constant. To test this idea, we plot $T'/(\overline{T}N^2)$ in the bottom row of Figure 38 using the Kalman fitted background profiles in each

case. Indeed, we see that this ratio, while not a perfect constant, is much less variable than the temperatures in the top row of Figure 38.

Thus, we believe that Figure 38 provides initial evidence of gravity wave-tidal interactions in the equatorial mesosphere produced by strong diurnal temperature variability due to the diurnal tide. This work, along with additional analysis and discussion, has recently been published by *Preusse et al.* [2000b].

2.4 Gravity Wave Activity in MLS Radiance Data from UARS

Gravity waves have previously been observed in the microwave limb radiances measured by the Microwave Limb Sounder on UARS [e.g., *Wu and Waters*, 1997]. Initial controversy centered on why these zonal-mean MLS variances differed so drastically from similar temperature-related variances derived from other satellite instruments, such as LIMS and GPS/MET. Modeling work by *Alexander* [1998] suggested that the spatial sensitivities of each satellite instrument were the key determinant in setting spatial patterns in their zonal-mean variance maps. In section 2.2 we outlined the results of a detailed study of ours, using our "gravity wave calibrated" subset of CRISTA1 data as a basis, which proved experimentally the modeling hypothesis set forth by *Alexander* [1998]. In particular, we were able to use the vertical sensitivities of both CRISTA and MLS to convert CRISTA temperature data into a zonal-mean distribution that should be more like that which MLS would resolve. When compared to actual MLS variance maps in Figure 10, the comparisons were much improved. The conclusion is that MLS did indeed measure gravity waves reliably during the UARS mission period, but that it measured much longer vertical wavelength gravity waves then did other limb sounders, such as CRISTA, LIMS and GPS/MET.

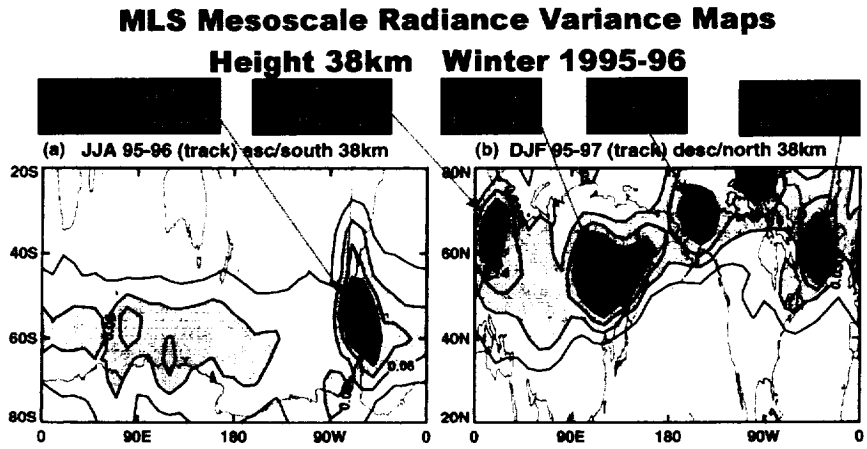

Figure 39: Maps of MLS limb-tracking radiances, averaged during winter months of 1995-1996 [after *McLandress et al.*, 2000]. Geographical locations of evident variance enhancements are pointed out.

Another consequence of this finding, reinforced in a subsequent climatological analysis of MLS data at 38 km by *McLandress et al.* [2000], was that longitudinal variations in MLS radiance variances at a given latitude should not be greatly influenced by instrument observing effects, and thus any zonal asymmetries in MLS radiance variance should be a reliable indicator of gravity wave variability of some sort or another. Figure 39 plots some mean results of MLS variances during winter in the southern and northern middle latitudes, as inferred from limb-track radiances [after *McLandress et al.*, 2000]. These limb track radiances essentially "stared" at a given atmospheric location, yielding spatially distributed data along the orbital track. The radiance measurement in each channel saturated at a certain different altitude, somewhat above the tangent point. These limb track data differ from the conventional limb-scanned data that were acquired exclusively by MLS earlier in the UARS mission. The idea behind the limb track mode was to "save time" by not scanning vertically and just tracking a given limb location. Thus these saturated limb-track radiances could be acquired much more rapidly along track (MLS viewed at a 90° angle to the spacecraft motion), yielding much greater horizontal resolution in the data, and potentially resolving a greater portion of the gravity wave spectrum than before in the limb scan mode. For further information, see *McLandress et al.* [2000] and *Jiang and Wu* [2000].

In Figure 39a we see a large climatological peak in limb track radiances over the southern Andes, which resembles the one seen in CRISTA data (see Figures 14,15,17,20,21,27 and 30). *McLandress et al.* [2000] used a simple analytical model to argue that the peak in Figure 39a was probably due to gravity waves with ground-based phase speeds c clustered near zero, which suggests a mountain-related source.

In collaboration with Drs. Jiang and Wu from JPL, we started looking in depth at daily time series of MLS radiance variances and radiosonde fluctuations from this region of the southern Andes. Figure 40a shows monthly mean values of MLS radiance variance over the southern Andes from limb-tracking data acquired over the period 1995-96. The plot below (Figure 40b) shows results from 6 radiosonde sounding stations scattered around southern South America, from which temperature fluctuations were extracted above 100 hPa using standard analysis techniques [e.g., *Allen and Vincent*, 1995]. We see that there is a clear annual variation in the stratospheric wave activity over the southern Andes, with a large peak in winter and a deep minimum during summer months.

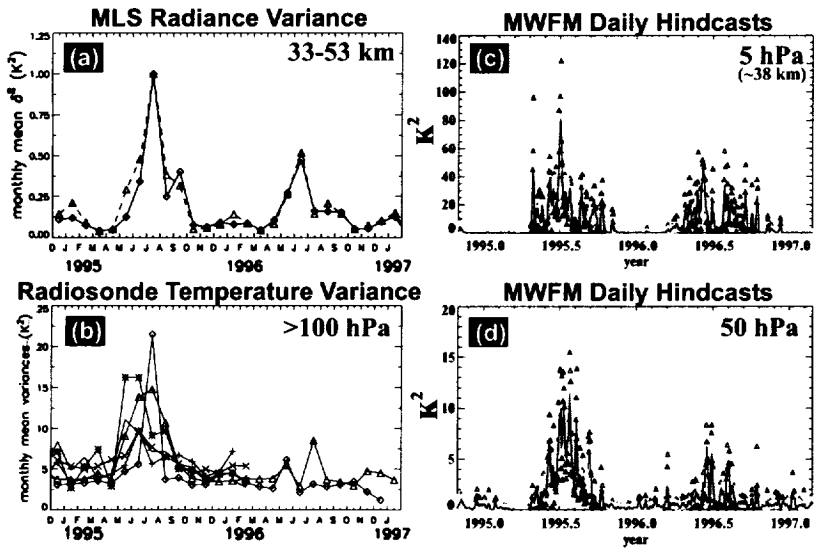

Figure 40: Mesoscale temperature variance in the stratosphere over the southern Andes region from November 1994 to February 1997. Left column shows data: (a) monthly mean MLS radiance variances over the Andes region (60°-80°W, 30°-50°S) at heights ~33-53 km. Note that MLS radiance variances are proportional to, but significantly smaller than, actual temperature variance. Separate curves show data with slightly different horizontal wavelength filter cutoffs; (b) Temperature variances above 100 hPa from six radiosonde stations in the southern Andes region. Right column shows MWFM hindcasts over the southern Andes region (50°-80°W, 40°-46°S) using daily (12Z) DAO assimilated data at (c) 5 hPa and (d) 50hPa. These altitudes roughly coincide to those for the data plots on the left. Triangles show daily means of the MWFM hindcasts, dark curve shows 5 point running average, thick light curve shows 30 point running average.

To see if these results could be explained solely in terms of seasonal variations of stratospheric mountain wave activity from the Andes, we conducted an intensive set of MWFM hindcasts over this southern Andes region using DAO wind and temperature analyses for every day from October 1994 to March 1997, a total of ~800 individual hindcast runs in all. The results were binned and averaged as a function of height. Final daily average results over the same latitude and longitude range are plotted at 5 hPa (Figure 40c) and 50hPa (Figure 40d). These hindcast simulations show remarkable similarities to the MLS and radiosonde data. The seasonal variation is accurately reproduced. Furthermore, the stronger peak in 1995 compared to 1996 is also reproduced. Some of the month-to-month variability also appears to be captured in the simulations, such as the minor "notch" in activity during June-July, 1996. These highly detailed MWFM hindcast simulations appear to prove beyond reasonable doubt that, not only is the climatological peak over the Andes in Figure 39a due to stratospheric mountain waves, but also most of the day-to-day variation in MLS radiances over this region year-round can be explained in terms of mountain waves transmitted into the stratosphere by flow over the southern Andes.

We also note in Figure 39b that some of the other peaks in the Northern Hemisphere, which *McLandress et al.* [2000] had difficulty in associating with a clear source and/or instrument effect, appear to correlate with major mountain ranges. For example, long wavelength stratospheric mountain waves over northern Scandinavia have been observed and modeled in a number of previous studies [e.g., *Dörnback et al.*, 1998]. CRISTA1 data showed enhanced stratospheric temperature amplitudes over

central Eurasia and Alaska, both of which were modeled in an MWFM hindcast simulations (Figures 18 and 19 – see also Figure 4 of *Eckermann and Preusse* [1999]). Intense stratospheric mountain wave fluctuations over southern Greenland were also measured by the MMS on an ER-2 flight on January 6, 1992, a case forecast by MWFM [*Bacmeister et al.*, 1994] and recently simulated in detail using a three-dimensional mesoscale model by *Leutbecher and Volkert* [2000]. Thus, much of the climatological variability in middle-to-high latitude MLS radiance variance in Figure 39b may be due to mountain waves. This idea will be fully assessed and tested in future multiyear MWFM hindcast simulations along the lines set forth in Figure 40c,d. The current MLS work for the Andes is currently being prepared for publication [*Jiang et al.*, 2000].

2.5 Gravity Wave Activity in CLAES Temperatures Measured from UARS

2.5.1 Motivation

To date, gravity waves have been detected in data from only a few instruments on the UARS spacecraft. Of these, data from MLS are the best known and most extensively analyzed to date [*Wu and Waters*, 1997; *Alexander*, 1998; *McLandress et al.*, 2000]. In the mesosphere and lower thermosphere gravity wave signals have been detected in various measurement channels of the HRDI and WINDII instruments [e.g., *Wang et al.*, 2000]. However, stratospheric gravity waves do not appear to have been seen to date from other major stratospheric probing instrument on UARS.

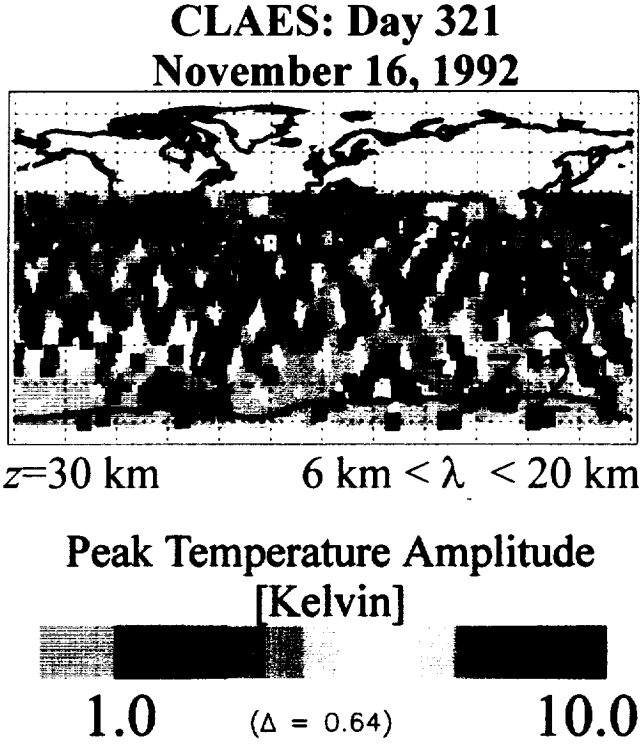

Figure 41: Global maps of gravity wave MEM/HA peak temperature amplitudes from CLAES measurements at 30 km altitude for 2 days starting on Day 321 of 1992 (November 16-17), with results plotted for fluctuations in the vertical wavelength range between 6 and 20 km.

We conducted a detailed pilot to study to apply what we have learned from analysis of CRISTA temperatures for gravity waves, summarized extensively in sections 2.1-2.3 of this report, to see whether there is gravity wave content in stratospheric temperatures measured by the Cryogenic Limb Array Etalon Spectrometer (CLAES) on UARS. We have done this because CLAES is an instrument similar in concept and operation to CRISTA: like CRISTA, CLAES is a cryogenically cooled limb-scanning infrared spectrometer, acquiring spectra within a more limited spectral range of 3.5-12.9 μm. Unlike CRISTA, which acquired full infrared spectra, CLAES used a series of filters on a chopper wheel to isolate lines within specific narrow regions of interest [*Roche et al.*, 1993]. Nonetheless, like CRISTA, CLAES temperatures in the stratosphere and lower thermosphere were inferred from the CO_2 Q-branch limb emissions at ~792 cm^{-1} (12.6 μm).

Gille et al. [1996] provided an extensive validation study of the CLAES temperature product. Comparisons with global analyses and radiosondes showed quite good agreement, with differences of ~2 K. *Gille et al.* [1996] estimated random statistical errors in Version 7 CLAES temperatures to range from ~0.9 K at 100 hPa (~16 km) to ~2.2 K at 0.46 hPa (~53 km). The vertical resolution of the profiles is ~2.5 km, giving a Nyquist vertical wavelength of ~5-6 km. While CRISTA temperatures are a little more accurate than this (estimated typically in the 0.5-1 K range), our analysis revealed stratospheric

gravity wave temperature perturbations as large as 10 K in the CRISTA data (Figure 14). Thus, on the basis of our experience with the CRISTA temperature data and the estimated random errors in CLAES temperatures, there seemed good reason to believe that stratospheric gravity waves may be evident in CLAES temperature data, since the along-limb acquisition characteristics should be broadly comparable. Indeed, stratospheric Kelvin waves have been seen in equatorial CLAES temperatures [*Shiotani et al.*, 1997; *Canziani*, 1999].

2.5.2 Subset of Southward-Viewing CLAES Data: November, 1992

Accordingly, we acquired a subset of the latest version (Version 8) CLAES level 3AT data from the Goddard DAAC. We concentrated first on data from November-December 1992, since this period corresponds best to the November, 1994 period of the first CRISTA-SPAS mission. Since we have a good understanding of the global morphology of gravity wave temperature variance from this mission, it provided a good initial basis from which to analyze and interpret similar potential signals in CLAES temperatures.

In this spirit, we analyzed the CLAES temperature fields in exactly the same way that we analyzed the CRISTA data, fitting the full day's data using a wavenumber 0-6 Kalman filter, subtracting to leave a small-scale temperature residual, then analyzing residual temperature fluctuations using a Maximum Entropy (MEM) to locate wavenumber peaks, and harmonic analysis (HA) to delineate vertical variations in peak wave amplitudes, as set forth for CRISTA in section 2.3.1. MEM/HA estimates at each altitude are stored and global maps for each day and plotted accordingly.

Figure 41 shows temperature perturbation amplitudes $\hat{T}$ at 30 km altitude derived from the primary MEM/HA spectral peak in the CLAES temperature profiles acquired from UARS over a two day sequence starting November 16, 1992. Figure 14 shows a similar pattern of wave amplitude estimates from CRISTA on 6 November, 1994.

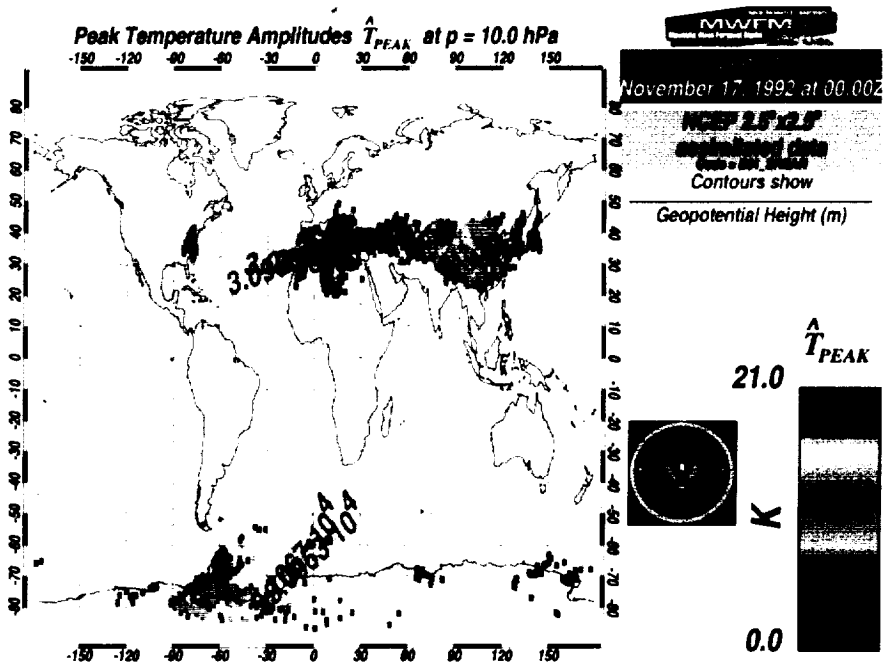

Figure 44: MWFM hindcast within the CLAES view area for southward UARS yaw cycle (~35°N-80°S) on November 17, 1992 at 0UT, at an altitude of 10 hPa (~32 km). Pink contours show geopotential height contours at this pressure altitude. This hindcast was constrained by the NCEP 2.5°x2.5° reanalysis fields for this time and date. Results were filtered to remove horizontal wavelengths > 100 km and vertical wavelengths > 5 km, to mimic the anticipated selectivity of the CLAES temperature data to long wavelength gravity waves.

We note on comparing Figures 14 and 41 that the geographical coverage of each instrument is rather different in each case. This is caused by differences in the viewing geometry of each instrument on the spacecraft. Unlike CRISTA, which was backwards viewing, CLAES viewed the limb at a 90° angle to UARS' orbital motion. Thus, CLAES viewed the atmosphere farther to the north and farther to the south than CRISTA (to latitudes ~80°) in one hemisphere, depending on the yaw cycle, but has much more limited coverage of the opposite hemisphere (only to latitudes ~34°). The sampling characteristics are very much like those of the MLS instrument [see, e.g., *McLandress et al.*, 2000]. We see from

Figure 41 that, on November 16-17, 1992, the UARS yaw cycle was such that CLAES preferentially viewed the Southern Hemisphere.

With these sampling differences in mind, we see qualitative similarities between the CLAES November 16-17, 1992 observations in Figure 41 and the CRISTA observations on November 6, 1994 in Figure 14. First, large regions of the stratosphere over the Southern Ocean have very small $\hat{T}$ values. In equatorial regions, however, typical ambient $\hat{T}$ values are somewhat larger.

More apparent, however, is the large isolated region of enhanced activity located directly above the southern Andes. Extensive analysis outlined in previous reports and publications [*Eckermann and Preusse*, 1999; see sections 7.1 and 7.3] has definitively associated the CRISTA mesoscale temperature enhancement over the southern Andes in Figure 14 as being due to a long mountain wave forced by flow across the Andes (see, e.g., Figures 15,17, 21,27).

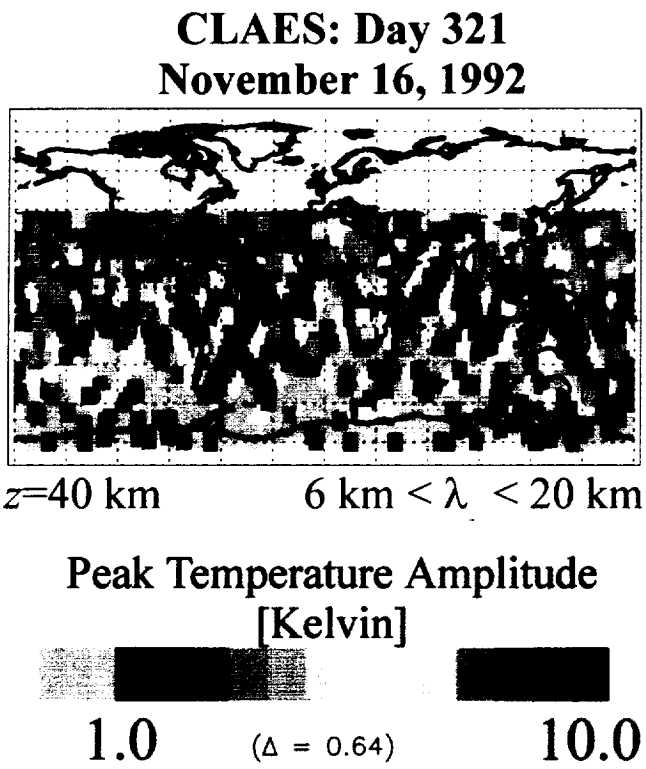

Figure 42: As for Figure 41, but at an altitude of 40 km.

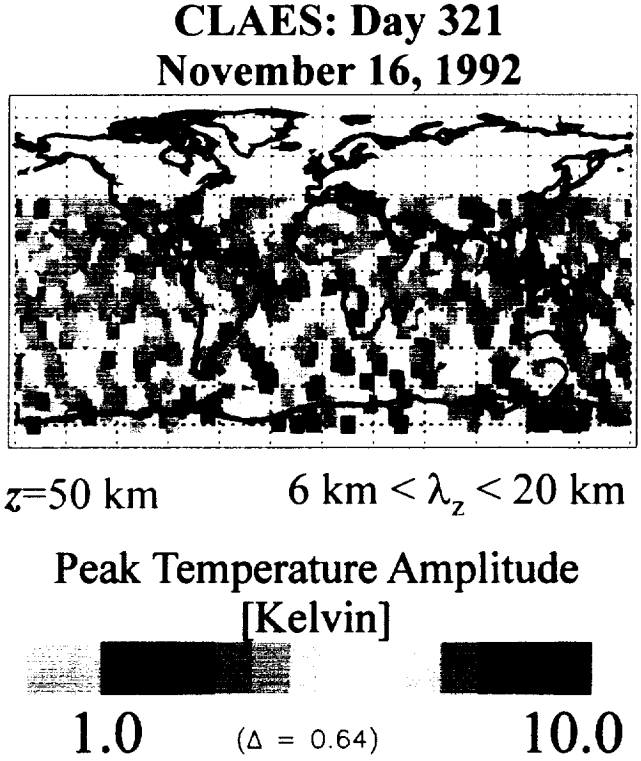

Figure 43: As for Figure 41, but at an altitude of 50 km.

Also apparent in Figure 41, but less apparent in Figure 14, is a large cluster of large $\hat{T}$ values to the north of India. This is interesting since it corresponds to the high mountainous regions of the Himalayas. These regions of enhanced temperature amplitudes stand out from other regions at similar northern latitudes ~30°N, where much reduced $\hat{T}$ values are evident. All of this is strong (but preliminary) evidence that there are the manifestations of long wavelength gravity waves radiated from these mountainous regions, which propagate into stratosphere and produce explicitly resolved temperature perturbations on CLAES temperature profiles.

To assess this, next we investigate the fluctuations in the CLAES data at higher altitudes in the stratosphere. If the fluctuations at 30 km in Figure 41 were due to a chance clustering of temperature errors in some profiles at 30 km, we might expect to see a somewhat different uncorrelated pattern 10 km higher at 40 km. Figure 42 shows the corresponding $\hat{T}$ estimates at 40 km. Figure 43 shows the corresponding $\hat{T}$ estimates at 50 km. The geographical distributions are very similar to those seen in Figure 41, which is inconsistent at least with random errors in CLAES temperatures that are uncorrelated in altitude, and consistent with a geophysical interpretation in terms of gravity wave amplitude trends that persist as waves propagate from 30 km to 40 km and then to 50 km in altitude.

To test whether these might be mountain waves, we conducted MWFM hindcasts for this period, based on recently issued 2.5°x2.5° NCEP global fields from the 40 year reanalysis project [*Kalnay et al.*, 1996]. We also conducted comparison simulations with DAO data for the period, which consisted solely of the coarser 5°x4° analysis fields. The results were basically comparable, though they showed some differences that we ascribe to shortcomings in the coarser and older DAO assimilations, possibly in the troposphere where early DAO analyses were believed to have problems. For present purposes, we use the NCEP analyses as our "best guess" for what the atmosphere was doing at this time.

Figure 44 shows results from MWFM hindcast runs constrained by the NCEP reanalysis fields for 17 November 1992 at 0 UT, a time roughly at the center of the 2 day CLAES observation period November 16-17 (Figure 41). These hindcast simulations predict a concentration of enhanced mountain wave temperature variance in the stratosphere over the extended Himalayan Region, much as observed in Figure 41 and at higher altitudes in Figures 42 and 43. Further, other mountainous regions at a similar latitude, such as the Rocky Mountain Region over the western USA, produces no detectable gravity wave variance, again much as observed in Figures 41-43. The absence of gravity waves here in both model predictions and data is, in some ways, even more persuasive, since it agrees with what we know about mountain wave propagation: i.e., on November 16, 1992, MWFM/NCEP hindcasts suggest that mountain waves could freely propagate into the stratosphere with long wavelengths over the Himalayas, where they could be detected by CLAES. Conversely, mountain waves were either not strongly forced, were blocked from propagating into the stratosphere, or had wavelengths too small to be resolved by CLAES, and so should not have been detected. Thus, detection over the Himalayas and non-detection over the western USA, as simulated and observed, is, in a sense, double confirmation that this activity over the Himalayas in CLAES temperatures is a geophysically believable gravity wave signature.

There are, however, some discrepancies also. For example, the isolated peak over the southern Andes, evident in

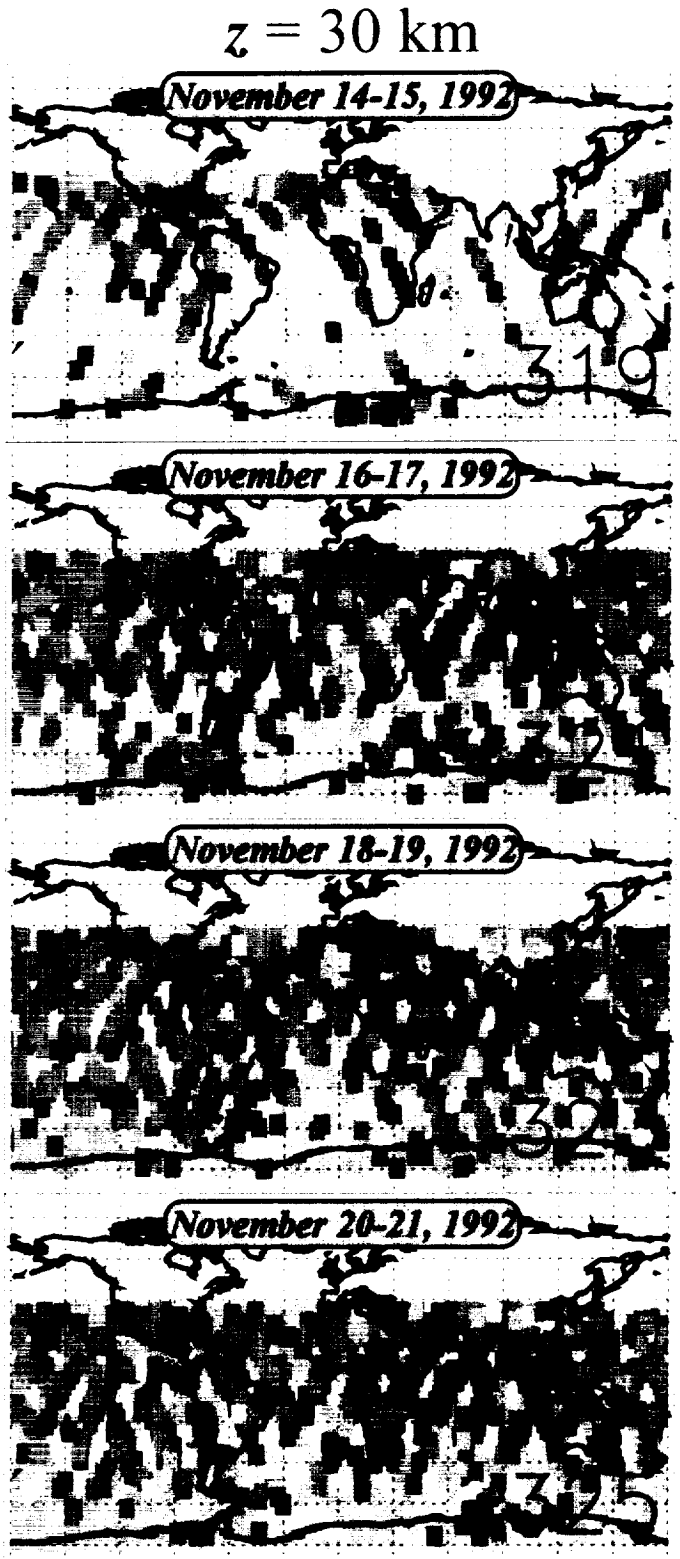

Figure 45: As for Figure 41, but showing a sequence of 2-day maps of CLAES $\hat{T}$ amplitudes at 30 km, from November 14-21, 1992 at an altitude of 30 km.

Figures 41-43, does not show up in the MWFM hindcast in Figure 44. Hindcasts for other times and days, and in which wavelength filtering was not applied to the hindcast output, did reveal an occasional small isolated peak over the southern Andes, but usually of fairly small amplitude (not shown). To study this a bit more, Figure 45 shows results a sequence of CLAES $\hat{T}$ plots at 30 km for the day pairs immediately before and after those shown in Figure 41 (which is reproduced in the second panel from the top in Figure 45). The sampling on the preceding days (top panel) is a little sparse globally, so it is hard to discern trends on the days prior. For the days afterwards (bottom two panels in Figure 45), however, we note that we have better global coverage in the CLAES data. These plots show that the extended region of activity over the Himalayan Region persists and evolves somewhat over the following four days (18-21 November, 1992), giving us further confidence in the fidelity and geophysical reality of this patch of variance in the CLAES temperature data.

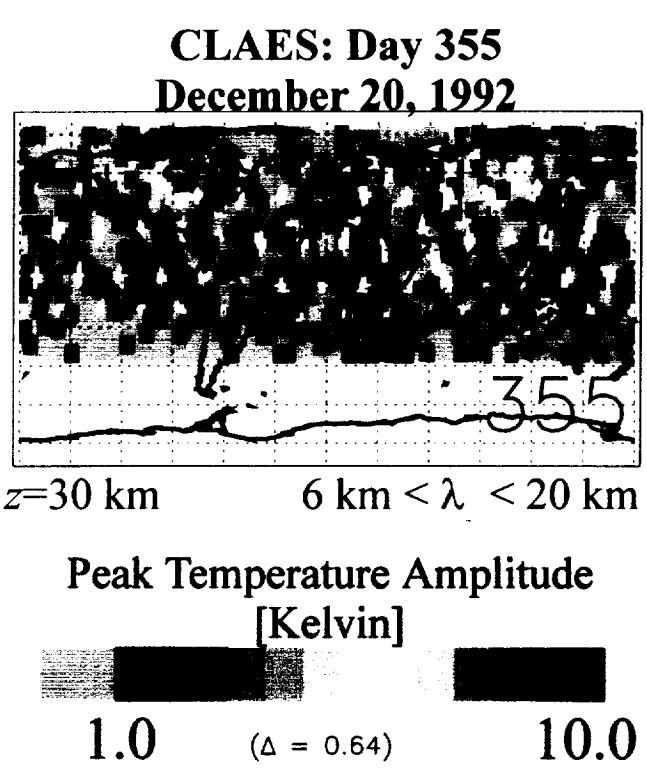

Figure 46: As for Figure 41, but for CLAES data at 30 km starting on Day 355 of 1992 (20-21 December) during the opposite UARS yaw cycle, which led CLAES to preferentially measure the northern hemisphere rather than the south, as evident from the figure.

The "peak" over South America, however, is much more fickle and does not seem to persist as strongly with time in Figure 45. Assuming it is real (i.e. geophysical), there are several plausible reasons for explaining how such waves might arise in the CLAES data but not be simulated by the MWFM hindcasts. One possibility is weaknesses in the assimilated datasets that are being used here. Since these fields are reanalyses based on assimilated data acquired about a decade earlier, they may not accurately simulate fine scale flow features in and around this region of the far southern Andes that may be important for the forcing and propagation of long mountain waves into the stratosphere at the time. Another plausible reason may be that the MWFM algorithms may have weaknesses here. Many processes may be important for forcing mountain waves in this region, but are ignored currently by the simplified analytical parameterization algorithms at the core of the MWFM. One potentially important effect is time dependence of the background wind conditions. MWFM (as with most mountain wave schemes) assumes a time-independent background atmosphere, whereas, in fact, wind conditions tend to vary considerably as a function of time as weather systems move across the topography and evolve. These and other possibilities are a prime focus of planned future investigations of these data.

2.5.3 Subset of Northward-Viewing CLAES Data: December, 1992

Given the promise shown in section 2.5.2 analyzing the southward-veiwing subset of CLAES data from November, 1992, we extended the analysis to some northward viewing CLAES data acquired during December, 1992, by which time UARS had maneuvered to its opposite yaw phase, and thus CLAES was viewing the atmosphere from the other side of the spacecraft's orbital track. This yields measurements which preferentially probe the middle atmosphere in the latitude band from ~35°S to ~80°N, giving a northern hemisphere bias to the data. A global map of CLAES peak residual temperature amplitudes $\hat{T}$ on December 20-21, 1992, inferred from the MEM/HA analysis at an altitude of 30 km are plotted in Figure 46, with results shown for fluctuations with vertical wavelengths in the range ~6-20 km.

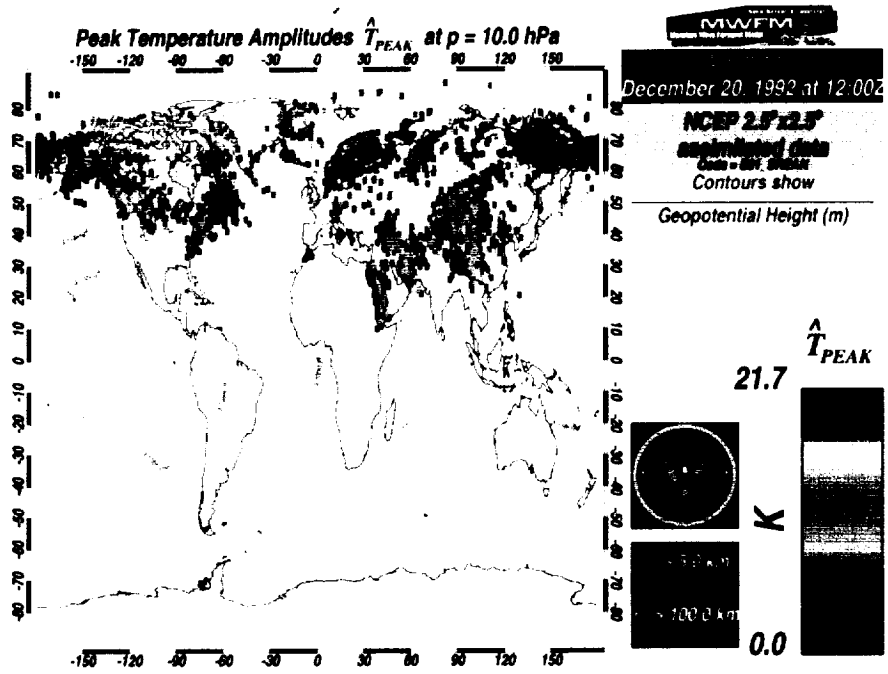

Figure 47: MWFM hindcast within the CLAES view area for northward UARS yaw cycle (~35°S-80°N) on December 20, 1992 at 12UT, at an altitude of 10 hPa (~32 km). Pink contours show geopotential height contours at this pressure altitude. This hindcast was constrained by the NCEP 2.5°x2.5° reanalysis fields for this time and date. Results were filtered to remove horizontal wavelengths > 100 km and vertical wavelengths > 5 km, to mimic the anticipated selectivity of the CLAES temperature data to long wavelength gravity waves.

As for the November data in Figure 41, we see a preferential clustering of the largest temperature amplitudes over the major land masses. In this case, notable regions are the high-latitude regions of North America, southern Greenland, northern Scandinavia, north of India and eastern Eurasia. As is well known, of course, all of these regions are not just major land masses, but have significant mountain ranges situated there. We note similar features in the climatological MLS limb-track radiance variances at 38 km in Figure 39b.

Figure 47 shows an MWFM hindcast simulation at 10 hPa, based on NCEP reanalysis winds and temperatures for December 20, 1992 at 12 UT. Results are filtered to retain only the long wavelength mountain waves that the CLAES limb-scan data should theoretically be sensitive to, based on what we learned from CRISTA limb scans (see Figure 3). The MWFM hindcast in Figure 47 shows remarkable visual similarities to the CLAES peak temperature residuals plotted in Figure 46. In particular, the bands of enhanced variance over far northwestern and far northeastern North America, the southern tip of Greenland, northern Scandinavia and central Eurasia all show out in the MWFM hindcast. Perhaps more impressively, other regions where large mountain ranges exist which could also force mountain waves produce no discernable signal in either the CLAES data in Figure 46 or the MWFM hindcast in Figure 47 – examples include mid-western USA, and the tropical Andes regions along the west coast of South America.

Indeed, previous observational and modeling work has shown the episodic presence of long wavelength mountain waves in several of these middle and high latitude northern stratospheric regions noted above. For example, ground-based and airborne stratospheric observations in northern Scandinavia have frequently revealed long wavelength mountain waves in the lower stratosphere during winter which produce temperature variability that modulates and accentuates the formation of polar stratospheric clouds [*Wirth et al.*, 1999]. As mesoscale model simulations reveal, the long wavelength response is produced by flow over the long wide Norwegian Mountain Range that runs along the coast of Norway [e.g., *Leutbecher and Volkert*, 1996; *Dörnbrack et al.*, 1998; *Wirth et al.*, 1999]. Despite their well-known presence, significant temperature amplitudes and long wavelengths, these waves have heretofore never been detected (explicitly at least) from space-based stratospheric temperature profiling. They could not be seen in CRISTA data since CRISTA could not observe far enough north. Accumulated limb-track variances from MLS at 38 km in Figure 39b suggest some kind of signal in the broad vicinity, but no explicit modeling analysis of these features has been conducted to date. Thus, these apparent observations in Figure 46 may represent the first tentative observation of these long mountain waves from the Norwegian Mountains from UARS. Similarly, stratospheric mountain wave activity emanating from topography on the southernmost tip of Greenland were measured in stratospheric velocity fields at ~70 hPa by the MMS instrument on NASA's instrumented stratospheric

ER-2 research aircraft on 6 January, 1992 [*Chan et al.*, 1993; see also `http://uap-www.nrl.navy.mil/dynamics/html/6jan92.html`]. Mountain wave forecasts [*Bacmeister et al.*, 1994] and hindcast simulations [*Bacmeister et al.*, 1994; *Leutbecher and Volkert*, 2000] definitively associated this activity with mountain waves and helped delineate the nature of the waves. In particular, the three-dimensional mesoscale model simulations of *Leutbecher and Volkert* [2000] revealed a great deal of structure in the simulated waves, showing both shorter and longer wavelength structures, the latter potentially resolvable from a satellite. Again, however, it does not appear that such waves have heretofore been detected from a satellite platform.

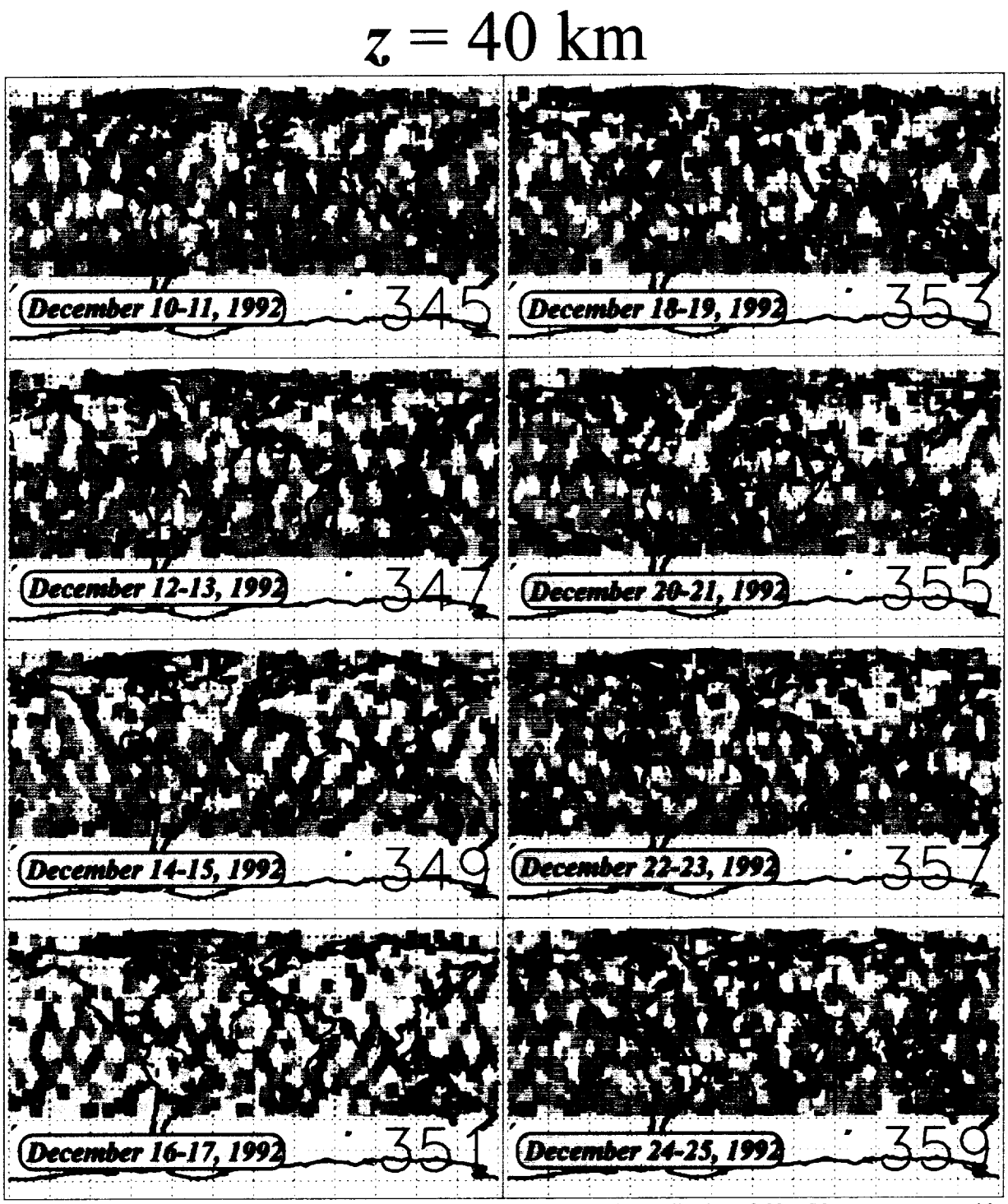

Figure 48: Sequence of global maps on successive day pairs of the peak amplitudes of CLAES temperature residuals, $\hat{T}$, at an altitude of 40 km.

Waves have been detected from space before over central Eurasia, however. Detections of such waves in CRISTA data in November, 1994, were reported in previous quarterly reports and published in the literature [*Eckermann and Preusse*, 1999; see sections 7.1 and 7.3]. These waves appeared to be radiated from complex tropographic ridges along the border regions of China, Russia, Mongolia and Kazakhstan, although exact spatial correlations with associated MWFM hindcast simulations were not perfect. Again, the band of enhanced activity over central and eastern Eurasia in the CLAES $\hat{T}$ plot in Figure 46 has many similarities to similar activity evident in the corresponding MWFM/NCEP hindcast map in Figure 47.

Figure 48 shows the global picture at a higher altitude of 40 km over a complete 16 day period of CLAES measurements in December, 1992 (Days 345-360). We see that activity over Northern America and Europe seems to be most intense during Days 353-358 (18-23 December), whereas in the eight days preceding (Days 345-353; December 10-17), the activity over North America largely disappears, while the activity over Europe, while it persists more, tends to be a little more dispersed. To assess this from the mountain wave perspective, Figure 49 shows sample MWFM/NCEP hindcasts at 10hPa for 12 December, 1992 (left panel) and 23 December, 1992 (right panel). Like the results in Figure 48, we see strong diminution of hindcast mountain wave amplitudes over North America earlier in December, with much of the continent free of forecast wave activity (Figure 49, left panel). Conversely, 10 days later (Figure 49, right panel), a great deal more of the North American has areas where stratospheric mountain waves are forecast. Hindcast differences over Europe are not as clear, however. The differences are also less distinct in the CLAES data in Figure 48, but there are indications of stronger activity later in December than earlier. This does not come out in the hindcasts in Figure 49, at least not obviously.

We believe that that this work has provided strong evidence of stratospheric mountain wave activity in the 12.6 μm temperatures measured by CLAES, which is an entirely new finding that was motivated by our analysis of a similar instrument (CRISTA) earlier in the project (sections 2.1-2.3). Thus, this adds another UARS instrument to the growing list that now appear to explicitly resolve gravity wave perturbations in one of their middle atmosphere channels. Our goal is to analyze these data further to provide information of a similar kind to CRISTA over the time periods and regions probed by CLAES before it exhausted its supply of onboard cryogen (~May, 1993). While this set of data is limited by UARS standards, it is much more extensive than the ~2 weeks of data provided by CRISTA, and the latter has kept us busy for many months of this contract. Thus, we believe there is much more to be done and found in this newly discovered CLAES gravity wave product.

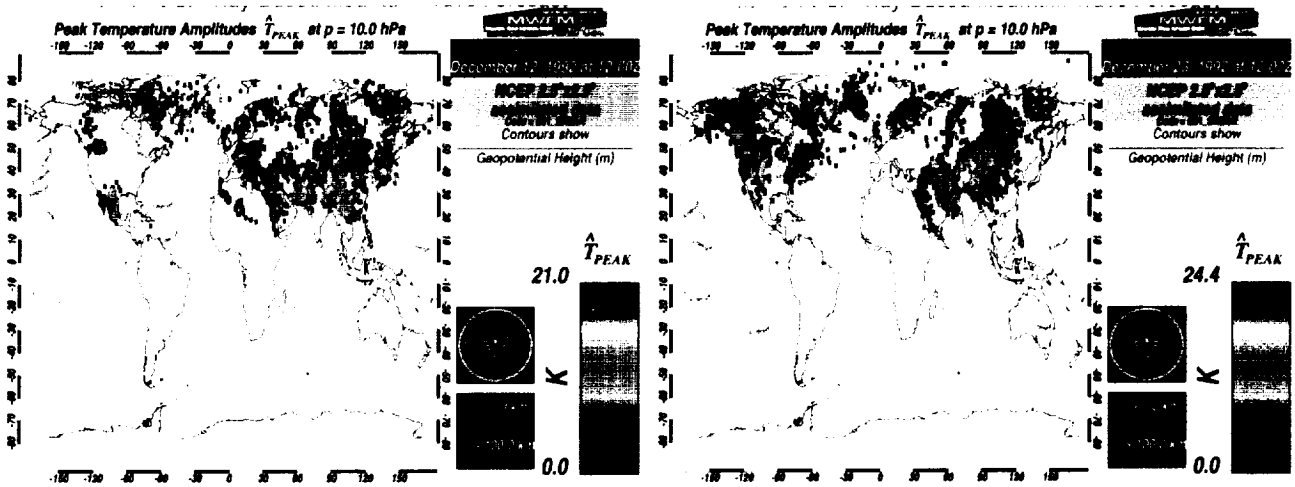

Figure 49: MWFM hindcasts constrained by NCEP reanalysis fields on December 12 (Day 347 - left panel) and December 23 (right panel: Day 358), at a height of 10 hPa and local time of 12 UT, with vertical wavelengths > 5 km and horizontal wavelengths > 100 km removed from the synthesized results.

3. Summary

3.1 Conclusions and Recommendations

Our work has proven that the era of routine space-based detection of gravity wave fluctuations in the stratosphere and mesosphere is at hand, a claim that was controversial and in doubt at the beginning of this project. Our work has provided insights into the precise way in which infrared limb scanning satellites explicitly detect long wavelength gravity waves in their profiled radiance data. These insights (e.g., section 2.1) will aid in the design of similarly motivated future instruments (e.g., HIRDLS) that can detect gravity waves by limb scanning, or via other observing strategies (e.g., nadir imaging).

We have conducted an extensive in-depth analysis of gravity waves resolved in the CRISTA limb-scanned temperature data (section 2.3), and have demonstrated that they provide extremely valuable global and precise geographical and vertical information on long wavelength gravity wave activity produced by a variety of sources, such as mountains, the jet stream, and tropical convection, as well as how these waves interact with tidal motions at higher altitudes. These insights have motivated further searches for such wave sources and characteristics in the MLS and CLAES temperature data acquired on UARS (sections 2.4 and 2.5).

Follow-up work is now needed to consolidate upon these findings. For example, we have shown that MLS and CLAES data resolve long wavelength gravity waves quite well, yet this rich vein of scientific information on stratospheric gravity waves has barely been tapped to date. Detailed analysis of these data, rather than the limited climatological analyses [*McLandress et al.*, 2000] or subset/subregion studies (sections 2.4 and 2.5) that have been attempted to date, is the logical next step forward. It is important that this is done, since our observational record on gravity waves in the middle atmosphere is still meager, yet these waves are known to be vital in setting the global circulation and climate.

3.2 Relation to Ultimate Objectives of the Research Contract

At the beginning of this contract, the very detection of middle atmospheric gravity waves explicitly from satellite platforms was still uncertain and controversial. Accumulated preliminary radiance/temperature variances from instruments such as LIMS and MLS clashed (see Figure 10), and, since these fluctuations were at the very detection limits (both in terms of accuracy/precision and spatial resolution), errors or contamination from larger scale structures (e.g., vortex filaments) could not be discounted. Detection of gravity waves from other instruments, such as infrared limb scanners such as CRISTA and CLAES, had yet to be studied and verified.

Thus, our goal in this research project was to cast light on space-based detection of gravity waves in the middle atmosphere, test these inferences using CRISTA data, and apply our knowledge to detecting and characterizing gravity waves that might be explicitly resolved in data from various other instruments on UARS. We made large strides in all of these goals during this project, as has been outlined in section 2.

Section 2.1 outlines the significant progress we made in understanding how infrared limb scanners measure gravity waves in the middle atmosphere. Section 2.2 illustrates why earlier zonal-mean data were somewhat discrepant and formulates methods for getting around this. Section 2.3 outlines a detailed analysis technique we developed to characterize long wavelength gravity waves in CRISTA data, which yielded new global information of stratospheric gravity waves generated by mountains (section 2.3.2), the vortex/jet-stream system (section 2.3.3), tropical convection (section 2.3.4) and the extension of these waves into the mesosphere where they interact with the diurnal tide (section 2.3.5). The detailed insights gained here were used to study climatological distributions of mountain waves evident in MLS data from UARS (section 2.4), and to prove for the first time that

stratospheric temperatures measured by the CLAES instrument on UARS also resolved stratospheric gravity waves (section 2.5). We believe that the full body of work summarized in this final report, and the ensuing publications listed in sections 4 and 5, have amply fulfilled all the research goals we set ourselves at the beginning of the project.

4. Papers Published in Peer-Reviewed Literature From Work Performed Under This Contract[2]

Drob, D. P., J. M. Picone, S. D. Eckermann, C. Y. She, J. F. Kafkalidis, D. A. Ortland, R. J. Niciejewski, and T. L. Killeen, Mid-latitude temperatures at 87 km: results from multi-instrument Fourier analysis, *Geophys. Res. Lett., 27*, 2109-2112, 2000.

Eckermann, S. D. and P. Preusse, Global measurements of stratospheric mountain waves from space, *Science, 286*, 1534-1537, 1999.

Eckermann, S. D., P. Preusse, and D. Offermann, Stratospheric gravity waves near the edge of the Southern Hemisphere polar vortex during the CRISTA2 mission, J. Geophys. Res., (manuscript in preparation for CRISTA2 special issue), 2000a.

Eidmann, G., D. Offermann, M. Jarisch, P. Preusse, S. D. Eckermann, and F. J. Schmidlin, Horizontal temperature variability in the stratosphere: global variations inferred from CRISTA data, *Adv. Space Res.*, (in press), 2000.

Jiang, J., D. L. Wu and S. D. Eckermann, A study of mountain waves over the Andes: UARS MLS observations compared with MWFM numerical simulations, *J. Geophys. Res.*, (paper in preparation), 2000.

Preusse, P., B. Schaeler, J. T. Bacmeister and D. Offermann, Evidence for gravity waves in CRISTA temperatures, *Adv. Space Res., 24*, (11)1601-(11)1604, 1999.

Preusse, P., S. D. Eckermann and D. Offermann, Comparison of global distributions of zonal-mean gravity wave variance inferred from different satellite instruments, *Geophys. Res. Lett., 27*, 3877-3880, 2000a.

Preusse, P., S. D. Eckermann, J. Oberheide, M. E. Hagan and D. Offermann, Modulation of gravity waves by tides as seen in CRISTA temperatures, *Adv. Space Res.*, (submitted), 2000b.

Preusse, P., S. D. Eckermann, A. Dörnbrack, M. Riese, B. Schaeler, D. Broutman, J. T. Bacmeister and D. Offermann, Space based measurements of stratospheric mountain waves by the Cryogenic Infrared Spectrometers and Telescopes for the Atmosphere (CRISTA), *J. Geophys. Res.*, (paper in preparation for CRISTA 2 special issue), 2000c.

Preusse, P., G. Eidmann, S. D. Eckermann, B. Schaeler, R. Spang, and D. Offermann, Indications of convectively generated gravity waves in CRISTA temperatures, *Adv. Space Res.*, (in press), 2000*d*.

Stevens, M. H., S. D. Eckermann, R. R. Conway, and R. G. Roble, MAHRSI observations of lower thermospheric nitric oxide: The role of gravity waves, *Geophys. Res. Lett.* (paper in preparation), 2000.

Tan, K. A., and S. D. Eckermann, Numerical model simulations of mountain waves in the middle atmosphere over the southern Andes, in *Atmospheric Science Across the Stratopause*, AGU Geophysical Monograph Series, D. E. Siskind, S. D. Eckermann and M. E. Summers editors, *123*, 311-318, 2000.

5. Additional Publications From Work Performed Under This Contract

Britt, R. R., Satellite spots turbulence-producing mountain waves in the stratosphere, *space.com*, http://www.space.com/scienceastronomy/planetearth/mountain_waves_991118.html, 1999.

[2] Full listing of most of these papers, with hyperlinks to abstracts and electronic manuscripts, is available at the following web site: `http://uap-www.nrl.navy.mil/dynamics/html/puball.html`

Eckermann, S. D., D. Broutman, K. A. Tan, P. Preusse and J. T. Bacmeister, Mountain waves in the stratosphere, *NRL Review*, 73-86, 2000a.

Eckermann, S. D., P. Preusse, B. Schaeler, J. Oberheide, D. Offerman, J. T. Bacmeister and D. Broutman, Global gravity wave "weather" in the middle atmosphere: preliminary insights from the CRISTA-SPAS missions, Proceedings of the Solar Terrestrial and Space Physics Community, 13th. National Congress of the Australian Institute of Physics, ANARE Research Reports, Australian Antarctic Division, Kingston, Tasmania, R. J. Morris and P. J. Wilkinson eds., (in press), 2000b[3].

Preusse, P., B. Schaeler, D. Offermann and S. D. Eckermann, Mountain lee waves over South America - a case study on the sensitivity to short spatial scales, in *Mesoscale processes in the stratosphere*, European Communities Air Pollution Research Report, No. 69, K. S. Carslaw and G. T. Amanatidis eds., 217-222, 1999.

6. Additional References for this Report

Alexander, M. J., Interpretations of observed climatological patterns in stratospheric gravity wave variance, *J. Geophys. Res., 103*, 8627-8640, 1998.

Allen, S. J., and R. A. Vincent, Gravity-wave activity in the lower atmosphere - seasonal and latitudinal variations, *J. Geophys. Res., 100*, 1327-1350, 1995.

Bacmeister, J. T., Mountain-wave drag in the stratosphere and mesosphere inferred from observed winds and a simple mountain-wave parameterization scheme, *J. Atmos. Sci., 50*, 377-399, 1993.

Bacmeister, J. T., P. A. Newman, B. L. Gary, and K. R. Chan, An algorithm for forecasting mountain wave-related turbulence in the stratosphere, *Wea. Forecasting, 9*, 241-253, 1994.

Broutman, D., J. W. Rottman and S. D. Eckermann, A hybrid method for analyzing wave propagation from a localized source, with application to mountain waves, *Q. J. R. Meteorol. Soc.*, (in press), 2000.

Canziani, P., Slow and ultraslow equatorial Kelvin waves: the UARS-CLAES view, *Q. J. R. Meteorol. Soc., 125*, 657-676, 1999.

Chan, K. R., and coauthors, A case study of the mountain lee wave event of January 6, 1992, *Geophys. Res. Lett., 20*, 2551–2554, 1993.

Coy, L., and R. Swinbank, The characteristics of stratospheric winds and temperatures produced by data assimilation, *J. Geophys. Res.*, 102, 25,763-25,781, 1997.

Dörnbrack, A., M. Leutbecher, H. Volkert, and M. Wirth, Mesoscale forecasts of stratospheric mountain waves, *Meteor. Appl., 5*, 117–126, 1998.

Duck, T. J., and J. A. Whiteway, Seasonal transition in gravity wave activity during the springtime stratospheric vortex breakdown, *Geophys. Res. Lett., 27*, 3477-3480, 2000.

Dunkerton, T. J., Inertia–gravity waves in the stratosphere, *J. Atmos. Sci., 41*, 3396–3404, 1984.

Eckermann, S. D., I. Hirota, and W. K. Hocking, Gravity-wave and equatorial-wave morphology of the stratosphere derived from long-term rocket soundings, *Quart. J. Roy. Meteor. Soc., 121*, 149-186, 1995.

Eckermann, S. D., D. Broutman, and J. T. Bacmeister, Aircraft encounters with mountain wave-induced clear air turbulence: Hindcasts and operational forecasts using an improved global model, *Preprint Volume of the Ninth Conference on Aviation, Range and Aerospace Meteorology*, American Meteorological Society, pp456-459, 2000c.

Fetzer, E. J., and J. C. Gille, Gravity wave variance in LIMS temperatures. Part I: variability and comparison with background winds, *J. Atmos. Sci., 51*, 2461-2483, 1994.

Gille, J. C., Bailey, P. L., Massie, S. T., Lyjak, L. V., Edwards, D. P., Roche, A. E., Kumer, J. B., Mergenthaler, J. L., Gross, M. R., Hauchecorne, A., Keckhut, P., McGee, T. J., McDermid, I. S., Miller, A. J., and Singh, U., Accuracy and precision of the Cryogenic Limb Array Spectrometer (CLAES) temperature retrievals , *J. Geophys. Res., 101*, 9583-9601, 1996.

[3] This paper is available online at `http://www.ips.gov.au/SRAMP/aip/steve/steve.htm`

Guest, F. M., M. J. Reeder, C. J. Marks, and D. J. Karoly, Inertia–gravity waves observed in the lower stratosphere over Macquarie Island, *J. Atmos. Sci., 57*, 737–752, 2000.

Hogan, T. F., and T. E. Rosmond, The description of the Navy operational global atmospheric prediction system, *Mon. Wea. Rev., 119*, 1786-1815, 1991.

Jiang, J. H., and D. L. Wu, UARS MLS observations of gravity waves associated with the arctic winter stratospheric vortex, *Geophys. Res. Lett.*, (in press), 2000.

Kalnay, E., and coauthors, The NCEP/NCAR 40 year reanalysis project, *Bull. Amer. Meteor. Soc., 77*, 437-471, 1996.

Koch, S. E., and C O'Handley, Operational forecasting and detection of mesoscale gravity waves, *Wea. Forecasting, 12*, 253-281, 1997.

Knox, J. A., Generalized nonlinear balance criteria and inertial instability, *J. Atmos. Sci., 54*, 967-985, 1997.

Leutbecher, M., and H. Volkert, Stratospheric temperature anomalies and mountain waves: A three-dimensional simulation using a multi-scale weather prediction model, *Geophys. Res. Lett., 23*, 3329-3332, 1996.

Leutbecher, M. and H. Volkert, The propagation of mountain waves into the stratosphere: quantitative evaluation of three-dimensional simulations, *J. Atmos. Sci., 57*, 3090–3108, 2000.

Marks, C. J., and S. D. Eckermann, A three-dimensional nonhydrostatic ray-tracing model for gravity waves: Formulation and preliminary results for the middle atmosphere, *J. Atmos. Sci., 52*, 1959-1984, 1995.

Marshall, B., T. L. Gordley, and D. A. Chu, BANDPAK: Algorithms for modeling broadband transmissions and radiance, *J. Quant. Spectrosc. Radiat. Transfer, 52*, 563-599, 1994.

Matsumoto, S., and H. Okamura, The internal gravity wave observed in the Typhoon T8124 (Gay), *J. Meteorol. Soc. Japan, 63*, 37-51, 1985.

McLandress, C., M. J. Alexander, and D. L. Wu, Microwave limb sounder observations of gravity waves in the stratosphere: a climatology and interpretation, *J. Geophys. Res., 105*, 11,947-11,967, 2000.

Moore, J. T., and W. A. Abeling, A diagnosis of unbalanced flow in upper levels during the AVE-SESAME-I period, *Mon. Wea. Rev., 116*, 2425-2436, 1988.

Oberheide, J., M. E. Hagan, W. E. Ward, M. Riese, and D. Offermann, Modeling the diurnal tide for the Cryogenic Infrared Spectrometers and Telescopes for the Atmosphere (CRISTA) 1 time period, *J. Geophys. Res.*, (in press), 2000.

O'Sullivan, D., and T. J. Dunkerton, Generation of inertia-gravity waves in a simulated life cycle of baroclinic instability. *J. Atmos. Sci., 52*, 3695–3716, 1995.

Riese, M., R. Spang, P. Preusse, M. Ern, M. Jarisch, D. Offermann, and K. U. Grossmann, Cryogenic Infrared Spectrometers and Telescopes for the Atmosphere (CRISTA) data processing and atmospheric temperature and trace gas retrieval, *J. Geophys. Res., 104*, 16-349-16,367, 1999.

Roche, A. E., Kumer, J. B., Mergenthaler, J. L., Ely, G. A., Uplinger, W. G., Potter, J. F., James, T. C., and Sterritt, L. W., The Cryogenic Limb Array Etalon Spectrometer (CLAES) on UARS: experiment description and performance, *J. Geophys. Res., 98*, 10763-10775, 1993.

Rodgers, C. D., Statistical principles of inversion theory, in *Inversion Methods in Atmospheric Remote Sounding*, A. Deepak ed., Academic Press, New York, 1977.

Sato, K., Small-scale wind disturbances observed by the MU radar during the passage of Typhoon Kelly, *J. Atmos. Sci., 50*, 518-537, 1993.

Seluchi, M., Y. V. Serafini, and H. Le Treut, The impact of the Andes on transient atmospheric systems: a comparison between observations and GCM results, *Mon. Wea. Rev., 126*, 895–912, 1998.

Shiotani, M., J. C. Gille and A. E. Roche, Kelvin waves in the equatorial lower stratosphere as revealed by cryogenic limb array etalon spectrometer temperature data, *J. Geophys. Res., 102*, 26,131-26,140, 1997.

Smith, S. A., D. C. Fritts, and T. E. Van Zandt, Evidence for a saturated spectrum of atmospheric gravity waves, *J. Atmos. Sci., 44*, 1404-1410, 1987.

Tsuda, T., M. Nishida, C. Rocken, and R. H. Ware, A global morphology of gravity wave activity in the stratosphere revealed by the GPS occultation data (GPS/MET), *J. Geophys. Res., 105*, 7257-7273, 2000.

Uccellini, L. W., and S. E. Koch, The synoptic setting and possible energy sources for mesoscale wave disturbances. *Mon. Wea. Rev., 115*, 721–729, 1987.

Ward, W. E., J. Oberheide, M. Riese, P. Preusse, and D. Offermann, Tidal signatures in temperature data from CRISTA 1 mission, *J. Geophys. Res., 104*, 16,391-16,403, 1999.

Vadas, S. L., and D. C. Fritts, Gravity wave re-radiation and mean responses to local body forces in the atmosphere, II, 3D mean responses, *J. Atmos. Sci.*, (submitted), 2001.

Wang, D. Y., W. E. Ward, B. H. Solheim, and G. G. Shepherd, Wavenumber spectra of horizontal wind and temperature measured with WINDII, Part I: observational results, *J. Atmos. Sol.-Terr. Phys., 62*, 967-979, 2000.

Whiteway, J. A., Enhanced and inhibited gravity wave spectra, *J. Atmos. Sci., 56*, 1344-1352, 1999.

Whiteway, J. A., and T. J. Duck, Enhanced Arctic stratospheric gravity wave activity above a tropospheric jet, *Geophys. Res. Lett., 26*, 2453-2456, 1999.

Whiteway, J. A., T. J. Duck, D. P. Donovan, J. C. Bird, S. R. Pal, and A. I. Carswell, Measurements of gravity wave activity within and around the Arctic stratospheric vortex, *Geophys. Res. Lett., 24*, 1387-1390, 1997.

Wirth, M., A. Tsias, A. Dörnbrack, V. Weiss, K. S. Carslaw, M. Leutbecher, W. Renger, H. Volkert, and T. Peter, Model-guided Lagrangian observation and simulation of mountain polar stratospheric clouds, *J. Geophys. Res., 104*, 23,971-23,981, 1999.

Wu, D. L., and J. W. Waters, Observations of gravity waves with the UARS Microwave Limb Sounder, in *Gravity Wave Processes: Their Parameterization in Global Models*, NATO ASI Series, Vol. I 50, K. Hamilton ed., Springer-Verlag, Heidelberg, 103-120, 1997.

7. Appendix: Three Short Sample Publications Reporting Results from this Contract

7.1 Eckermann, S. D., and P. Preusse, **Science, 286,** ***1534-1537,*** *1999* ***(4 pages)***

7.2 Preusse, P., S. D. Eckermann and D. Offermann, **Geophys. Res. Lett., 27,** ***3877-3880, 2000. (4 pages)***

7.3 Britt, R. R., feature article in **space.com,** ***November 18, 1999. (3 pages)***

Global Measurements of Stratospheric Mountain Waves from Space

Stephen D. Eckermann[1] and Peter Preusse[2]

Temperatures acquired by the Cryogenic Infrared Spectrometers and Telescopes for the Atmosphere (CRISTA) during shuttle mission STS-66 have provided measurements of stratospheric mountain waves from space. Large-amplitude, long-wavelength mountain waves at heights of 15 to 30 kilometers above the southern Andes Mountains were observed and characterized, with vigorous wave breaking inferred above 30 kilometers. Mountain waves also occurred throughout the stratosphere (15 to 45 kilometers) over a broad mountainous region of central Eurasia. The global distribution of mountain wave activity accords well with predictions from a mountain wave model. The findings demonstrate that satellites can provide the global data needed to improve mountain wave parameterizations and hence global climate and forecast models.

Gravity waves in the lower atmosphere, forced by flow over mountains, have been observed and modeled for many years (*1*). Mountain waves can also propagate into the stratosphere. Drag produced by breaking stratospheric mountain waves is essential for accurate climate and forecast models (*2*). The turbulence generated by stratospheric mountain wave breaking poses a major safety hazard to high-altitude aircraft (*3–5*) and influences stratosphere-troposphere exchange of important trace gases (*6*). Mountain wave ascent triggers formation of polar stratospheric clouds (PSCs) (*7*). It has been argued that mountain wave PSCs reduce Arctic ozone concentrations by activating chlorine in stratospheric air that flows through them (*8*).

Computational limits have prevented global troposphere-stratosphere models from operating at a spatial resolution fine enough to generate mountain waves in the stratosphere, so their effects must be parameterized (*2*). The spatial resolution of stratospheric sounding satellites has generally been too coarse to resolve mountain waves. Detailed measurements have been limited largely to scattered ground-based soundings (*9*), some regional campaigns (*3*, *10*), and chance intercepts by high-altitude aircraft (*4*, *11*). Thus, global data are lacking.

Recently, a few high-resolution stratospheric satellite instruments have detected gravity waves (*12*). However, instrumental effects have complicated interpretation of these gravity-wave signals (*13*). In particular, the data have shown little clear evidence of mountain waves, despite suggestions that mountains should be a strong source of stratospheric gravity waves (*2–4*, *9–11*).

On 4 November 1994, the CRISTA-SPAS (Shuttle Pallet Satellite) experiment was deployed into orbit by the space shuttle Atlantis (Fig. 1A). CRISTA measured infrared emission spectra (4 to 71 μm) from atmospheric limb scans with the use of three telescopes that viewed closely separated volumes of air (*14*). From the CO_2 Q-branch emission at ~12.6 μm, vertical temperature profiles $T(z)$ with a precision of ~0.5 K were derived every 1.5 km in altitude, z, throughout the stratosphere (*15*, *16*). Although short spatial scales along the line of sight are smeared out, medium scale structure is resolved. Theoretical radiance calculations show that the temperature data have >50% visibility to gravity waves with wavelengths ≥3 to 5 km vertically and ≥100 to 200 km along the limb (*17*). Each telescope provided a profile every 200 or 400 km along the orbital track, depending on the measurement mode (*18*), for a week.

Small-scale temperature fluctuations $T'(z)$ were isolated from global temperature data with a wavenumber 0 to 6 Kalman filter. Vertical wavelengths λ_z and amplitudes $\hat{T}$ of dominant oscillations in each $T'(z)$ profile were determined with spectral peak detection and sliding harmonic fits, respectively. These parameters are shown (Fig. 1B) for three successive $T'(z)$ profiles (labeled 1, 2, and 3) acquired over the southern Andes Mountains (Fig. 1C) on 6 November 1994. All three profiles show similar-looking large-amplitude wave oscillations at 15 to 30 km. The photo in Fig. 1A, taken over this region 2 days earlier, shows banded mountain wave clouds downstream of the Andes. This suggests that the oscillations in Fig. 1B may be stratospheric mountain waves.

A long, stationary plane mountain wave emanating from the Andes should have a vertical wavelength given by the hydrostatic relation

$$(\lambda_z)_{\text{theory}} \approx \frac{2\pi \bar{U}}{N} \qquad (1)$$

where $\bar{U}$ is the local horizontal wind speed across the Andean Ridge and N is the buoyancy frequency (*1*). At 15 to 30 km, $\bar{U} \approx 20$ to 23 m s^{-1} (Fig. 1D) and $N \approx 0.020$ rad s^{-1}, which yields $(\lambda_z)_{\text{theory}} \approx 6$ to 7 km. The observed vertical wavelength λ_z of the measured wave oscillations in Fig. 1B is ~6.5 km at 15 to 30 km. The close agreement between observed and theoretical vertical wavelengths is strong evidence that these measured wave oscillations are stratospheric mountain waves. Successive profiles are separated horizontally by 200 km (Fig. 1C) and phase shifted by 180° (Fig. 1B). This implies a horizontal wavelength $\lambda_h = 400/n$ km for this wave, where n is an odd integer. Given the sensitivity of CRISTA to $\lambda_h > 100$ to 200 km, then λ_h must be either 130 or 400 km.

Nonbreaking mountain waves grow in amplitude with height approximately as $\exp(z/2H_\rho)$. The density scale height $H_\rho \sim 7$ km, and so $\hat{T}$ should increase by a factor of 3 over the 15- to 30-km height range, as observed in Fig. 1B. Thus, the mountain wave propagates without breaking from 15 to 30 km. Above 30 km, the oscillations in Fig. 1B abruptly attenuate and disappear. There are two plausible reasons for this. Because winds weaken rapidly above this level (Fig. 1D), λ_z decreases according to Eq. 1, and the wave soon becomes too short for CRISTA to resolve. Additionally, however, the wave is likely to break above 30 km. Mountain waves advect heavy air over lighter air and overturn when amplitudes exceed the breaking threshold

$$\hat{T} \geq \hat{T}_{\text{break}} \approx \left[\frac{d\bar{T}}{dz} + \Gamma_a\right] \frac{\bar{U}}{N} \qquad (2)$$

where Γ_a is the adiabatic lapse rate (9.8 K km^{-1}) and $\bar{T}$ is background temperature (*19*). At 15 to 30 km, the mountain wave-breaking amplitude $\hat{T}_{\text{break}} \approx 10$ K. This value is consistent with the observed nondissipative growth in $\hat{T}$ from 15 to 30 km, because $\hat{T} < \hat{T}_{\text{break}}$ at these heights. At 30 km, however, $\hat{T} = 7$ K (Fig. 1B) and is probably larger in reality, given some observational smearing. Indeed, retrieval calculations indicate that, for a wave of $\lambda_z = 6.5$ km and $\lambda_h = 400$ km, the amplitude $\hat{T}$ measured by CRISTA is only ~60% of its true value (*17*). Thus, this wave is at or near its breaking amplitude at 30 km. Above 30 km, Eq. 2 shows that $\hat{T}_{\text{break}}$ decreases because of the weakening winds in Fig. 1D, making wave breaking and amplitude attenuation even more probable and severe.

The influence of a breaking mountain wave on the atmosphere is determined by its vertical flux of horizontal momentum density, the so-

[1]E. O. Hulburt Center for Space Research, Naval Research Laboratory, Code 7641.2, Washington, DC 20375, USA. [2]Department of Physics, University of Wuppertal, Gauss-Strasse 20, D-42097 Wuppertal, Germany.

*To whom correspondence should be addressed. E-mail: eckerman@map.nrl.navy.mil

called Eliassen-Palm (EP) flux, which can be computed from measured wave parameters (*20*). With the use of Eq. 2 and linear saturation theory (*2*, *19*), wave breaking above 30 km yields large EP flux divergences that imply mean-flow accelerations of up to −(50 to 200) m s^{-1} day^{-1}. These decelerative forces on the eastward stratospheric flow in Fig. 1D are one to two orders of magnitude larger than zonal-mean climatological estimates of small-scale wave forcing at 40° to 50°S (*21*). Such large values imply vigorous local wave breaking, drag, turbulence production, and mixing at 30 to 40 km. The wave is likely to dissipate entirely below 43 km, where a critical level ($\bar{U}$ = 0: Fig. 1D) causes both λ_z and $\hat{T}$ to vanish (Eqs. 1 and 2) and prevents further penetration of mountain wave energy (*1*).

How common are large mountain wave events? Figure 2 compares λ_z and $(\lambda_z)_{theory}$ at z = 25 km based on $T'(z)$ data for all seven mission days at 40° to 50°S over South America. Again, there is very good correlation between theoretical and measured vertical wavelengths. Amplitudes measured on four successive days are plotted in Fig. 3, A to D. Underlying plots show corresponding predictions, with the Naval Research Laboratory Mountain Wave Forecast Model (MWFM) (*4*, *22*) interfaced to assimilated regional winds and temperatures from NASA's Data Assimilation Office (DAO) (Fig. 3, E to G) (*23*). The MWFM results capture much of the day-to-day variability. Figures 2 and 3 reveal that mountain waves were present in this region of the stratosphere throughout the mission.

These long plane stratospheric mountain waves resemble those observed by aircraft over the Scandinavian Ridge (*8*, *24*). Rapid cooling of air by the latter waves produces PSCs, which in turn destroy Arctic ozone (*8*). Although the Andean mountain waves observed here also produce large temperature decreases (Fig. 3), they are probably too far north to yield temperatures cold enough to form PSCs. Nevertheless, as the edge of the Antarctic vortex moves back and forth across the tip of South America (*25*), strong turbulence generated by these mountain waves will mix tongues of ozone-depleted vortex air with ozone-rich air from mid-latitudes, thus diluting local ozone concentrations overall. The large EP flux divergences could also modify the subsequent evolution of the vortex (*26*).

Are stratospheric mountain waves evident elsewhere in the CRISTA data? $\hat{T}$ amplitudes over the Northern Hemisphere at 25, 35, and 45 km on 9 November 1994 are plotted in Fig. 4, A to C. Mountain wave amplitudes $\hat{T}$ predicted by MWFM on this day are shown in Fig. 4, D and F. Although the peak amplitudes differ (*27*), observations and model results show very similar geographical distributions. Most notable is a broad region of enhanced amplitudes over central Eurasia. The activity is produced by mountain waves from the Altai Mountains,

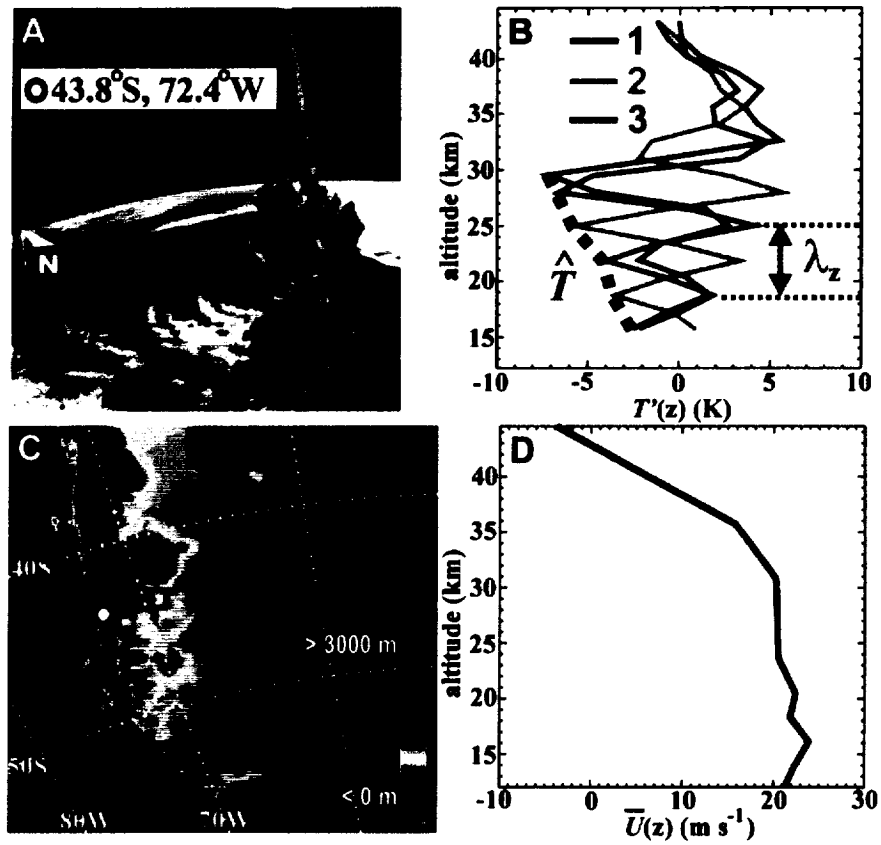

Fig. 1. (**A**) Astronaut photograph over southern South America showing deployment of CRISTA-SPAS from Atlantis, 4 November 1994, at 12:19 UT. The cylindrical assembly on the satellite houses CRISTA. The east coast of Argentina and the Atlantic Ocean are visible to the right; banded mountain wave clouds downstream of the Andes are visible to the lower left. (**B**) Temperature perturbations $T'(z)$ from three successive CRISTA scans (labeled 1, 2, and 3) on 6 November 1994, at ~06:00 UT. (**C**) Topographic elevations for southern South America (linear color scale). Squares labeled 1, 2, and 3 show locations of the profiles in (**B**). The nadir point and orbital motion of the shuttle in (**A**) are shown with a black and white circle and black arrow, respectively. (**D**) Horizontal winds orthogonal to the Andean Ridge, from DAO assimilated data (*23*) at 42°S, 69°W on 6 November 1994, 06:00 UT.

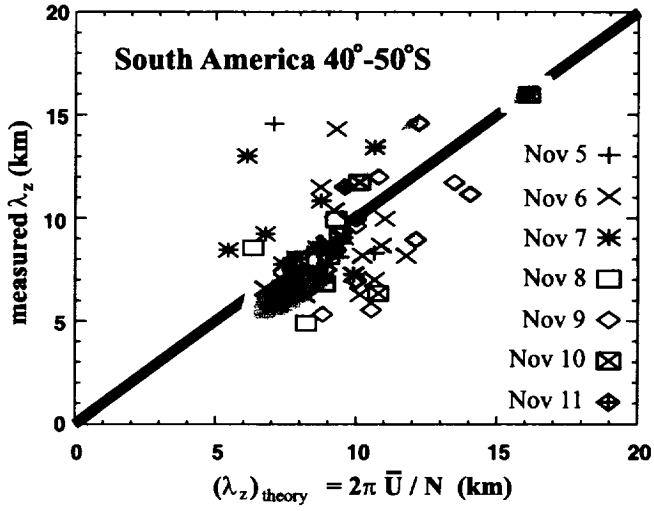

Fig. 2. Predicted mountain wave vertical wavelengths $(\lambda_z)_{theory}$ versus measured wavelengths λ_z for all profiles over South America between 40° and 50°S in the 20- to 30-km height range. In the calculations of $(\lambda_z)_{theory}$, $\bar{U}$ was approximated by the average total wind speed, because stratospheric flow was generally orthogonal to the Andean Ridge over the mission period. Wind speeds were taken from United Kingdom Meteorological Office assimilated data (*23*) for the days and times in question, with gridded values interpolated to the specific profile location and averaged from 20 to 30 km. Regions of largest amplitude-weighted point density are shaded.

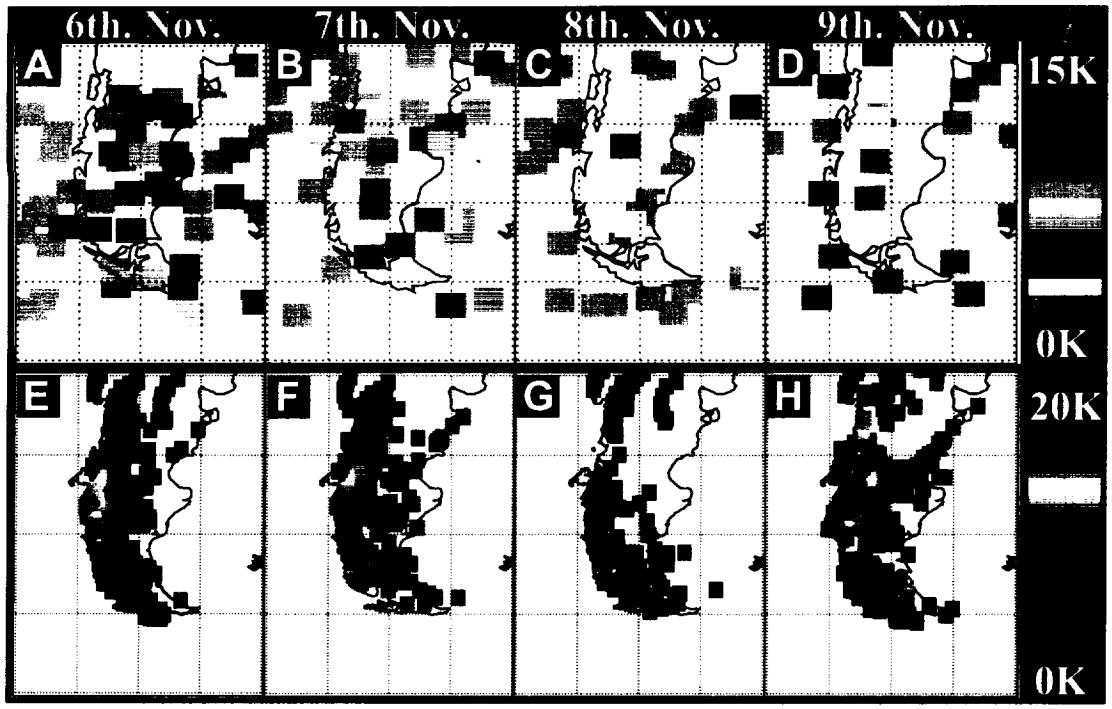

Fig. 3. $\hat{T}$ amplitudes over southern South America from 6 to 9 November 1994 (**A** to **D**, respectively), plotted as color pixels at the profile location. Raw values were scaled according to their vertical wavelengths to correct for observational smearing (*17*). Beneath each panel is a corresponding MWFM prediction based on DAO assimilated winds and temperatures at 12:00 UT for these dates (**E** to **H**). Modeled waves with $\lambda_z < 5$ km were not plotted because CRISTA is not sensitive to them. The color scales are linear. Pixels are plotted in order of ascending amplitude and are sized to maximize coverage and visibility while minimizing pixel overlap.

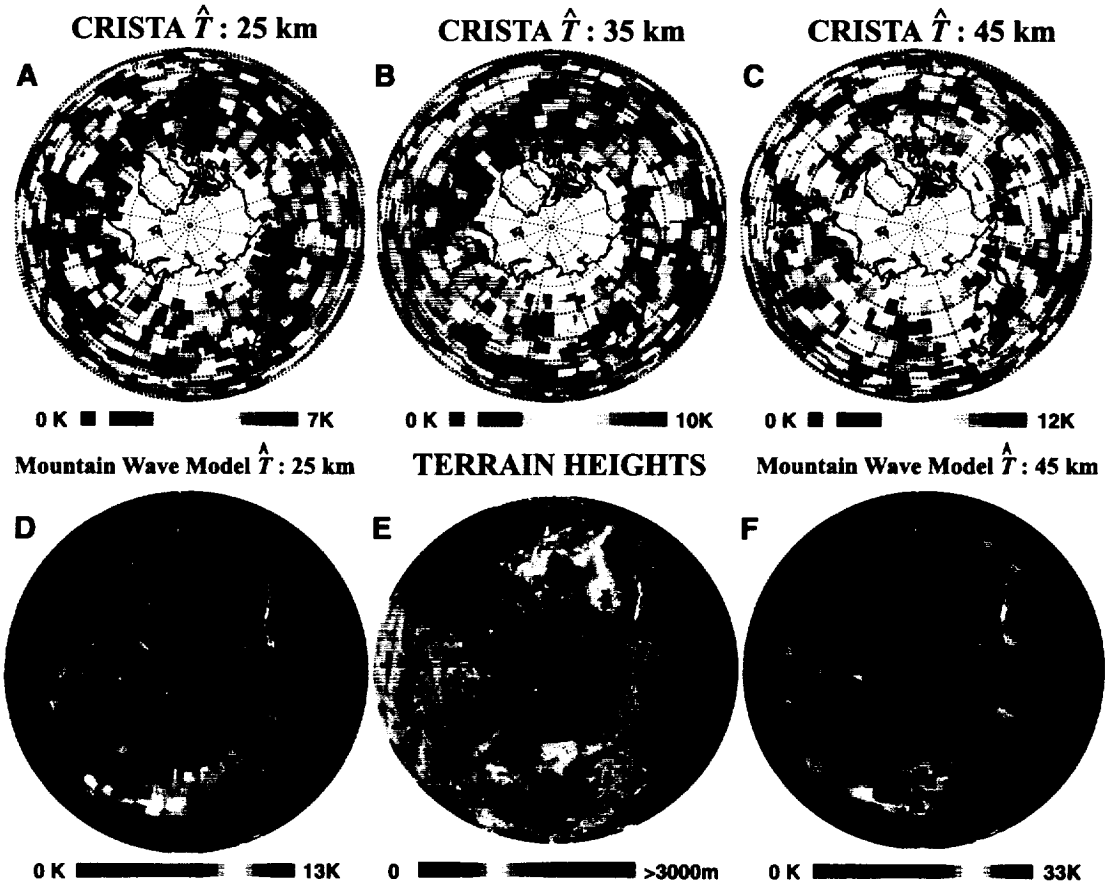

Fig. 4. (**A** to **C**) Polar orthographic maps of amplitudes $\hat{T}$ from CRISTA profiles over the Northern Hemisphere on 9 November 1994 at 25, 35, and 45 km, respectively. Values were corrected for observational smearing as in Fig. 3. (**D** and **F**) Corresponding MWFM amplitudes $\hat{T}$ at 25 and 45 km, respectively, based on DAO assimilated winds and temperatures at 12:00 UT on this date. As in Fig. 3, modeled waves with $\lambda_z < 5$ km were omitted. (**E**) Topographic elevation in the Northern Hemisphere. All color scales are linear. Pixels are plotted in order of ascending amplitude.

Sayan Ranges, and Tian Shan, which skirt the border regions of Russia, Mongolia, China, and Kazakhstan (Fig. 4E). These mountain waves are present at all heights, reaching the uppermost levels of the stratosphere (Fig. 4C). There is also evidence of more isolated mountain wave activity over the Alps and the Alaska-Yukon region. Mountain waves are largely absent in both the observations and model results over other mountainous regions, such as western North America, the Himalayas, Greenland, and Scandinavia. This absence occurs in the MWFM results because regional winds inhibit mountain wave propagation into the stratosphere.

Despite the basic similarities, specific differences between the CRISTA data and MWFM results are also evident in Figs. 3 and 4. Shortcomings in the model may be implicated here, highlighting the potential value of observations such as these in improving global mountain wave parameterizations.

Figure 4C also shows large $\hat{T}$ amplitudes at $z = 45$ km at the northernmost latitudes, which cannot be explained in terms of polar mountain waves (Fig. 4F). This observation is consistent with large gravity-wave amplitudes observed previously in ground-based soundings of the high-latitude winter upper stratosphere (*28*). The feature has been attributed to enhanced $\exp(z/2H_\rho)$ amplitude growth of weaker "background" gravity-wave activity, due to the temperature structure of the winter polar stratosphere (*13*, *29*), although longitudinal asymmetries in stratospheric winds can modulate the effect substantially (*30*). This indicates that CRISTA measured gravity waves from sources other than mountains as well.

References and Notes

1. R. B. Smith, *Adv. Geophys.* **21**, 87 (1979); M. G. Wurtele, R. D. Sharman, A. Datta, *Annu. Rev. Fluid Mech.* **28**, 429 (1996).
2. T. N. Palmer, G. J. Shutts, R. Swinbank, *Q. J. R. Meteorol. Soc.* **112**, 1001 (1986); N. McFarlane, *J. Atmos. Sci.* **44**, 175 (1987); J. Zhou, Y. C. Sud, K.-M. Lau, *Q. J. R. Meteorol. Soc.* **122**, 903 (1996).
3. D. K. Lilly and P. F. Lester, *J. Atmos. Sci.* **31**, 800 (1974).
4. J. T. Bacmeister, P. A. Newman, B. L. Gary, K. R. Chan, *Weather Forecasting* **9**, 241 (1994).
5. F. M. Ralph, P. J. Nieman, D. Levinson, *Geophys. Res. Lett.* **24**, 663 (1997); R. M. Worthington, *J. Atmos. Sol.-Terr. Phys.* **60**, 1543 (1998).
6. J.-F. Lamarque, A. O. Langford, M. H. Proffitt, *J. Geophys. Res.* **101**, 22969 (1996); T. Schilling, F.-J. Lübken, F. G. Wienhold, P. Hoor, H. Fischer, *Geophys. Res. Lett.* **26**, 303 (1999).
7. D. Cariolle, S. Muller, F. Cayla, M. P. McCormick, *J. Geophys. Res.* **94**, 11233 (1989); T. Deshler, T. Peter, R. Müller, P. Crutzen, *Geophys. Res. Lett.* **21**, 1327 (1994); K. S. Carslaw *et al.*, *J. Geophys. Res.* **103**, 5785 (1998); K. S. Carslaw, T. Peter, J. T. Bacmeister, S. D. Eckermann, *J. Geophys. Res.* **104**, 1827 (1999); J. Schreiner *et al.*, *Science* **283**, 968 (1999).
8. K. S. Carslaw *et al.*, *Nature* **391**, 675 (1998).
9. K. Sato, *J. Atmos. Sci.* **47**, 2803 (1990); F. M. Ralph, M. Crochet, S. V. Venkateswaran, *Q. J. R. Meteorol. Soc.* **118**, 597 (1992); R. M. Worthington and L. Thomas, *Geophys. Res. Lett.* **24**, 1071 (1997); C. M. Scavuzzo, M. A. Lamfri, H. Teitelbaum, F. Lott, *J. Geophys. Res.* **103**, 1747 (1998); J. A. Whiteway, *J. Atmos. Sci.* **56**, 1344 (1999).
10. G. J. Shutts and A. Broad, *Q. J. R. Meteorol. Soc.* **119**, 377 (1993); J. L. Attié, A. Druilhet, P. Durand, B. Bénech, *Ann Geophys.* **15**, 823 (1997); J. Dean-Day *et al.*, *Geophys. Res. Lett.* **25**, 1351 (1998).
11. J. T. Bacmeister, M. R. Schoeberl, L. R. Lait, P. A. Newman, B. Gary, *Geophys. Res. Lett.* **17**, 81 (1990); G. D. Nastrom and D. C. Fritts, *J. Atmos. Sci.* **49**, 101 (1992).
12. E. J. Fetzer and J. C. Gille, *J. Atmos. Sci.* **51**, 2461 (1994); D. L. Wu and J. W. Waters, *Geophys. Res. Lett.* **23**, 3631 (1996); R. H. Picard *et al.*, *Geophys. Res. Lett.* **25**, 2809 (1998).
13. M. J. Alexander, *J. Geophys. Res.* **103**, 8627 (1998).
14. D. Offermann *et al.*, *J. Geophys. Res.* **104**, 16311 (1999). CRISTA-SPAS orbited ~100 km behind the shuttle, with the CRISTA telescopes pointed opposite to the orbital motion (backward viewing). The left and right telescopes scanned the limb 18° on either side of the center telescope. This corresponds to tangent heights separated by ~600 km.
15. M. Riese *et al.*, *J. Geophys. Res.* **104**, 16349 (1999).
16. Riese *et al.* (*15*) give full details of version 1 CRISTA retrievals, which yielded temperatures of ~1 K precision. Data analyzed here come from improved version 2 retrievals (precision of ~0.5 K).
17. P. Preusse, B. Schaeler, J. T. Bacmeister, D. Offermann, *Adv. Space Res.*, in press. Visibility is defined here as the measured wave temperature amplitude divided by its actual amplitude.
18. There were two main measurement modes: a stratosphere mode (77 hours of data every 200 km along track) and a stratosphere-mesosphere mode (55 hours of data every 400 km along track). Additionally, every fourth profile was a high-altitude scan (HAS) (*15*). HAS data were not analyzed here.
19. See, for example, section 2.1 of D. C. Fritts, *Rev. Geophys.* **22**, 275 (1984).
20. EP flux F is conserved for a nonbreaking, steady plane mountain wave [A. Eliassen and E. Palm, *Geofys. Publ.* **22**, 1 (1961)]. With the use of irrotational hydrostatic gravity-wave relations, it can be evaluated from measured mountain wave variables as

$$F = \frac{-\rho g \lambda_z \hat{T}^2}{2\bar{T}\lambda_h[d\bar{T}/dz + \Gamma_a]}$$

where ρ is atmospheric density and g is gravitational acceleration. This equation yields a predominantly westward EP flux ~0.02 to 0.2 Pa below 30 km (given the quoted uncertainties in λ_h and $\hat{T}$). When mountain waves break, the vertical EP flux gradient quantifies the force exerted on the atmosphere and the intensity of turbulence generated locally (*2*, *4*, *19*, *22*).
21. M. J. Alexander and K. Rosenlof, *J. Geophys. Res.* **101**, 23465 (1996).
22. An improved research version of MWFM was used here, which uses ray-tracing methods to better simulate the amplitudes and three-dimensional nonhydrostatic propagation of waves through the atmosphere [S. D. Eckermann and C. J. Marks, *Adv. Space Res.* **20** (no. 6), 1253 (1997)].
23. L. Coy and R. Swinbank, *J. Geophys. Res.* **102**, 25763 (1997).
24. M. Leutbecher and H. Volkert, *Geophys. Res. Lett.* **23**, 3329 (1996); A. Dörnbrack, M. Leutbecher, H. Volkert, M. Wirth, *Meteorol. Appl.* **5**, 117 (1998).
25. CRISTA ozone and trace gas data show this clearly; see Plate 2a of M. Riese *et al.* [*J. Geophys. Res.* **104**, 16349 (1999)] and Plate 5 of M. Riese, X. Tie, G. Brasseur, and D. Offermann [*J. Geophys. Res.* **104**, 16419 (1999)].
26. R. R. Garcia and B. A. Boville, *J. Atmos. Sci.* **51**, 2238 (1994); T. J. Duck, J. A. Whiteway, A. I. Carswell, *Geophys. Res. Lett.* **25**, 2813 (1998).
27. There are a number of reasons for these differences. Although efforts were made to correct for observational smearing of the CRISTA $\hat{T}$ values, measured amplitudes may still be substantially underestimated. Additionally, linear plane-wave parameterizations such as MWFM tend to overestimate wave amplitudes [S. A. Smith, D. C. Fritts, T. E. VanZandt, *J. Atmos. Sci.* **44**, 1404 (1987); G. J. Shutts, *Q. J. R. Meteorol. Soc.* **124**, 1421 (1998)].
28. I. Hirota, *J. Atmos. Terr. Phys.* **46**, 767 (1984); S. D. Eckermann, I. Hirota, W. K. Hocking, *Q. J. R. Meteorol. Soc.* **121**, 149 (1995).
29. S. D. Eckermann, *J. Atmos. Terr. Phys.* **57**, 105 (1995).
30. J. A. Whiteway *et al.*, *Geophys. Res. Lett.* **24**, 1387 (1997).

31. This research was supported by the Office of Naval Research and by NASA through the Atmospheric Chemistry Modeling and Analysis Program and the Upper Atmosphere Research Satellite Guest Investigator Program.

17 June 1999; accepted 19 October 1999

Enhancement of Interdecadal Climate Variability in the Sahel by Vegetation Interaction

Ning Zeng,[1]* J. David Neelin,[1] K.-M. Lau,[2] Compton J. Tucker[2]

The role of naturally varying vegetation in influencing the climate variability in the West African Sahel is explored in a coupled atmosphere–land-vegetation model. The Sahel rainfall variability is influenced by sea-surface temperature variations in the oceans. Land-surface feedback is found to increase this variability both on interannual and interdecadal time scales. Interactive vegetation enhances the interdecadal variation substantially but can reduce year-to-year variability because of a phase lag introduced by the relatively slow vegetation adjustment time. Variations in vegetation accompany the changes in rainfall, in particular the multidecadal drying trend from the 1950s to the 1980s.

The rainfall over the West African Sahel region (*1*) shows a multidecadal drying trend from the 1950s to the 1980s and early 1990s, as well as strong interannual variability (Fig. 1A). Causes proposed to explain this dramatic trend include global sea surface temperature (SST) variations (*2*–*5*) and land use change, that is, the desertification process (*6*, *7*). Because vegetation distribution tends to be controlled largely by climate (*8*, *9*), and surface property changes can affect climate by modifying the atmospheric energy and water budget (*10*–*13*), it is reasonable to propose that dynamic vegetation-climate interaction might influence decadal climate variability substantially in a climatically sensitive zone such as the Sahel. We tested this

GEOPHYSICAL RESEARCH LETTERS, VOL. 27, NO. 23, PAGES 3877-3880, DECEMBER 1, 2000

Comparison of Global Distributions of Zonal-Mean Gravity Wave Variance Inferred from Different Satellite Instruments

Peter Preusse,[1] Stephen D. Eckermann[2] and Dirk Offermann[1]

Abstract.
Gravity wave temperature fluctuations acquired by the CRISTA instrument are compared to previous estimates of zonal-mean gravity wave temperature variance inferred from the LIMS, MLS and GPS/MET satellite instruments during northern winter. Careful attention is paid to the range of vertical wavelengths resolved by each instrument. Good agreement between CRISTA data and previously published results from LIMS, MLS and GPS/MET are found. Key latitudinal features in these variances are consistent with previous findings from ground-based measurements and some simple models. We conclude that all four satellite instruments provide reliable global data on zonal-mean gravity wave temperature fluctuations throughout the middle atmosphere.

Introduction

Remote-sensing instruments on satellites have revolutionized our understanding of the synoptic-scale dynamics and chemistry of the middle atmosphere. Since the structure of the middle atmosphere is controlled in large part by gravity wave breaking, global measurements of gravity wave activity are needed to further our understanding of this region of the atmosphere [*McLandress*, 1998]. This requires satellite measurements of high precision and high spatial resolution in all three dimensions, which most previous instruments have not provided. Thus, comparatively little global information on gravity wave activity exists.

Recent advances in remote-sensing technology have produced instruments capable of measuring gravity waves. To date, gravity wave signals have been analyzed on global scales using temperature data acquired by the Limb Infrared Monitor of the Stratosphere (LIMS) [*Fetzer and Gille*, 1994], 63 GHz limb radiances measured by the Microwave Limb Sounder (MLS) [*Wu and Waters*, 1996; *Wu and Waters*, 1997; *McLandress et al.*, 2000], temperature data from the Cryogenic Infrared Spectrometers and Telescopes for the Atmosphere (CRISTA) [*Preusse et al.*, 1999; *Eckermann and Preusse*, 1999], and temperature retrievals from the Global Positioning System Meteorological Experiment (GPS/MET) [*Tsuda et al.*, 2000].

Puzzling differences among these data sets have emerged. An example is given in the top row of Figure 1, which shows zonal mean gravity wave variances from LIMS and MLS in the northern winter. The MLS radiance variances (Figure 1*b*) should be closely related to temperature variance [*Wu and Waters*, 1997], and so should resemble the LIMS temperature variances in Figure 1*a*. However, substantial differences between the two are evident. Since gravity waves are near the detection limits of each instrument, these discrepancies might call some or all of these data into question.

Using a theoretical model, *Alexander* [1998] argued instead that the MLS variances in Figure 1*b* are reliable, but

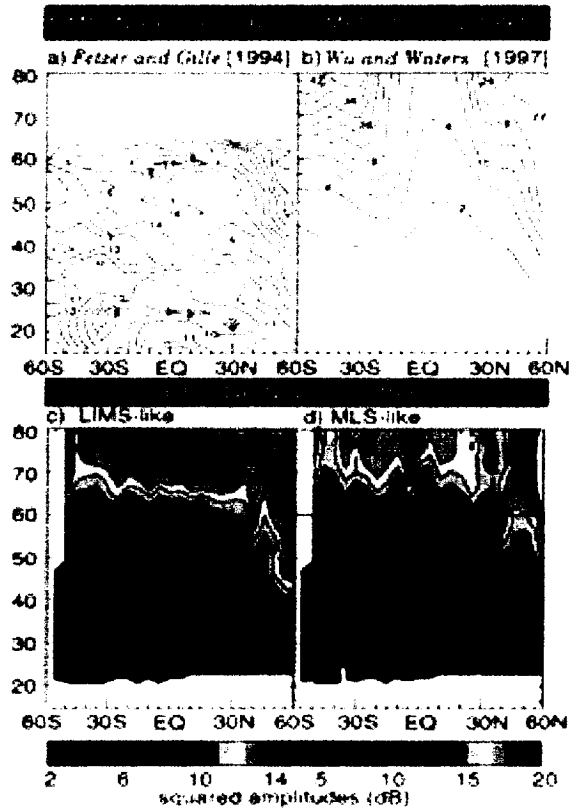

Figure 1. Top row: zonal-mean latitude-height distributions of small-scale variances in data from LIMS (a) and MLS (b), after *Fetzer and Gille* [1994] and *Wu and Waters* [1997], respectively. LIMS contours are temperature variances in dB over 1 K^2 (10 dB = 10 K^2, 20 dB = 100 K^2). MLS contours are relative radiance variances, with contour labels in multiples of 10^{-7}. Bottom row: corresponding squared temperature amplitudes from corrected CRISTA MEM/HA data. See text for details of the filters used in each case for comparison with LIMS (c) and MLS (d).

[1] Department of Physics, Wuppertal University, Germany
[2] E. O. Hulburt Center for Space Research, Naval Research Laboratory, Washington, DC

Paper number 2000GL011916.
0094-8276/00/2000GL011916$05.00

that the vertical weighting functions of this instrument play a pivotal role in controlling the global distributions. She went on to argue that meaningful comparisons of gravity wave data from different satellites requires careful consideration of the spatial sensitivities of each instrument. These ideas were used by *McLandress et al.* [2000] to argue that longitudinal variations in MLS variances at ~38 km can provide information on sources. These ideas have not been tested on other satellite data sets.

Here, we test Alexander's hypothesis by applying it in an intercomparison of zonal-mean gravity wave variances from the aforementioned satellite instruments. In section 2, we present updated calculations of the spatial sensitivity of the CRISTA temperature data to gravity waves, and use them to apply approximate corrections to these data. In section 3, we apply additional filters to the corrected CRISTA gravity-wave data that mimic the LIMS, MLS and GPS/MET vertical weighting functions, and compare the resulting zonal mean variances with actual data from LIMS, MLS and GPS/MET.

Gravity Wave Data from CRISTA Temperatures

In this study, we use gravity wave data derived from temperatures measured by CRISTA during the first CRISTA-SPAS mission in November, 1994 [*Offermann et al.*, 1999]. We use a two-day subset of these data which scanned the largest range of altitudes [*Riese et al.*, 1999]. To isolate short scales, the large-scale global background was removed using a 0-6 zonal wavenumber Kalman filter (see also *Fetzer and Gille* [1994]). Separate daytime and nighttime fits were used to remove tidal structures as well. The resulting temperature residuals contain gravity wave fluctuations [*Preusse et al.*, 1999; *Eckermann and Preusse*, 1999].

To characterize these waves, individual vertical profiles were analyzed using the Maximum Entropy Method (MEM) and harmonic analysis (HA). The MEM spectrum was calculated using the complete height profile. The MEM peaks were used to constrain harmonic fits to the profile within a 13 km altitude window that was moved upwards in 1.5 km increments to span the full height range. This MEM/HA analysis provides height profiles of the amplitudes, phases and vertical wavelengths of the two largest oscillations in any given profile, and allows these values to vary with height (see also Eckermann and Preusse [1999]).

Sensitivity of CRISTA temperatures to gravity waves can be estimated from high spatial resolution radiative transport calculations using two-dimensional sinusoidal temperature perturbations of varying vertical wavelength λ_z and horizontal wavelength λ_h [*Preusse et al.*, 1999]. Updated calculations, using the BANDPAK libraries [*Marshall et al.*, 1994] and postprocessing through CRISTA retrieval algorithms, are summarized in Figure 2. The contours show the fraction of the gravity wave temperature amplitude recovered by CRISTA, $\epsilon(\lambda_h, \lambda_z)$, hereafter called the "visibility." We note $\gtrsim$50% visibility for waves of $\lambda_z \gtrsim 5$ km and $\lambda_h \gtrsim 200$ km. These are worst case scenarios in which

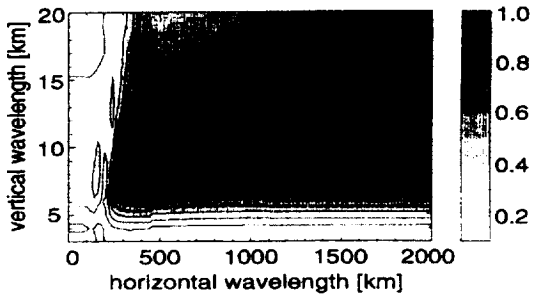

Figure 2. Sensitivity, or "visibility" $\epsilon(\lambda_h, \lambda_z)$, of CRISTA temperature data to gravity wave temperature oscillations of different horizontal and vertical wavelengths (λ_h and λ_z). The 0.5 contour is highlighted (thick dashed line). Here, the waves propagate horizontally parallel to the CRISTA line of sight. Values were derived from high spatial resolution radiance calculations (see text).

CRISTA scans across the wave phase fronts. Waves with horizontal wavevectors rotated by ±90° present phase fronts that CRISTA scans along. For these waves, the shortest visible λ_h is much shorter [*Fetzer and Gille*, 1994; *Wu and Waters*, 1997].

For $\lambda_h \lesssim 1000$ km, typical of most gravity waves in the middle atmosphere [*Reid and Vincent*, 1987], Figure 2 shows that $\epsilon(\lambda_h, \lambda_z)$ reaches a maximum at $\lambda_z \sim 10$ km and depends weakly on λ_h for $\lambda_h \gtrsim$ 200–300 km. Hence we derive a one-dimensional visibility $\hat{\epsilon}(\lambda_z)$, averaged over the λ_h = 300–800 km range for each λ_z. We use $\hat{\epsilon}^{-1}(\lambda_z)$ to scale measured CRISTA amplitudes and compensate to some extent for observational degradation. These corrected CRISTA data contain gravity waves roughly in the range λ_z = 3–25 km.

Effective Visibilities of LIMS, MLS, and GPS/MET

Next we choose simple boxcar visibility functions $\hat{\epsilon}(\lambda_z)$ for the LIMS, MLS and GPS/MET instruments, following *Alexander* [1998]. However, rather than applying them to model data, here we apply them to the corrected CRISTA MEM/HA data to derive gravity wave temperature data that are "LIMS-like," "MLS-like," and "GPS/MET-like."

In isolating temperature fluctuations from LIMS, *Fetzer and Gille* [1994] applied only a wavenumber 0-6 Kalman filter at each level. This involves no vertical filtering, so only observational degradation affects the range of resolved vertical wavelengths. Calculations by *Bailey and Gille* [1986] suggested that LIMS should measure gravity waves of $\lambda_z \gtrsim 6$ km with roughly equal sensitivity: however, these calculations were based on vertical weighting functions that did not take into account the two-dimensional spatial structure of the waves [*Preusse et al.*, 1999]. Because LIMS and CRISTA had nearly the same viewing geometry, we assume here that their visibility characteristics were broadly similar. To test this, we computed latitude-height temperature variances from CRISTA using the same method as *Fetzer and*

Gille [1994], and compared them to latitude-height distributions of filtered forms of the corrected CRISTA MEM/HA data. Best agreement was found using a pass band of λ_z =3-15 km on the corrected CRISTA MEM/HA data. This result is consistent with diminished LIMS visibility to long vertical wavelengths, as was inferred for CRISTA in Figure 2.

MLS radiance fluctuations were analyzed by *Wu and Waters* [1997]. They argued that MLS could not resolve waves of $\lambda_z \lesssim 10$ km and had greatest sensitivity to waves of $\lambda_z \gg 10$ km. The MLS weighting functions at high altitudes were even broader, and could not resolve $\lambda_z \lesssim 15$ km. Thus, we approximate MLS visibilities using boxcar passbands of λ_z =10–25 km below 60 km and λ_z =15–35 km above 60 km. The sliding HA window was increased to 17 km to yield more reliable long-wavelength data for the latter pass band. While these filters capture the first-order effects, actual MLS visibility functions are more complex [*Wu and Waters*, 1997; *McLandress et al.*, 2000].

In isolating gravity waves from GPS/MET temperature profiles, *Tsuda et al.* [2000] used a high pass filter which eliminated $\lambda_z > 10$ km. Thus, we generate GPS/MET-like data from the corrected CRISTA MEM/HA data using a λ_z =3–10 km pass band.

The total error estimates are 0.7 dB for the LIMS-like CRISTA data, 1.5 dB for the MLS-like data, and ~30% for the GPS/MET-like data.

Intercomparison of Zonal Mean Variances

Zonal-mean gravity wave variances during winter are shown in Figure 1. The LIMS data in Figure 1a [after *Fetzer and Gille*, 1994] show small-scale temperature variance in dB over 1 K^2, averaged from 6-12 November, 1978. Notable features are the strong tropical maximum and midlatitude minima in the lower stratosphere ($z \sim$ 16–30 km) and enhanced activity throughout the stratosphere and lower mesosphere at high northern latitudes. Variances grow with height over the $z \sim$ 25–40 km range. Above 40-45 km, however, amplitudes remain relatively constant with height, apart from a weak tropical maximum at ~60 km.

Many of these features can be seen in the LIMS-like CRISTA MEM/HA data in Figure 1c. At the lowest heights, the midlatitude minima and equatorial maximum are reproduced. Enhanced variance occurs at high northern latitudes. Variances grow with height up to ~40-45 km, but show little growth with height from 45-60 km. Interestingly, the LIMS-like CRISTA variance grows with height from ~60-75 km before growth abates again at the uppermost heights ~75-80 km (there are no LIMS data above 65 km for comparison).

One large difference exists, however. The absolute values in Figures 1a and 1c should agree, whereas we find a mean offset between the two of ~5 dB. The same offset occurs when we compute CRISTA temperature variances using the same procedure as *Fetzer and Gille* [1994]. Substantially stronger background winds during the LIMS period may have contributed by allowing more waves of longer wavelength into the middle atmosphere. In addition, differences between the two instruments may also be implicated.

Figure 1b shows normalized MLS radiance variances, averaged from 20 December, 1992 to 29 January, 1993 [after *Wu and Waters*, 1997]. The latitude-height distribution differs from the LIMS data at heights where the measurements overlap (~33-64 km). For example, a column of attenuated MLS variance at ~0–20°N extends throughout the middle atmosphere. MLS variances at high northern latitudes are largest at the lowest altitudes only: at upper altitudes, largest values occur in the midlatitude southern hemisphere. There is also no variance "plateau" above 40–45 km: MLS variances grow with height throughout the altitude range.

Since the MLS-like CRISTA data are temperature variances and the MLS data are radiance variances, Figures 1b and 1d can be compared qualitatively only. Nevertheless, the agreement in latitude-height morphology below 60 km is quite good. Both variances grow with altitude up to ~70 km. There is also a column of reduced variance at ~0–20°N and of enhanced variance at ~10–20°S and 60°N. At mesospheric heights, the agreement is less impressive. It appears that the waves resolved by each instrument have such different vertical and horizontal wavelengths at these altitudes that corrected CRISTA MEM/HA data still cannot adequately reproduce the MLS data.

GPS/MET variances from *Tsuda et al.* [2000] are plotted with diamonds in Figure 3, while the GPS/MET-like CRISTA MEM/HA variances are plotted with asterisks. These values have been converted into potential energies per unit mass, $E_{pot} = \frac{1}{2}(g/N)^2 \langle T'/\bar{T} \rangle^2$, where $< T'/\bar{T} >^2$ is

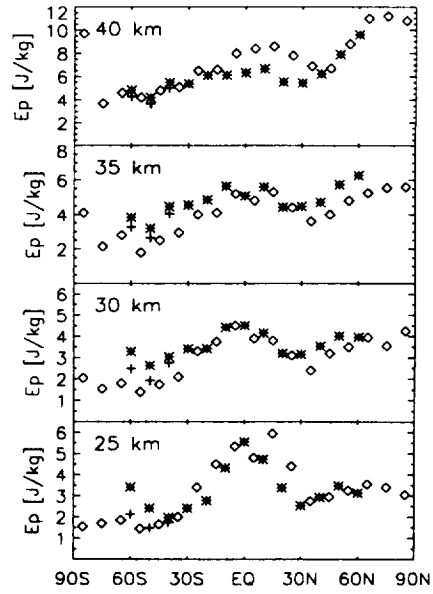

Figure 3. Zonal mean potential energy per unit mass, E_{pot}, as a function of latitude and height, derived from GPS/MET data (diamonds) [after *Tsuda et al.*, 2000] and the GPS/MET-like CRISTA MEM/HA data (stars). Crosses replot the CRISTA MEM/HA data at 50-60°S after removal of large values over South America due to mountain waves.

the relative temperature variance, T is local background temperature, g is gravitational acceleration and N is background Brunt-Väisälä frequency. Even though GPS/MET data were acquired and analyzed in a quite different way from CRISTA and are averages for three winter months and different years, the agreement between the two is excellent, both in absolute terms and in latitudinal variations.

Slight differences at low altitudes at 50-60°S can be explained by strong mountain wave activity excited over South America during November, 1994 [*Eckermann and Preusse*, 1999]: Omitting CRISTA data from this region yields variances (crosses in Figure 3) that agree much better with the GPS/MET data. These data also compare well with the LIMS data in Figure 1a: for example, we see clear evidence of a tropical maximum and midlatitude minima at lower heights in Figure 3.

Summary and Conclusions

Differences among zonal-mean gravity wave variances inferred from four different satellite instruments that measured middle atmosphere temperatures during northern winter are shown here to result in large part from the different "visibilities" to gravity waves. Once these observational effects were taken into account, using a method where we scaled CRISTA gravity wave data, good comparisons were found with results from the other three instruments. The resulting zonal-mean latitude-height variance distributions in Figures 1 and 3 also have much in common with ground-based measurements from this region [*Alexander*, 1998; *Tsuda et al.*, 2000]. For instance, the lack of growth in LIMS temperature variances from 45-60 km (Figure 1a) is also seen in rocketsonde data [*Eckermann et al.*, 1995; *Eckermann*, 1995].

Thus, our analysis shows that gravity wave signals in all four satellite instruments are reliable and yield reproducable zonal-mean structures. This work provides direct experimental support for similar arguments made by *Alexander* [1998] using model data. While it now appears that basic zonal-mean features noted here can be explained without invoking sources [*Eckermann*, 1995; *Alexander*, 1998], recent work has shown that longitudinal variability can often be source related [*Eckermann and Preusse*, 1999; *McLandress et al.*, 2000].

Acknowledgments.

We thank T. B. Marshall and L. L. Gordley for providing us with the BANDPAK radiance model. The CRISTA experiment is funded by the Bundesministerium fuer Bildung und Forschung (BMBF,Berlin) through Deutsches Zentrum fuer Luft- und Raumfahrt (DLR,Bonn). SDE's research was supported by NASA's UARS Guest Investigator Program (NAS5-98045)

References

Alexander, M. J., Interpretations of observed climatological patterns in stratospheric gravity wave variance, *J. Geophys. Res.*, *103*, 8627-8640, 1998.

Bailey, P. L. and J. C. Gille, Inversion of limb radiance measurements: an operational algorithm, *J. Geophys. Res.*, *91*, 2757-2774, 1986.

Eckermann, S. D., On the observed morphology of gravity-wave and equatorial-wave variance in the stratosphere, *J. Atmos. Terr. Phys.*, *57*, 105–134, 1995.

Eckermann, S. D. and P. Preusse, Global measurements of stratospheric mountain waves from space, *Science*, *286*, 1534-1537, 1999.

Eckermann, S. D., I. Hirota, W. K. Hocking, Gravity wave and equatorial wave morphology of the stratosphere derived from long-term rocket soundings, *Q. J. R. Meteorol. Soc.*, *121*, 149-186, 1995.

Fetzer, E. J., and J. C. Gille, Gravity wave variances in LIMS temperatures, I, Variability and comparison with background winds, *J. Atmos. Sci.*, *51*, 2461-2483, 1994.

Marshall, B. T., L. L. Gordley, and D. A. Chu, Bandpak: Algorithms for modeling broadband transmissions and radiance, *J. Quant. Spectrosc. Radiat. Transfer*, *52*, 563-599, 1994.

McLandress, C., On the importance of gravity waves in the middle atmosphere and their parameterization in general circulation models, *J. Atmos. Terr. Phys.*, *60*, 1357-1383, 1998.

McLandress, C., M. J. Alexander and D. L. Wu, Microwave Limb Sounder observations of gravity waves in the stratosphere: a climatology and interpretation, *J. Geophys. Res.*, *105*, 11,947-11967, 2000.

Offermann, D., et al., Cryogenic Infrared Spectrometers and Telescopes for the Atmosphere (CRISTA) experiment and middle atmosphere variability, *J. Geophys. Res.*, *104*, 16,311-16,325, 1999.

Preusse, P., et al., Evidence for gravity waves in CRISTA temperatures, *Adv. Space Res.*, *24*, (11)1601-(11)1604, 1999.

Reid, I. M., and R. A. Vincent, Measurements of the horizontal scales and phase velocities of short period mesospheric gravity waves, *J. Atmos. Terr. Phys.*, *49*, 1033–1048, 1987.

Riese, M., et al., Cryogenic Infrared Spectrometers and Telescopes for the Atmosphere (CRISTA) data processing and atmospheric temperature and trace gas retrieval, *J. Geophys. Res.*, *104*, 16,349-16,367, 1999.

Tsuda, T., et al., A global morphology of gravity wave activity in the stratosphere revealed by the GPS occultation data (GPS/MET), *J. Geophys. Res.*, *105*, 7257-7273, 2000.

Wu, D. L. and J. W. Waters, Satellite observations of atmospheric variances: A possible indication of gravity waves, *Geophys. Res. Lett.*, *23*, 3631-3634, 1996

Wu, D. L. and J. W. Waters, Observations of gravity waves with the UARS Microwave Lims Sounder, in *Gravity wave processes: their parameterization in global climate models*, NATO ASI Series, Vol. I 50, K. Hamilton ed., Springer-Verlag, Heidelberg, 103-120, 1997.

P. Preusse and D.Offermann, Department of Physics, Wuppertal University, Gauss Str. 20, D-42097 Wuppertal, Germany, (email preusse@wpos2.physik.uni-wuppertal.de)

S. D. Eckermann, E. O. Hulburt Center for Space Research, Code 7641.2, Naval Research Laboratory, Washington, DC 20375-5352, USA, (email eckerman@map.nrl.navy.mil)

(Received June 20, 2000; revised September 4, 2000; accepted September 8, 2000.)

Wed. Feb 7, 2001
News
Missions/Launches
Science/Astronomy
Astronomy
Solar System
Planet Earth
General Science
SpaceWatch
Virtual Space Tour
Constellation Quiz
SETI: Search for Life
Photos/Videos
SpaceTV
Business/Technology
Science Fiction
Entertainment
Games
SpaceKids
People
Message Boards
TeachSpace
Reference
Spaceshop

Satellite Spots Turbulence-Producing Mountain Waves in the Stratosphere

By Robert Roy Britt
Senior Science Writer
posted: 04:04 pm ET
18 November 1999

When masses of air flow over massive mountains, invisible waves often roil high into the stratosphere, affecting weather and mixing the chemicals that contribute to ozone depletion. The waves also create turbulence that can be a danger to high-altitude research missions by NASA's lightweight ER-2 aircraft, as well as shuttle flights upon reentry.

In Friday's issue of the journal *Science*, researchers report for the first time a technique that allows them to see temperature signatures from these invisible mountain waves. The method, involving high-resolution, satellite-based measurement of adjacent pockets of the atmosphere, is expected to aid in spotting turbulence and, one day, improve weather forecasts.

Hanging 10, in 3-D

Much like water waves in the ocean, airborne mountain waves rush, break and tumble. But in the air, which is virtually unconfined compared to a body of water, waves propagate in three dimensions, said Stephen Eckermann of the Naval Research Laboratory in Washington, DC.

"Imagine a rock protruding out of water," explained Eckermann, lead researcher on the study. "You'll get a wave or ripple pattern as water passes over and around the rock. Air over a mountain acts very much the same way."

But a typical wave approaching the beach is pretty much limited to two-dimensional movement. Even a ship's waves, which move outward in many directions, travel only along the surface -- at least for the most part. A submarine, on the other hand, sends out three-dimensional waves that are more closely resemble the airborne mountain waves.

Picture the ripples radiating outward from a stone thrown into a pond, Eckermann suggests, and then attempt to fathom distorting all this motion into a cone that also extends upward from the pond. Well, okay, so it's not so simple. And that, Eckermann says, is why it has taken until now to measure the high-altitude mountain waves.

"To model it three-dimensionally is a complicated problem," he said, adding that it's "an important problem" because of the effects on weather, turbulence and ozone depletion.

Seeing the wind from space

The key to modeling waves in the stratosphere -- which extends upward from about 7 miles to around 30 miles -- was to view them from above. Because the waves move quickly -- changing structure significantly over periods as short as 5 minutes -- a method of quick measurement was needed.

So in 1994, a shuttle temporarily deployed a satellite named CRISTA 1, which produced infrared images of the atmosphere. It measured minute temperature differences between relatively small, adjacent patches of air. Eckermann explained how this, ultimately, revealed the waves:

"The wave is basically moving air particles from side-to-side and up-and-down as the wave propagates through. As it moves air up, the air cools, and as it moves it down, it warms." The wave, moving through, leaves a signature of change, a "temperature wave." In a region of the atmosphere where temperatures range from -80 to -20 degrees Celsius, the satellite picked out temperature differences as little as 2 to 10 degrees.

Eckermann and his colleague, Peter Preusse of the University of Wuppertal in Germany, found that mountain waves come in a variety of forms, and not all of the waves make it to the stratosphere.

"You have very long, slow waves and very short, fast waves, depending on the topography of the mountain underneath," Eckermann said. While some of the faster waves can reach the stratosphere in an hour or less, others lumber up there over several days.

Knowing how the waves mix chemicals in the atmosphere could provide clues to ozone creation and depletion, Eckermann says. Regionally, the new model can help predict how the waves, typically 100 to 200 kilometers across, might affect weather.

Over the Andes in South America, for example, waves routinely reach the stratosphere, having a significant effect on weather along the way. But in western North America, the jet stream inhibits their travels aloft, and rarely do the waves make it to the outer reaches of our atmosphere. In the tropics, where there is less land and little topography, standard convection and thunderstorm activity have a far greater impact on weather.

Because mountain waves can change so quickly, and because computer models used to forecast weather always have a finite capacity for data, most models use estimates of the phenomena based on long-term characteristics. Feeding in better data, based on real-time measurements, ought to improve forecasting.

"This is why we think space-based measurement of mountain waves will be important," Eckermann said.

More to Explore

- **Top 10 Weirdest Things in Space: See the New List Based on Your Votes!**
- Photo Galleries
- Virtual Space Tour

- **SPACE.com home**
- **Back to top**
- **E-mail this story to a friend**
- **Share your comments, suggestions or criticisms on this or any SPACE.com experience.**

related links

The CRISTA satellite

images

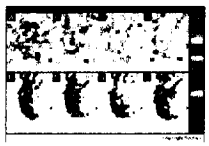

CUTLINE: Top row represents satellite-measured temperature signature of a mountain wave (red) over the Andes that dissipates by Nov. 8. Bottom row shows computer model of the wave based on the data and other factors.

The CRISTA-1 satellite used an infrared imager to study mountain waves in 1994. CREDIT: NASA

more stories

U.K. Computer Could Predict Impact of Solar Storms

Floyd's Marine Damage Monitored from Space

Ikonos Takes a Close Look at World Cities

Space Weather Forecast:
Coronal Holes Allow Solar Raygun to Zap Earth

about us | **sitemap** | **space links** | **contact us** | **advertise**